Spin-dependent Transport in Magnetic Heterostructures: Ohmic and Tunneling Regimes

Ikhtiar

Doctoral Program in Materials Science and Engineering

Submitted to the Graduate School of Pure and Applied Sciences in Partial Fulfillment of the Requirements for the Degree of Doctor of Philosophy in Engineering

at the University of Tsukuba

Contents

List of Figures

List of Tables

Chapter 1

Introduction

1.1 Overview : spintronics and magnetic data storage

The study on spin-dependent transport of magnetic heterostructures has rapidly progressed in the last two decades owing to various spintronics phenomena that can be observed in this artificial systems [1–3]. While electrons in ferromagnetic (FM) metals had been long proposed to flow independently in spin-up and spin-down channels [4, 5], the novel consequence of this phenomena could only be demonstrated in a magnetic hetero-structure composed of FM and and non-magnetic (NM) metals (see Fig. 1.1). It was the report on the giant magnetoresistance (GMR) effect in Fe/Cr/Fe multilayers that opened the new research avenue the so-called spintronics in which magnetic hetero-structures play a pivotal role [6, 7].

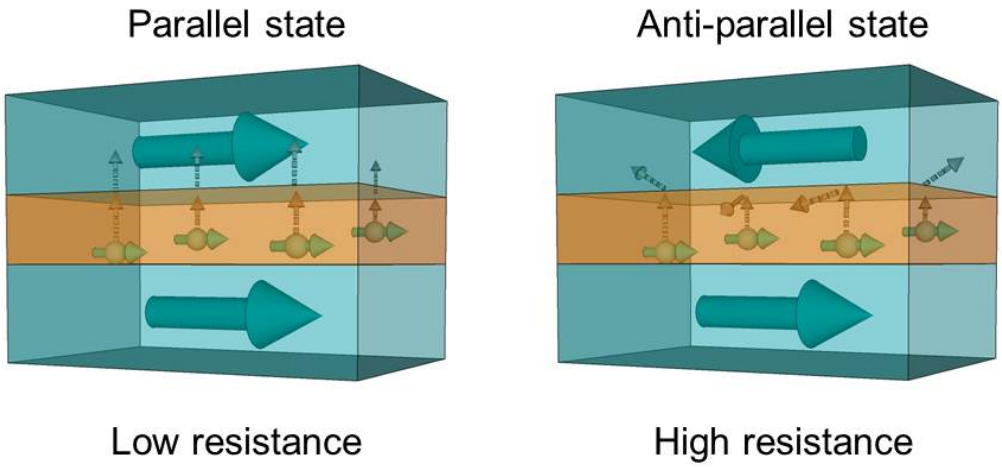

Figure 1.1: The giant magnetoresistance (GMR) effect in the FM/NM/FM trilayer structure. In the parallel state, the spin-polarized electrons coming from bottom FM can travel easily through top FM as the electron spin orientation is parallel to the local magnetization of top FM, hence resulting in low resistance (R_{P}). On the other hand, in the antiparallel state the spin polarized electrons coming from bottom FM will be strongly scattered once they enter the top FM since the electron spin orientation is antiparallel to the local magnetic moment of top FM, hence resulting in higher resistance (R_{AP}) compared to that in the parallel state. Note that, in this illustration current is assumed to flow perpendicular to the plane of the trilayer structure. The resistance change is typically expressed as MR ratio given as (R_{AP}-R_{P})/R_{P}.

The discovery of the GMR effect has profound impacts on both the basic understanding of spin-dependent electron transport and its applications. The giant resistance change that it can exhibit depending on the relative orientation of the FM layers magnetization made the GMR effect immediately envisaged as promising magnetic field sensors [8, 9]. The use of the GMR effect, in particular, for read sensor applications (Fig. 1.2) enabled the ever increasing areal density of hard disk drives (HDD) and was considered as the main contribution of spintronics research in driving the revolution in data storage technology [1, 3].

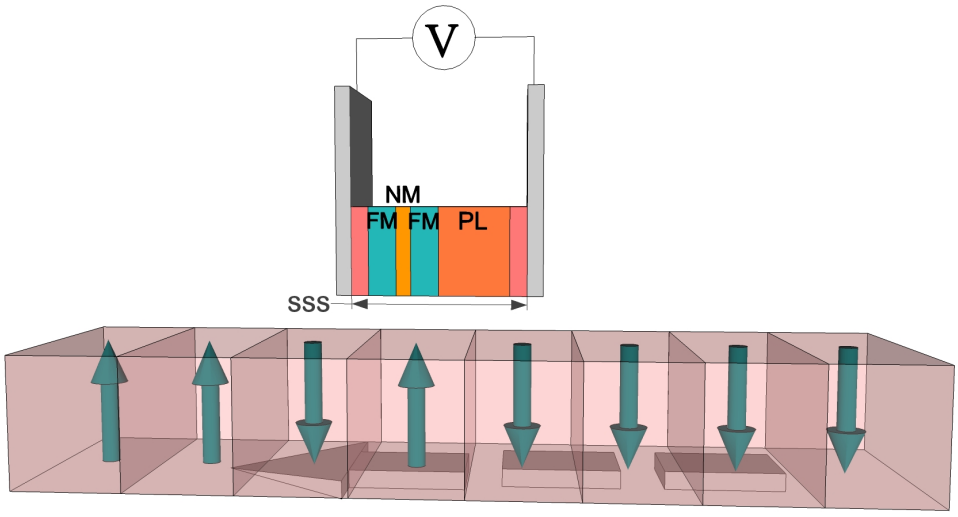

Figure 1.2: The schematic illustration of a read sensor of HDD. The moving magnetic media (the rotation direction is illustrated by an arrow pointing to the left) is composed of huge number of small magnetic grains. A group of several grains emanates stray magnetic field, either pointing upward or downward, representing one single bit of data. The magnetoresistive read sensor positioned right above magnetic media will change in resistance as the stray magnetic field tilt the relative orientation of two FM layers. In the generic structure of read sensor, the so-called spin valve, a pinning layer (PL) is used to fix the orientation of an adjacent FM layer (reference layer, RL), while the other FM layer is free to rotate (free layer, FL). The NM layer can be composed of either an insulating barrier or a metal. The total thickness of spin valve corresponds to the shield-to-shield spacing (SSS) of read sensors. The shield (most-left and most right) is typically made of soft magnets with high magnetic permeability such as NiFe (Permalloy or Py).

In 1995, another novel phenomenon observed in magnetic tunnel junctions (MTJs) composed of Fe/Al-O/Fe trilayer was reported [10, 11]. The effect coined as the tunneling magnetoresistance (TMR) is characteristically similar to the GMR effect as to its resistance change, but the former exhibits even higher magnitude of MR ratio. While the GMR effect lies in the spin-dependent transport of electrons in diffusive regime, the TMR effect is a quantum mechanical phenomenon of spin-dependent tunneling through a thin insulating barrier. Though the TMR effect had been immediately anticipated as a potential complementary or even a substitute for the GMR effect in various magnetic sensing applications, the most important impact of the TMR effect discovery is on the possibility of realizing a non-volatile memory, the so-called magnetic random access memory (MRAM) [12].

Further development on material research has resulted in the demonstration of symmetry filtering effect across crystalline MgO barrier that can exhibit TMR ratio higher than 100% [13,14]. Currently, MgO-based MTJs are being used in HDD read sensors as well as MRAM cells. Owing to the develop-

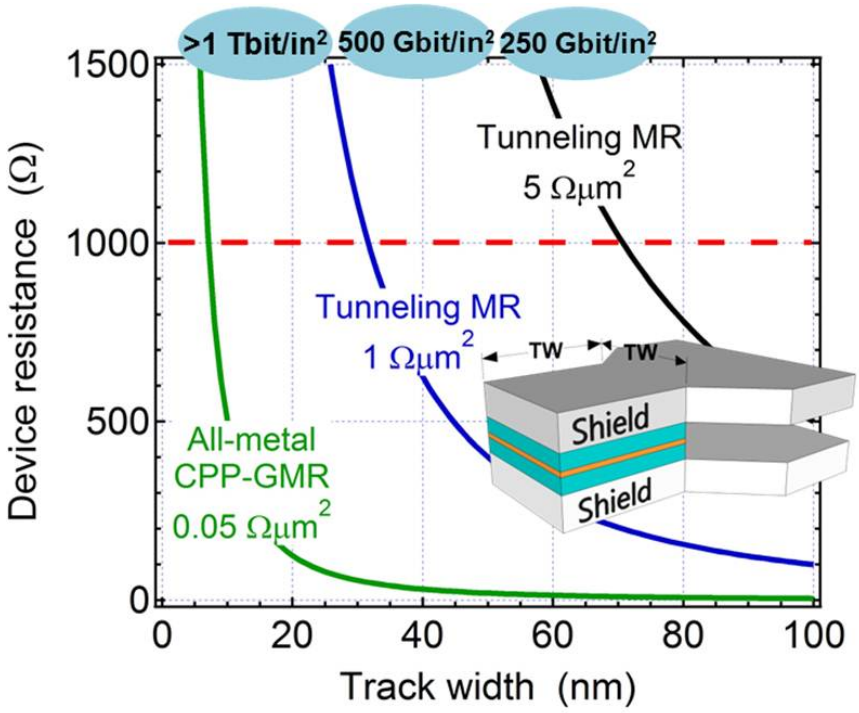

Figure 1.3: The calculated magnetoresistive device resistance for a given RA. Due to the ever increasing areal density, the trackwidth needs to be reduced and naturally leads to the increase in device resistance. The graph is reproduced from the presentation of Richard New of Hitachi Global Storage Technologies in 2008.

ment in thin film preparation very thin MgO barriers ≤ 1 nm can be prepared resulting in MTJs with RA of $1\Omega\mu\text{m}^2$ while at the same time preserving the high TMR over 100% [15]. As tera-bit scale HDD will be expected in a few years, the trackwidth of read sensor needs to be shrunk in order to realize the required high resolution read-out which consequently increases the resistance of corresponding devices (see Fig. 1.3). In order to keep the resistance of read sensor at certain values, the development of low RA MTJs is becoming very important.

The HDD industry has anticipated the limitation of TMR-based read sensor using MgO barrier as areal density of HDD is going beyond 1 Tbit/in^2 [16]. The current-perpendicular-to-plane giant magnetoresistive (CPP-GMR) devices has been long considered to be the most potential candidate to replace MgO-based MTJs in HDD read sensors [17,18]. The all-metallic structure of CPP-GMR devices which is an innately low-resistance device can realize the required fast operation of read-out process. The initial efforts have been started to improve the MR ratio of CPP-GMR devices which was too small compared to that of MgO-based MTJs, by the search for half-metallic FM and their incorporation into CPP-GMR devices [19,20]. Recent reports convincingly demonstrated the significant improvement on MR ratio of CPP-GMR devices by the use of highly spin-polarized Heusler alloys [21]. Nevertheless, there is considerable room for the MTJs to extend their sensing task in HDD industry. One of the potential approaches is by developing narrow band gap insulator that may realize low RA MTJs with high TMR ratio. This approach might open a new avenue for the development of barrier materials in the post-MgO era.

On the other hand, as the areal density will go further beyond 2 Tbit/in^2, the generic spin valve struc-

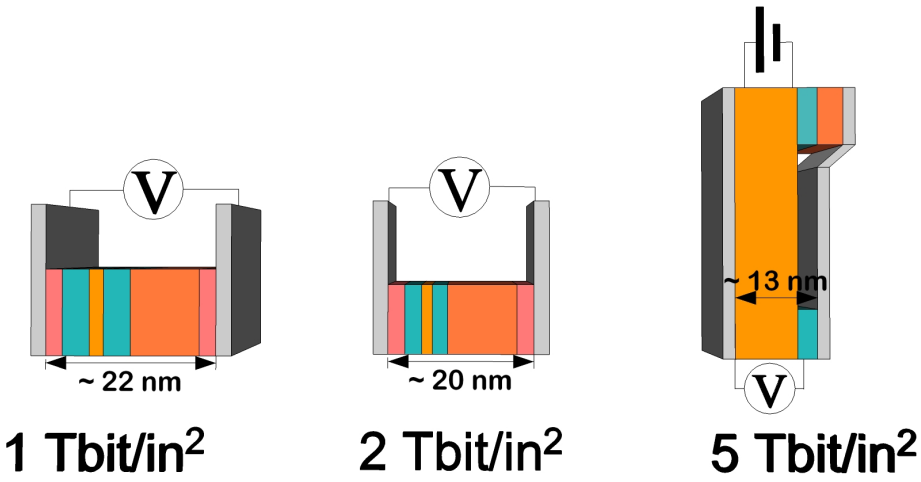

Figure 1.4: The schematic illustrations of dimensional change of read sensors as areal density increases. The generic spin valve structure (left and middle) may face the limitation in fulfilling the required narrow SSS for areal density beyond 2 Tbit/in^2. The proposed LSV-based read sensor (right) is proposed to possibly realize narrow SSS.

ture of read sensor will face another challenge in fulfilling the requirement for more narrow shield-to-shield spacing (SSS) of less than 20 nm [18]. In the spin valve structure, the pinning layer with at least 6 nm in thickness constitutes 20%-30% of the whole spin valve stack and is a limiting factor of the possible minimum SSS (Fig. 1.4). Therefore a dramatic change in the device structure of read sensor may be necessary in the near future to realize narrow SSS. One of candidates for ultra-narrow read sensors is the lateral spin valve in which the free layer is laterally separated from the reference layer and the pinning layer. The LSV may enable read sensors with SSS down to 13 nm, sufficiently thin to work in HDD with high areal density up to 5 Tbit/in^2 [22, 23]. Nevertheless, there is still long way to go for LSVs in order to be usable as read sensors considering its low output signals. Further development on materials and device structures might be required in order to realize practical LSV-based read sensors.

1.2 Spin injection and detection in magnetic heterostructures

In FM metals, such as Co, Ni, and Fe, due to the presence of exchange interaction the $3d$ bands of spin-up and spin-down electrons are shifted with respect to each other (see Fig. 1.5(a)) while the $4s$ bands remain unsplit. This phenomena induce the net magnetic moments inside the material and is the origin of finite magnetization in equilibrium state. In the early work of N.F. Mott [4], the electron conductivity of transition metals was hypothesized to be entirely dominated by the s electrons. This is mainly due to the much smaller effective mass of the s electrons than that of the d electrons. The spin-conserving electron scattering is proportional to the density of available states, so the electron transition from the s band (initial state) to the d band (final state) having greater DOS is the dominant factor dictating the scattering rate. Since the DOS of $3d$ bands at the Fermi energy is different for the two spin directions it consequently results in different scattering rates for spin-up and spin-down electrons, hence the corresponding conductivities. Therefore in FM metals electrons can be considered to flow in two independent channels, spin-up and spin-down channels.

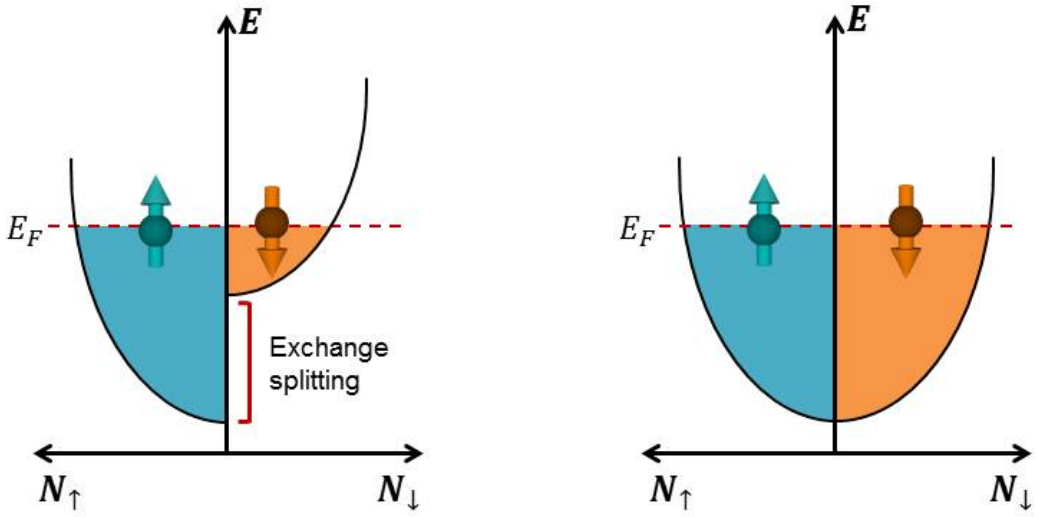

Figure 1.5: The schematic illustration of band structure of (a)FM and (b) NM metals.

Despite the absence of imbalance between spin-up and spin-down electrons in NM materials (see Fig. 1.5(b)), non-equilibrium spin states can be induced electrically. This concept of electrical spin injection, for the first time, was proposed by Aronov [24] and can be realized by injecting current through a contact of FM/NM as depicted in Fig. 1.6. Within the spin diffusion length, non-equilibrium states of spin-up and the spin-down electrons are induced and cause the change in the DOS of NM metals, virtually mimicking the DOS of FM. At the position longer than spin diffusion length, each spin-electrons relaxes towards the equilibrium state hence the DOS of NM recovers to the original state.

Johnson and Silsbee [25] experimentally demonstrated the concept of electrical spin injection using Al slab and Permalloy as NM channel and FM electrodes, respectively. In their pioneering work, two Permalloy electrodes were deposited on Al slab and laterally separated within a distance of several tens of micrometers. The function of another Permalloy electrode is to detect the traversing spin underneath. Despite the clear demonstration of spin injection and detection reported by Johnson and Silsbee [25], the signal detected at the detector electrode is very small of tens picovolt range and can only be observed at low temperature of 20-30K, partly due to the micron size of the device used in their experiment.

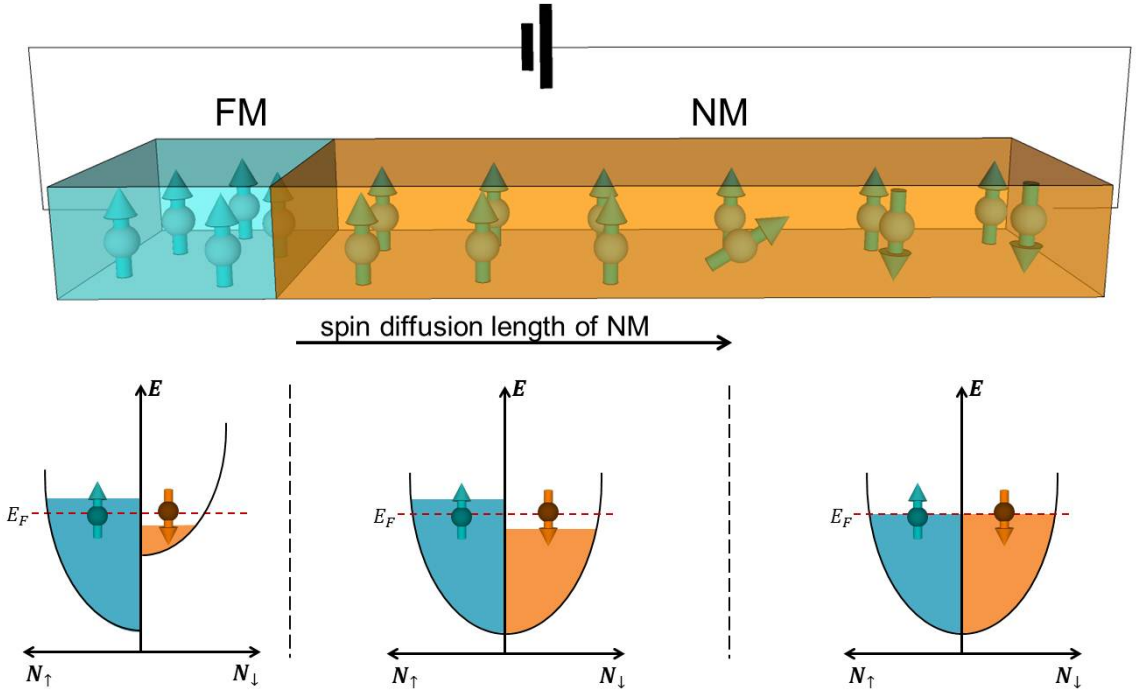

Figure 1.6: The schematic illustration of spin injection from an FM metal (blue slab) into an NM metal (brown slab). The corresponding band structures of FM and NM metals illustrating the spatial distribution of spin transport inside the magnetic heterostructure

In 2001, Jedema *et al* revisited the work on spin injection-detection in the all-metallic system [26]. Owing to the enormous development on nanostructures fabrication, mesoscopic devices were successfully prepared which enabled the significantly high spin signals measurable even at room temperature. The term of lateral spin valve was coined by the same authors to distinguish the unique geometry of the device and has been widely adopted in the spintronics research community, ever since. This report has re-spurred the attention to the original work of Johnson and Silsbee on spin injection and detection.

1.3 Lateral spin valves and half-metallic ferromagnets

1.3.1 The one-dimensional spin diffusion model

The derivation of one-dimensional spin diffusion model for lateral spin valves by Takahashi-Maekawa is adopted in this thesis. The device geometry is shown at the top side of Fig. 1.7 and basically the same as that used in Johnson-Silsbee experiment. The center-to-center distance of FM electrodes is denoted as d, while w_{FM}, w_{NM} and and t_{NM} correspond to width of FM wires, width of NM wires, and thickness of NM wires respectively. The electron current is typically injected from the left FM wire (FM 1) into the NM wire. The spin polarized current flows to the left part of NM wire. On the other hand, the net spin current flow to the right side of NM wire and once it reach the detector part (FM 2), the voltmeter will probe the chemical potential inside the FM wire relative to that in NM wire (bottom side of Fig. 1.7).

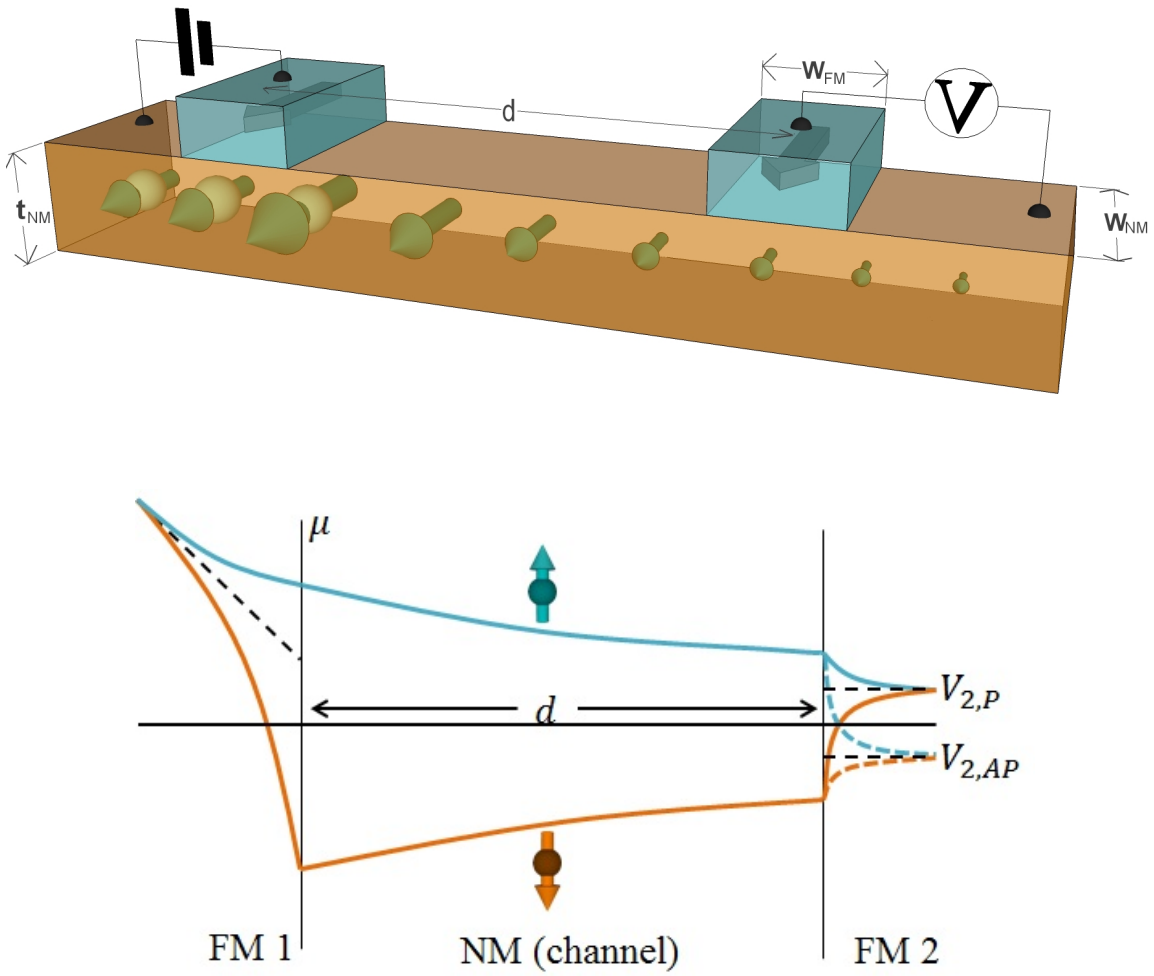

Figure 1.7: The generic structure of lateral spin valves with non-local measurement (top) and the corresponding electrochemical potential for up-spin and down-spin electrons (bottom).

In this and the following paragraphs, the derivation of one-dimensional spin diffusion model is described. To start with, the charge current density j_γ for each spin channel γ ($\uparrow$ or $\downarrow$) is expressed as

$$j_\gamma = \sigma_\gamma E - eD_\gamma \nabla \delta n_\gamma \tag{1.1}$$

where σ is the electron conductivity, E is the electric field, e is electron charge, D is the diffusion constant, $\delta \mathrm{n}_\gamma$ is the change in carrier density n_γ from equilibrium. The the first and second factor on the right part of the Eq. 1.1 correspond to the drift current and diffusion current respectively. Using Einstein relation $\sigma_\gamma = e^2 \mathrm{N}_\gamma D_\gamma$ and $\delta \mathrm{n}_\gamma = \mathrm{N}_\gamma \delta \epsilon_F^\gamma$ we have

$$j_\gamma = -(\sigma_\gamma / e) \nabla \mu_\gamma \tag{1.2}$$

where N_γ and μ_γ corresponds to the DOS and the electrochemical potential, respectively. In the

steady state the continuity equations for charge current j^{charge}= $j_\uparrow$+$j_\downarrow$ and spin current j^{spin}= $j_\uparrow$-$j_\downarrow$ are given as

$$\nabla(j_\uparrow + j_\downarrow) = 0 \tag{1.3}$$

$$\nabla(j_\uparrow - j_\downarrow) = -e\frac{\delta n_\uparrow}{\tau_{\uparrow\downarrow}} + e\frac{\delta n_\downarrow}{\tau_{\downarrow\uparrow}} \tag{1.4}$$

where $\tau_{\uparrow\downarrow}$ ($\tau_{\downarrow\uparrow}$) corresponds to scattering time of an electron from up-spin (down-spin) to down-spin (up-spin). Combining the continuity equation with the detailed balance, given as

$$\frac{N_\uparrow}{\tau_{\uparrow\downarrow}} = \frac{N_\downarrow}{\tau_{\downarrow\uparrow}} \tag{1.5}$$

the following basic equations can be obtained

$$\nabla^2(\sigma_\uparrow\mu_\uparrow + \sigma_\downarrow\mu_\downarrow) = 0 \tag{1.6}$$

$$\nabla^2(\mu_\uparrow - \mu_\downarrow) = \frac{1}{\lambda_{sf}}(\mu_\uparrow - \mu_\downarrow) \tag{1.7}$$

where λ_{sf} is the spin-difussion length. The time an electron travels before losing its spin information, i.e. the spin relaxation time τ_{sf}, is related to spin diffusion length as given below

$$\lambda_{sf} = \sqrt{D\tau_{sf}} \tag{1.8}$$

where

$$D = \frac{D_\uparrow D_\downarrow (N_\uparrow + N_\downarrow)}{N_\uparrow D_\uparrow + N_\downarrow D_\downarrow}, \quad \frac{1}{\tau_{sf}} = \frac{1}{2}\left(\frac{1}{\tau_{\uparrow\downarrow}} + \frac{1}{\tau_{\downarrow\uparrow}}\right)$$

The general solution of Eq.1.6 and Eq.1.7 for either an FM or an NM is given by [27, 28]

$$\mu_\gamma = A + Bx \pm \frac{C}{\sigma_\gamma} exp(-x/\lambda_{sf}) \pm \frac{D}{\sigma_\gamma} exp(x/\lambda_{sf}) \tag{1.9}$$

The coefficient A, B, C, and D can be deduced based on the boundary conditions at the interface of FM/NM. The first two factors on the right side of Eq. 1.9 correspond to the ground level of electrochemical potential and the additional potential coming from the applied external electric field, respectively. While the last two factors correspond to the electrochemical potential change due the the presence of spin-dependent transport. The sign of two last factors takes positive (+) and negative (-) for up-spin and down-spin electrons, respectively.

For the typical non-local LSV shown in Fig. 1.7 the solution for electrochemical potential inside the NM wire can be found to be

$$\mu^{\gamma}_{\mathrm{NM}} = \bar{\mu}_{\mathrm{NM}} \pm \left[a_1 exp(-\left|x\right|/\lambda_{NM}) - a_2 exp(-\left|x-L\right|/\lambda_{NM})\right] \tag{1.10}$$

where

$$\bar{\mu}_{\mathrm{NM}} = -\left[eI/(\sigma_{\mathrm{NM}} w_{\mathrm{NM}} t_{\mathrm{NM}})\right] x, \quad x < 0 \tag{1.11}$$

$$\bar{\mu}_{\mathrm{NM}} = 0, \qquad\qquad x > 0 \tag{1.12}$$

As the thickness and the length of FM wires are typically much longer than the typical spin diffusion length of FM materials, the electrochemical potential (in z axis direction) inside the FM wires can be written

$$\mu^{\gamma}_{\mathrm{FM},1} = \bar{\mu}_{\mathrm{FM1}} \pm b^{\gamma}_1 exp(-z/\lambda_{FM}) \tag{1.13}$$

$$\mu^{\gamma}_{\mathrm{FM},2} = \bar{\mu}_{\mathrm{FM2}} \mp b^{\gamma}_2 exp(-z/\lambda_{FM}) \tag{1.14}$$

where

$$\bar{\mu}_{\mathrm{FM},1} = -\left[eI/(\sigma_{\mathrm{FM}} w_{\mathrm{FM}} w_{\mathrm{NM}})\right] z + eV_1, \quad \bar{\mu}_{\mathrm{FM},2} = eV_2 \tag{1.15}$$

To determine a_1, a_2, b_1, b_2, V_1, and V_2 the boundary conditions such as the continuity of electron and spin currents at the FM/NM interfaces need to be imposed to Eqs. 1.10-1.15 [29]. In addition, it is wise to consider a general interfacial condition in that the resistive contact of FM/NM (R_i, where i corresponds to the junction 1 or 2) is assumed and it obeys the following boundary condition

$$R^{\gamma}_i = \frac{1}{eI^{\gamma}_i}\left(\mu^{\gamma}_{FM,i} - \mu^{\gamma}_{NM}\right) \tag{1.16}$$

The bottom side of Fig.1.7 shows the spatial distribution of electrochemical potential inside the LSV device for non-local spin injection(please note that the axis direction for FM and NM are different). Depending on the relative orientation of two FM wires, the voltage probed by the detector part can be expressed in the parallel state and the antiparallel state as $V_{2,\mathrm{P}}$ and $V_{2,\mathrm{AP}}$, respectively. The detected voltage difference between these two states normalized to the applied current I at the injector part is called the non-local spin signal and is given as

$$\Delta R_{\mathrm{S}} = \frac{V_{2,\mathrm{P}} - V_{2,\mathrm{AP}}}{I} \tag{1.17}$$

$$= 4R_{\mathrm{NM}} \frac{\left(\frac{P_{\mathrm{J},1}}{1-P^2_{\mathrm{J},1}}\frac{R_1}{R_{\mathrm{NM}}} + \frac{P_{\mathrm{FM}}}{1-P^2_{\mathrm{FM}}}\frac{R_{\mathrm{FM}}}{R_{\mathrm{NM}}}\right)\left(\frac{P_{\mathrm{J},2}}{1-P^2_{\mathrm{J},2}}\frac{R_2}{R_{\mathrm{NM}}} + \frac{P_{\mathrm{FM}}}{1-P^2_{\mathrm{FM}}}\frac{R_{\mathrm{FM}}}{R_{\mathrm{NM}}}\right) e^{\frac{-d}{\lambda_{\mathrm{NM}}}}}{\left(1 + \frac{2}{1-P^2_{\mathrm{J},1}}\frac{R_1}{R_{\mathrm{NM}}} + \frac{2}{1-P^2_{\mathrm{FM}}}\frac{R_{\mathrm{FM}}}{R_{\mathrm{NM}}}\right)\left(1 + \frac{2}{1-P^2_{\mathrm{J},2}}\frac{R_2}{R_{\mathrm{FM}}} + \frac{2}{1-P^2_{\mathrm{FM}}}\frac{R_{\mathrm{FM}}}{R_{\mathrm{NM}}}\right) - e^{\frac{-2d}{\lambda_{\mathrm{NM}}}}} \tag{1.18}$$

where $R_{FM} = \rho_{FM}\lambda_{FM}/A_J$ and $R_{NM} = \rho_{NM}\lambda_{NM}/A_{NM}$ are the spin resistance of FM and NM, respectively, while R_1 and R_2 are the contacts resistance of injector and detector respectively. The ρ, λ, and A correspond to resistivity, spin diffusion length, and effective cross section for spin current, respectively. The $P_{FM} = (\rho^{\uparrow}_{FM}\text{-}\rho^{\downarrow}_{FM})/(\rho^{\uparrow}_{FM}+\rho^{\downarrow}_{FM})$ and $P_J = (R_i^{\uparrow}\text{-}R_i^{\downarrow})/(R_i^{\uparrow}+R_i^{\downarrow})$ are the bulk and the FM/NM interfacial spin polarizations respectively.

The one-dimensional spin diffusion model is very useful in analyzing the spin-dependent transport properties of LVS through fitting the data of spin signals as a function two FM distances. Material parameters of interest such as P_{FM}, P_J, and also λ_{NM} can be deduced, given that other parameters are known. In addition, a simple calculation using this model can be done to know the possible spin signals that can be obtained under a certain condition (different material combinations, different device dimensions, etc.) given all parameters are known or reasonably assumed. Nevertheless, it should be noted that this model assumes the uniform current distribution across FM/NM interfaces which is unrealistic if the device dimension is too large or the FM/NM interfacial resistance R_i is too small, a situation that may not justify the use of this model for the fitting.

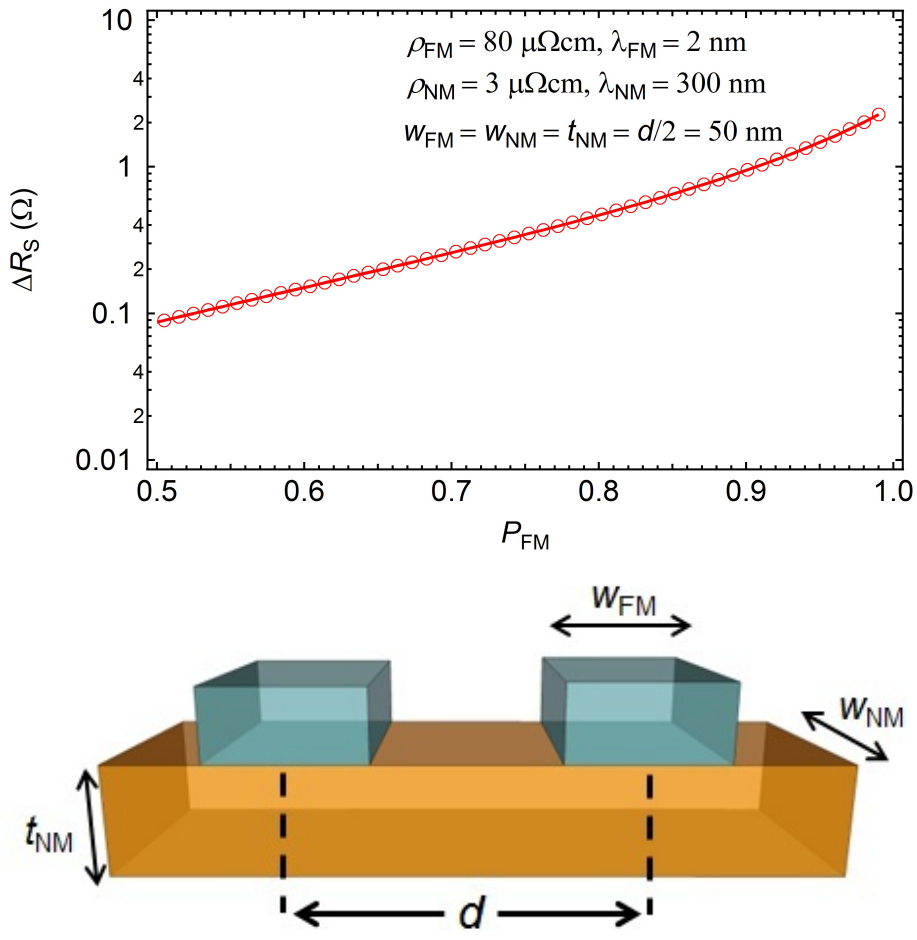

Figure 1.8: The calculated non-local spin signals ΔR_S as a function of effective spin polarization P_{FM} (top side) and the corresponding device dimensions (bottom side).

Here, an example of the use of the one-dimensional spin diffusion model is given. Figure 1.8 shows the calculated ΔR_S as a function of P_{FM} for the given materials parameters and device dimensions. In the

calculation, the transparent contact is assumed for the FM/NM interface. This case is very likely in the all-metallic LSVs, the system of interest for low RA and ultra-narrow read sensors. It can be seen that, the ΔR_S is (exponentially) proportional the P_{FM}. It should be noted that the ΔR_S is plotted in the logarithmic scale. The high P_{FM} can be realized by the use of FM materials having large difference of conductivity for up-spin and down-spin (please remember that $P_{FM} = (\rho^{\uparrow}_{FM}\text{-}\rho^{\downarrow}_{FM})/(\rho^{\uparrow}_{FM}+\rho^{\downarrow}_{FM})$). In an ideal case, the FM materials having a band gap at the Fermi level for only one spin direction can even realize the so-called half metals in which the $P_{FM} \approx 1$ hence giving the possible maximum spin signal. In the next subsection, the literature review on the half metallic FM is described.

1.3.2 Co-based Heusler alloys

In 1903, Friedrich Heusler reported on the existence of a unique compound [30], Cu_2MnAl, that exhibits ferromagnetism in spite of the absence of magnetic elements[1]. This first report stimulated further experimental and theoretical works on the so-called Heusler alloys, named after Friedrich Heusler, the inventor. The half-metallic property of Heusler alloys was firstly reported by de Groot *et al* who calculated the band structure of Mn-based Heusler alloys with the augmented-spherical-wave method [31]. A century after the first report by F. Heusler, various Heusler alloys with many different properties have been investigated and reported [32].

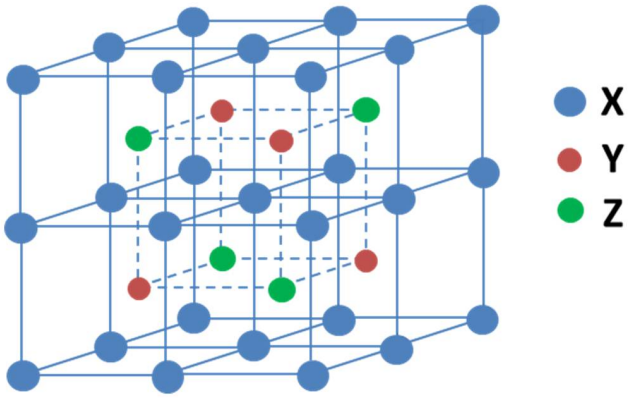

Figure 1.9: The schematic illustration of Heusler alloys with $L2_1$ atomic order

The so-called full-Heusler alloys have a general composition of X_2YZ, where X and Y are usually the transition elements (Co, Fe, Ni and Mn) and Z is the main group elements (Si, Al, Ga, Ge, etc). The structure of full-Heusler alloys can be described either as four interpenetrating fcc sublattices or a CsCl-like superstructure [32]. Fig 1.9 shows the generic structure of $L2_1$ atomic order. Of full-Heusler alloys, the Co-based ones for which Co atom occupies X sites are of practical interest due to the experimentally demonstrated high Curie temperature as well as theoretically predicted half metallicity [32].

Despite its predicted half-metallic property, no true half-metallic Heusler alloys have ever been reported. The perfect $L2_1$ atomic order, that have been found to be necessary in order to obtain the half-metallic property in Heusler alloys [33, 34], is very challenging to realize experimentally. The typically high annealing temperature $\geq$400°C is required [35, 36] in order to obtain highly ordered

[1] At the time of Heusler's first report, an element was supposed to have a spontaneous net magnetization in order to be classified as a magnetic element.

films, putting another constraint on how to realize the well defined multilayer stacks under such a process. Nevertheless, various spintronics applications can benefit from the significantly higher spin polarization of Heusler alloy over those of ordinary FM materials. Of several spintronics devices, current-perpendicular-to-plane giant magnetoresistive devices have been shown to greatly benefit from Heusler alloys [21]. The improved performance of CPP-GMR devices can lead to practical applications such as in read sensor of high density HDD [20, 37].

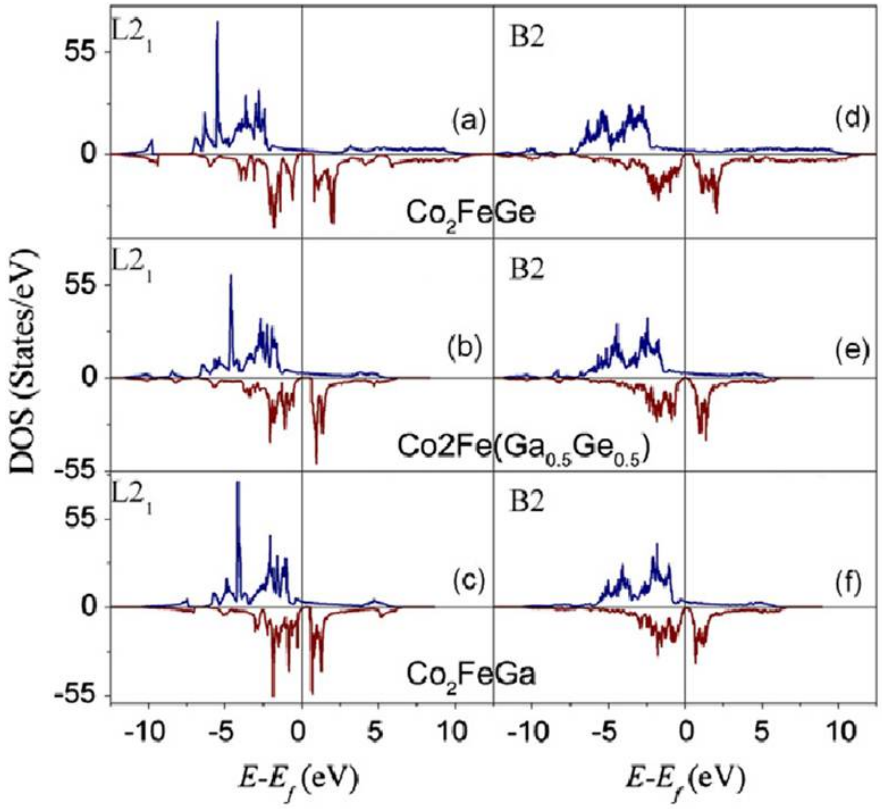

Figure 1.10: The calculated band structure of quaternary Heusler alloys $Co_2Fe(Ga_xGe_{1-x})$ with $L2_1$ and B2 atomic order(taken from [39])

Though in general Heusler alloys are ternary alloys, further tuning of material properties can be obtained by substituting one of the constituent elements (typically Y or Z site) with a different element hence forming quaternary alloys (see Fig. as an example). One of the consequences of forming quaternary alloys is the possibility of Fermi level tuning that enable us to shift the position of Fermi energy within band gap of minority spin [38, 39]. Another consequence is the band gap tuning that enables us to either widen or narrow the band gap of minority spins [38, 39]. Accordingly, by tuning the composition of quaternary alloys, further improvement especially on the spin polarization can be obtained [38, 39]. In our group, several quaternary Heusler alloys have been investigated (See Table 1.1). By point contact Andreev reflection indeed the quaternary ones exhibit higher spin polarization compared with those of ternary ones [39]. The highest record of MR ratio in CPP-GMR devices has been also reported by the use of quaternary Heusler alloys [40].

The high spin polarization of particular alloy compositions measured by PCAR, unfortunately, does not necessarily mean the corresponding magnetic devices would show a high performance, i.e., high

Table 1.1: The spin polarizations of Heusler alloys measured by point contact Andreev reflection. The preparation and characterization of samples were carried out at Research Center for Magnetic and Spintronic Materials of NIMS (taken from [39])

Quaternary alloys	P	T_C (K)	Ternary alloys	P	T_C (K)
$Co_2Mn(Ga_{0.75}Ga_{0.25})$	0.74	895	Co_2CrAl	0.62	600
$Co_2Mn(Ga_{0.5}Sn_{0.5})$	0.72	770	Co_2CrGa	0.61	-
$Co_2Fe(Si_{0.75}Ge_{0.25})$	0.70	990	Co_2MnSn	0.6	800
$Co_2Fe(Ga_{0.5}Ge_{0.5})$	0.69	1080	Co_2MnAl	0.6	-
$Co_2(Cr_{0.02}Fe_{0.98})Ga$	0.67	-	Co_2MnGa	0.6	700
$Co_2Mn(Ge_{0.25}Sn_{0.75})$	0.67	-	Co_2FeSi	0.6	1100
$Co_2(Mn_{0.95}Fe_{0.05})Sn$	0.65	-	Co_2FeAl	0.59	-
$(Co_{1.93}Fe_{0.062})MnGe$	0.68	-	Co_2MnGe	0.58	900
$Co_2(Mn_{0.5}Fe_{0.5})Ga$	0.7	990	Co_2FeGe	0.58	1000
$Co_2(Cr_{0.02}Fe_{0.98})Si$	0.65	990	Co_2FeGa	0.58	1100
$Co_2Mn(Ti_{0.25}Sn_{0.75})$	0.64	480	Co_2TiSn	0.57	364
$Co_2Mn(Al_{0.5}Sn_{0.5})$	0.63	-	Co_2MnSi	0.56	900
$Co_2Mn(Ga_{0.25}Si_{0.75})$	0.63	-	Fe_2VAl	0.56	-
$Co_2Mn(Si_{0.25}Ge_{0.75})$	0.63	-	Co_2VAl	0.48	-
$Co_2(Fe_{0.5}Mn_{0.5})Si$	0.61	-			
$Co_2Mn(Al_{0.5}Si_{0.5})$	0.60	-			
$Co_2Fe(Ga_{0.5}Si_{0.5})$	0.60	-			
$Co_2Fe(Al_{0.5}Si_{0.5})$	0.60	-			

MR ratio. It should be noted that a sample for PCAR measurement is basically prepared from a single bulk or thin film alloy [41]. Once this particular alloy is used in the corresponding magnetic devices other factors would affect the whole device performance, such as the degree of atomic order under a certain annealing process [35, 36, 42, 43], the lattice misfit with the adjacent layers [44–47], or the possible elemental inter-diffusion and degradation of layered structure upon annealing [48, 49]. Therefore, it is of great importance to find the right Heusler alloys that may form a well defined multilayer structure with high atomic order and sufficiently robust during preparation processes. The detail of physics may even be more complicated since certain Heusler alloys may have different levels of band matching at the interface with adjacent spacer/barrier materials [35, 50]. The termination layer and the corresponding exchange stiffness were also found to play an important role in affecting device performance [51–54].

1.4 Spin-dependent tunneling in magnetic tunnel junctions

1.4.1 Tunneling magnetoresistance effect

The early work on spin-dependent tunneling can be traced back in 1971 when Tedrow and Meservey reported their work on spin dependent tunneling spectroscopy in $Al/Al_2O_3/Ni$ junctions [55]. In 1975, Julliere reported the first observation of tunneling magnetoresistance effect in Fe/Ge/Co junctions that were measured at 4 K [56]. Due to the small TMR effect that can be observed only at low temperature and the difficulties in making high quality tunneling barrier, the research on this topic just received a little attention. Two decades later, Moodera [10] and Miyazaki [11] reported the observation of giant TMR effect at room temperature in Fe/Al-O/Fe. The arising interest in GMR effect in early 90s readily made the TMR effect to be one of the central issues after the report of Moodera and Miyazaki.

In the classical mechanics, a moving particle cannot pass the potential barrier unless its energy is higher than the potential energy of that barrier. In the quantum mechanical picture, however, a small particle such as electron can have a finite probability to pass through the barrier having a higher potential energy through the so-called quantum tunneling effect. The quantum tunneling effect can be observed and studied in a solid state device comprised of a thin insulating barrier sandwiched by two metallic electrodes, the so-called tunnel junction shown in Fig. 1.11. Within the free electron model, the transmission probability of tunneling across the insulating barrier is given as

$$T(E) \approx exp\left(-2\int_0^t \sqrt{2m_e\left[U(x)-E\right]\hbar^2}dx\right) \tag{1.19}$$

where t, m_e, $U(x)$,and E correspond to the barrier thickness, the electron mass, the barrier potential energy, and the electron energy, respectively. Suppose that the barrier potential hardly change with x, $U(x) \approx U$, the difference between barrier potential and electron energy U-E can be defined as the barrier height ϕ. Accordingly the transmission probability as a function of the barrier thickness t and the barrier height ϕ can be simplified into

$$T(t,\phi) \approx exp\left(-t\frac{\sqrt{8m_e\phi}}{\hbar}\right) \tag{1.20}$$

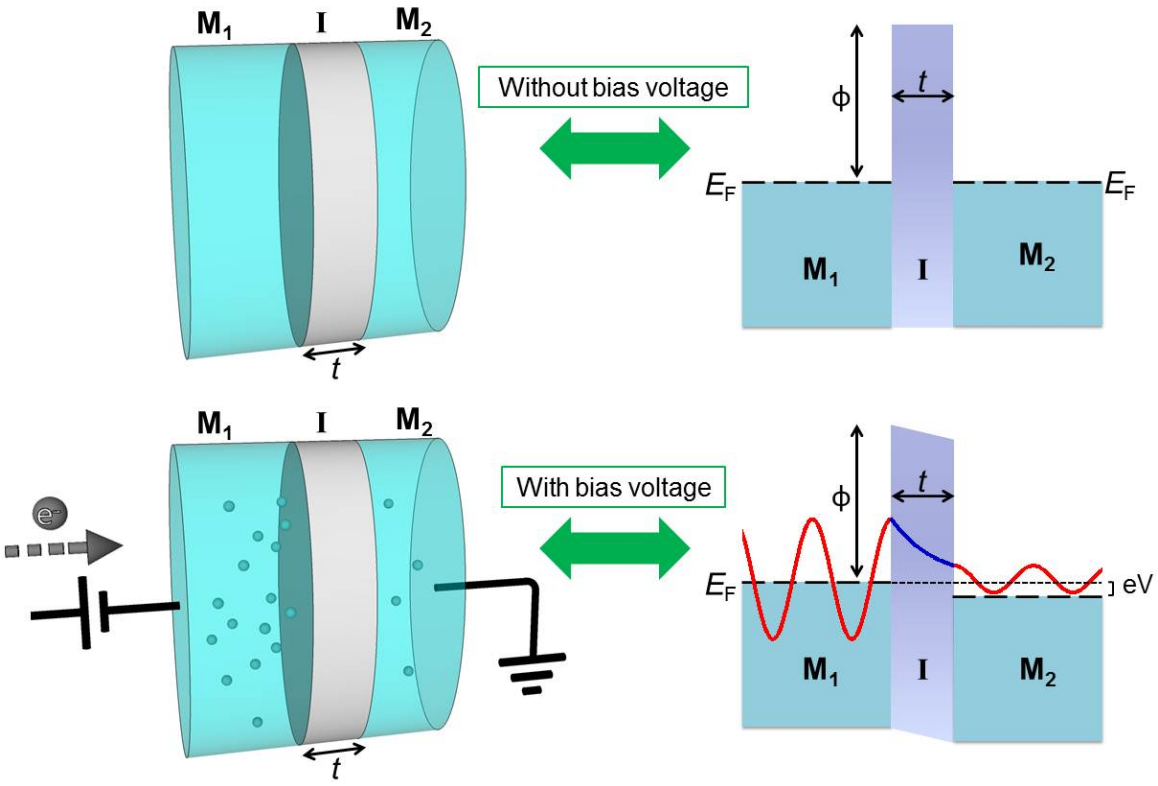

Figure 1.11: The schematic illustration of a tunnel junction, metal/insulator/metal (M/I/M), and the corresponding energy band diagram without and with the application of external bias voltage

Figure 1.11 shows the schematic illustrations of the energy band diagram in a tunnel junction without (top) and with (bottom) the presence of bias voltage. When the tunnel junction is not biased, the

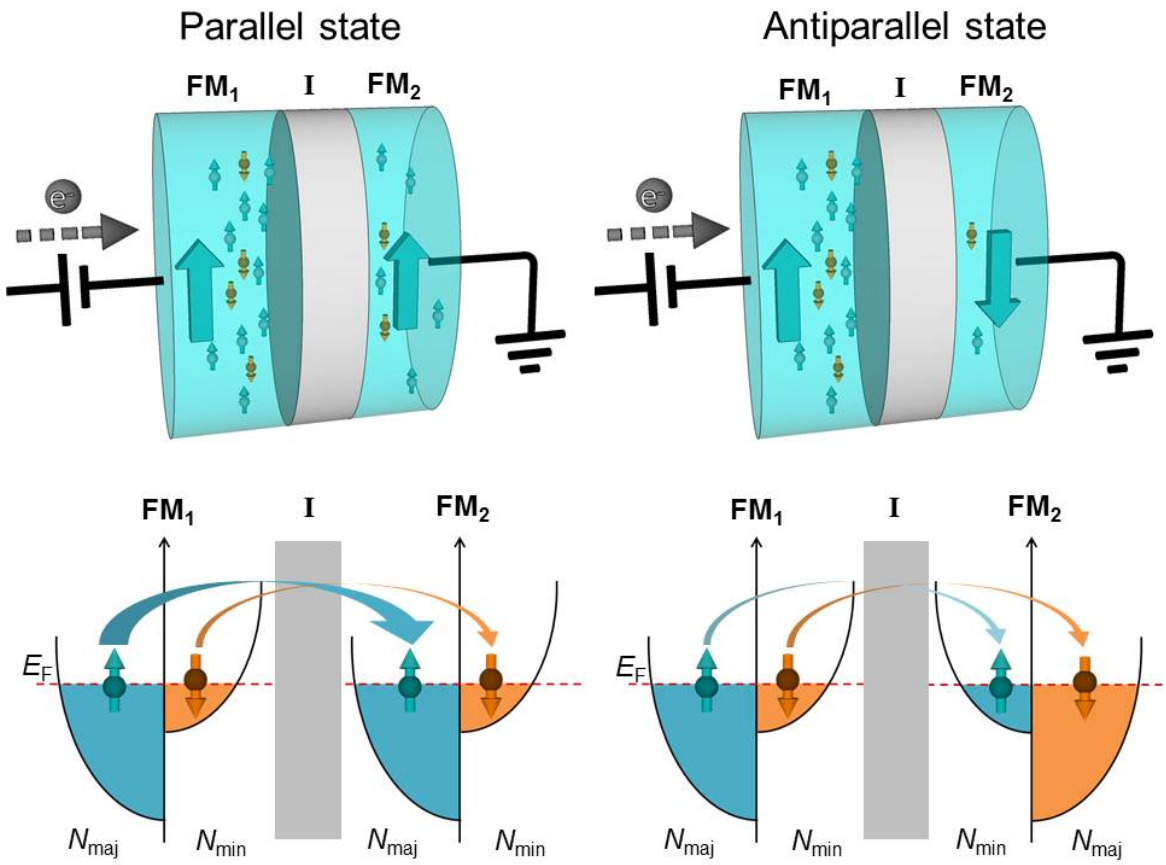

Figure 1.12: The schematic illustration of a magnetic tunnel junction, FM/I/FM, and the corresponding energy band diagram for the P and AP states

Fermi energy of two metallic electrodes would align at the same level and there would be no tunneling across the barrier. If a certain bias voltage V is applied across the tunnel junction as schematically shown in bottom side of Fig 1.11, the Fermi level of the right electrode M_2 is lowered by eV relative to the Fermi level of the left electrode M_1. Accordingly, the electron states of M_1 is in higher potential energy than those of M_2 leading to the quantum tunneling of electrons from the filled states of M_1 into the unoccupied states of M_2.

A simple analytic calculation of tunneling current through a tunnel junction within the assumption of $eV \ll \phi$ would lead to the simple expression of tunneling conductance given as

$$G \propto N_1(E_F)N_2(E_F)T(t,\phi) \tag{1.21}$$

where $N_{1,2}(E_\mathrm{F})$ is the DOS at Fermi level for each metal electrode. In the experiment, the tunneling conductance of a tunnel junction can be obtained by calculating the first derivative of the I-V curve, dI/dV.

Suppose that FM metals are used as electrodes, the so-called magnetic tunnel junction (MTJ) can be created (top side of Fig. 1.12). In the MTJ, we need to consider the difference in the DOS of up-spin and down-spin electrons in affecting the total tunneling current. Since in FM metals the electrons flow independently through up-spin and down-spin channels, the total tunneling conductance of MTJs is simply the summation of these two channels :

$$G = G_{\uparrow} + G_{\downarrow} \propto N_1^{\uparrow}(E_{\mathrm{F}})N_2^{\uparrow}(E_{\mathrm{F}}) + N_1^{\downarrow}(E_{\mathrm{F}})N_2^{\downarrow}(E_{\mathrm{F}}) \tag{1.22}$$

Here we need to consider the respective total conductance for different relative magnetization orientation of two FM electrodes; the parallel (P) and antiparallel (AP) states. Defining that the majority (minority) channel corresponds to the spin channel having higher (lower) DOS and parallel (antiparallel) with the magnetization of an electrode (see bottom side of Fig.1.12), the total tunneling conductance for the P and AP states can be written respectively

$$G_{\mathrm{P}} \propto N_{\mathrm{maj}}(E_{\mathrm{F}})N_{\mathrm{maj}}(E_{\mathrm{F}}) + N_{\mathrm{min}}(E_{\mathrm{F}})N_{\mathrm{min}}(E_{\mathrm{F}}) \tag{1.23}$$

$$G_{\mathrm{AP}} \propto N_{\mathrm{maj}}(E_{\mathrm{F}})N_{\mathrm{min}}(E_{\mathrm{F}}) + N_{\mathrm{min}}(E_{\mathrm{F}})N_{\mathrm{maj}}(E_{\mathrm{F}}) \tag{1.24}$$

where $N_{\mathrm{maj,min}}(E_{\mathrm{F}})$ corresponds to the DOS for either majority or minority spin channel at the Fermi level. Considering that $\mathrm{N_{maj}}(E_{\mathrm{F}}) > N_{\mathrm{min}}(E_{\mathrm{F}})$ it can be readily anticipated that $G_{\mathrm{P}} > G_{\mathrm{AP}}$ indicating the difference in tunneling conductance depending on the relative magnetization orientation of two electrodes. This phenomena is widely called as the TMR effect which can be observed in the MTJ under the application of external magnetic field that can switch the relative magnetization orientation from P to AP state or vice versa. The typical TMR curve that can be obtained through the electrical measurement of the MTJ is shown in Fig. 1.13.

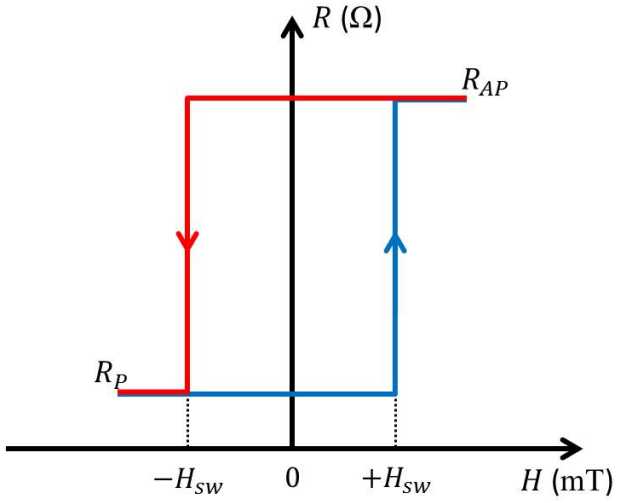

Figure 1.13: The typical TMR curve which can obtained by applying external magnetic field to the MTJ and measuring its resistance. H_{SW} corresponds to the switching field of an FM electrode, namely the free layer.

The widely used quantitative expression representing the degree of resistance change in MTJs is the so-called TMR ratio given as

$$\text{TMR ratio} = \frac{G_{\mathrm{P}} - G_{\mathrm{AP}}}{G_{\mathrm{AP}}} = \frac{R_{\mathrm{AP}} - R_{\mathrm{P}}}{R_{\mathrm{P}}} \tag{1.25}$$

This expression is basically the same as the MR ratio used for giant magnetoresistance effect.
Julliere proposed the expression of TMR ratio in relation with the spin polarization of each FM electrode P_{FM} [56]

$$\text{TMR ratio} = \frac{2P_{\mathrm{FM},1}P_{\mathrm{FM},2}}{1 - P_{\mathrm{FM},1}P_{\mathrm{FM},2}} \tag{1.26}$$

$$P_{\mathrm{FM}} = \frac{N_{\uparrow}(E_{\mathrm{F}}) - N_{\downarrow}(E_{\mathrm{F}})}{N_{\uparrow}(E_{\mathrm{F}}) + N_{\downarrow}(E_{\mathrm{F}})} \tag{1.27}$$

Due to its simplicity and straightforward relation with the spin polarization, the Julliere model has been widely used to analyze the TMR effect in various combination of FM electrodes and insulating barriers [10, 57–59].

1.4.2 Symmetry filtering effect in MgO barrier

The rich physical phenomena in spin-dependent tunneling have been attracting wide interest in spintronics community [59]. The high TMR ratio as a manifestation of highly spin-polarized tunneling across the barrier is desired for applications such as magnetic sensors and memory cells in MRAM. The mostly investigated barrier in 90's was amorphous Al-O [59, 60]. The high TMR ratio up to 70% can be achieved at room temperature using amorphous Al-O barrier, sufficiently high to fulfill the requirement of HDD [61] and MRAM [62] with relatively low capacity. With the increasing demand on the ever increasing capacity of data storage and memory, the higher TMR ratio that cannot be achieved with amorphous Al-O barrier is indispensable. On there hand, the use of highly spin-polarized Heusler alloys can only give a giant TMR ratio at low temperature [58, 63], hindering the possibility to use this unique class of materials in combination with amorphous Al-O barrier for practical applications.

In 2001, Butler et al [64] and Mathon et al [65] independently reported the symmetry filtering effect across (001) MgO barrier with Fe electrodes that may lead to the giant TMR ratio over 1000%. In MgO barrier, the evanescent states of different symmetry tunnel at different decay rates, hence coined the symmetry filtering effect. The states with Δ_1 symmetry dominate the tunneling due to the slowest decay rate (Fig. 1.14(a)). Fortunately, in Co_xFe_{1-x} as well as Co-based Heusler alloys the Δ_1 band of majority spin crosses the Fermi level(Fig. 1.14(b)), while that of minority spin does not, leading to the half-metallic nature for this particular band. Accordingly, in the P state the up-spin electrons (majority spin states in both electrodes) of Δ_1 band dominate the whole tunneling current(Fig. 1.14(c)). While in the AP state up-spin electrons of Δ_1 band essentially should not exist at the other electrode (become minority spin states in one of the electrodes), hence significantly suppressing the tunneling current. In 2004, two independent groups successfully prepared polycrystalline CoFe/MgO [13] and epitaxial Fe/MgO [14] , respectively, that exhibit TMR ratio higher than 100%, confirming the theoretical work on the symmetry filtering effect in MgO. These two reports have spurred great interest on the investigation of MgO-based MTJs.

Of particular interest is the CoFeB/MgO system that was reported to show a high TMR ratio at room temperature [66]. The possibility of growing CoFeB/MgO stacks on amorphous substrates is a big ad-

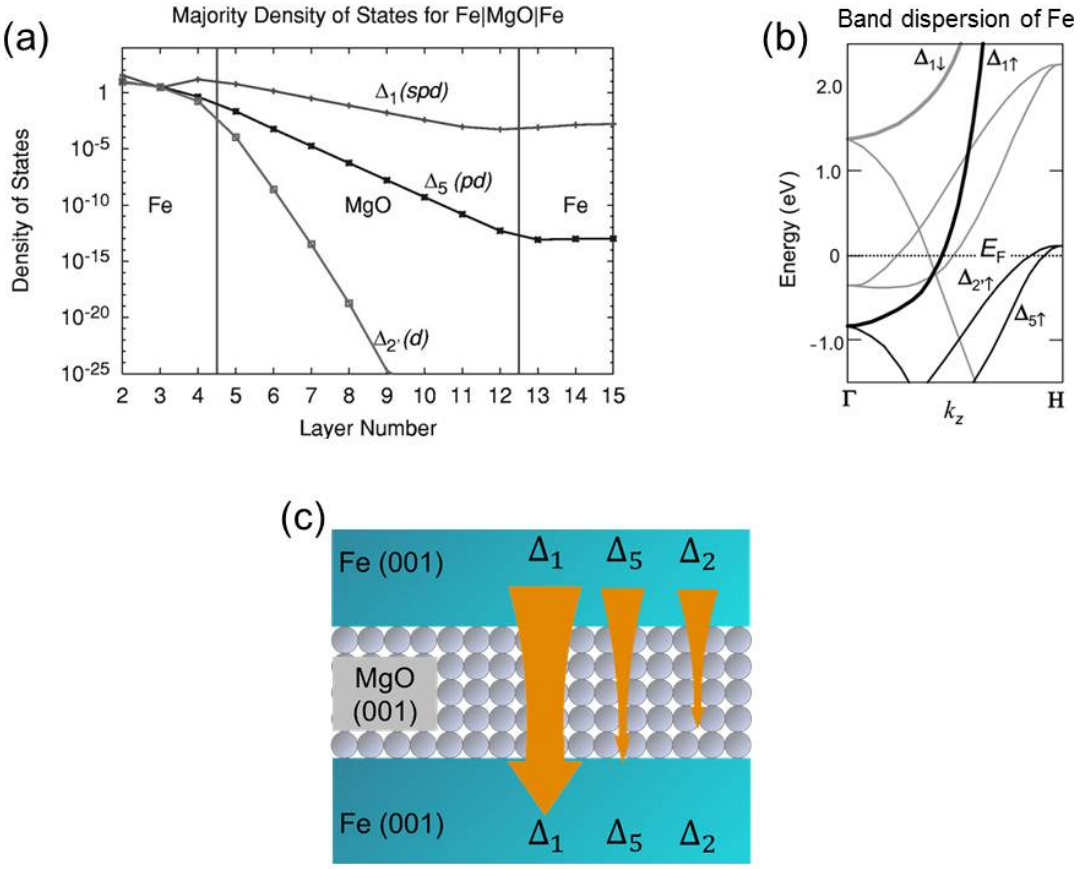

Figure 1.14: (a) Due to the symmetry filtering effect, the evanescent states with Δ_1 symmetry dominate the tunneling across the MgO barrier, while other states with Δ_5 and $\Delta_{2'}$ symmetries decay at much faster rate (taken from[64]). (b) According to the band structure of Fe electrodes, Δ_1 band is fully spin polarized at Fermi level (taken from[60]). (c) The schematic illustration of symmetry filtering effect in Fe/MgO MTJs (for the P state) which can lead to the high TMR ratio.

vantage over epitaxial MTJs that require the use of expensive single crystal substrates. In fact, further development has demonstrated the superiority of the CoFeB/MgO system over epitaxial MgO barrier regarding the TMR ratio value (Fig. 1.15). The wide interest in CoFeB/MgO has stimulated a large amount of research and progressed the understanding on the physics of symmetry filtering effect as well as polycrystalline thin films [60]. The phenomena of Boron diffusion into Ta upon post-annealing was found to be the key to obtain the grain-to-grain epitaxial growth between eventually-crystallized CoFe and highly-textured MgO (Fig. 1.16) [67–69]; a prerequisite for Δ_1 symmetry filtering effect. As high as 600% of TMR ratio at room temperature was reported [70], showing the promising potential of CoFeB/MgO for practical applications. Nowadays, the CoFeB/MgO system has been widely used as read sensors in HDD and cells in spin-transfer-torque MRAM [16, 60, 71].

One of the key factors in MgO-based MTJs is the possibility to tune theRA value that may vary depending on the specific applications. The RA of tunneling devices can be easily tuned by varying the barrier thickness [72] (see Fig.1.17). For both read sensors in HDD and cells in STT-MRAM, the ever increasing capacity trends require low RA below 10 $\Omega\mu\text{m}^2$ [15,73], which typically corresponds to barrier thickness less than 1 nm (5 monolayers). While Butler *et al.* indeed predicted the decreasing

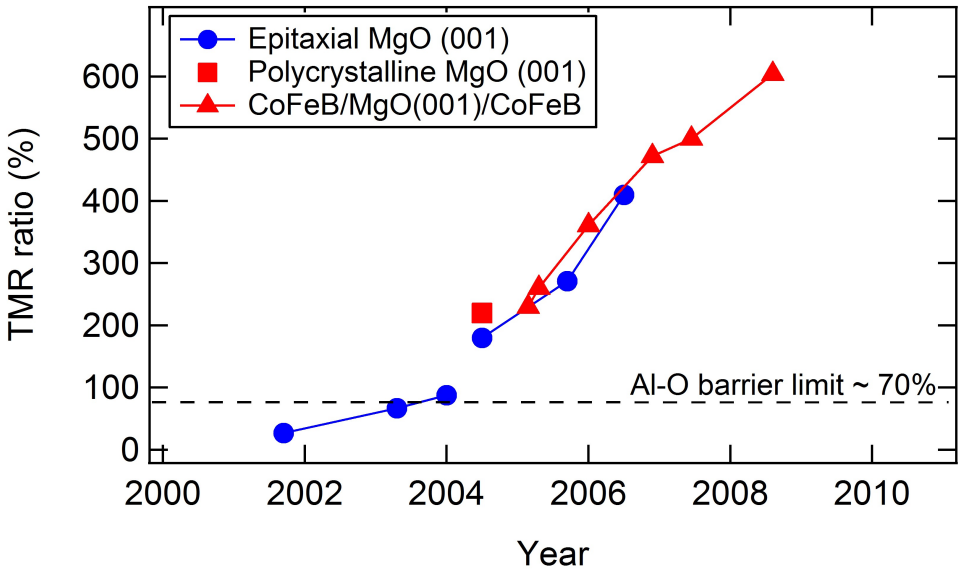

Figure 1.15: The development of MgO-based MTJs showing giant TMR ratio at room temperature over the years. The dashed line indicates the limit of amorphous Al-O barrier that can just achieve TMR ratio of 70%. The CoFeB/MgO can be seen to achieve the highest record of TMR ratio around 600% at room temperature

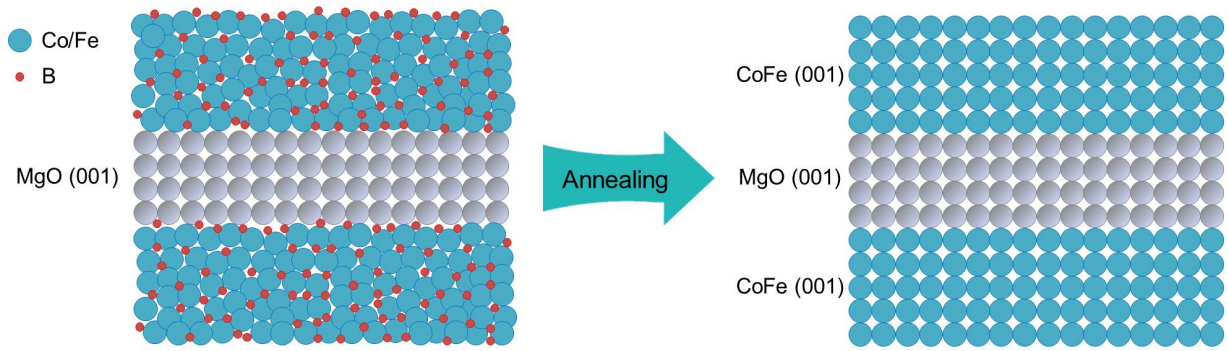

Figure 1.16: The schematic illustration of microstructure evolution upon annealing treatment in CoFeB/MgO MTJs

TMR ratio with decreasing MgO barrier thickness [64], in the real MTJ stacks the drop of TMR ratio might be more severe due to extrinsic factors such as microstructures in very thin MgO barriers. This microstructure issues can manifest as a low degree of MgO texture, rough MgO barrier, the presence of pinholes, and so on. These all not only would lead to the lower TMR ratio, but also lower break-down voltage of MTJs, which is detrimental for device endurance.

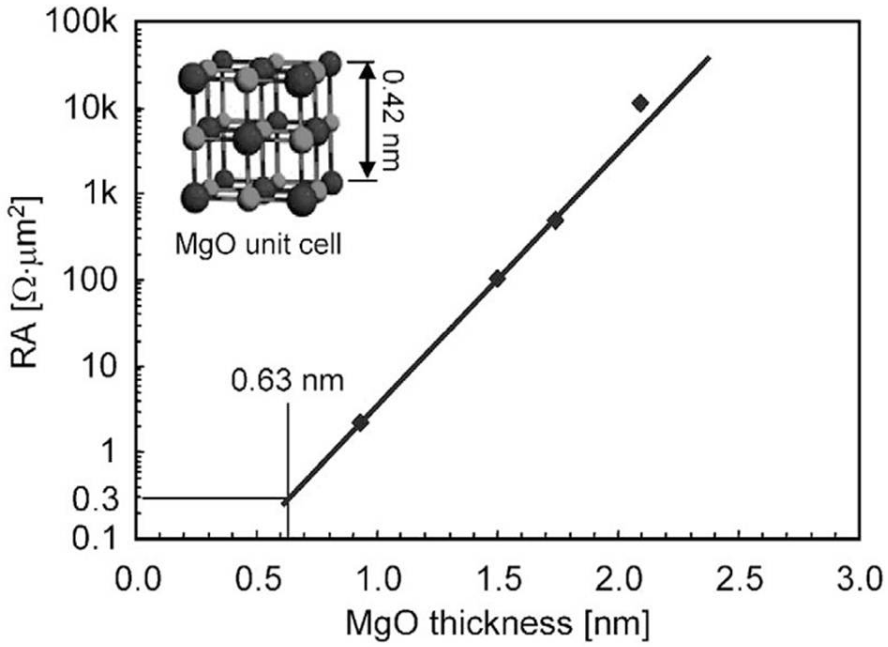

Figure 1.17: The *RA* as a function of barrier thickness for MgO-based MTJs with CoFeB electrodes (taken from [72]).

1.5 Outline of thesis

This thesis titled "Spin-dependent Transport in Magnetic Heterostructures : Ohmic and Tunneling Regimes" is aimed to tackle the issues on the ever shrinking read sensor of HDD with high areal density ≥ 1 Tbit/in^2. The near future HDD technology may see not only a gradual transition from insulating barriers to semiconducting and metallic spacers, but also a dramatic change in the device structure of read sensors. In this thesis, the development of barrier materials with narrow band gap is proposed as an alternative to the widely-used MgO barriers in MTJs-based read sensors. On the other hand, the lateral spin valve structure is demonstrated as a potential alternative to resolve the issue on the physical dimension of generic spin valve structures that might not be able to realize ultra-narrow read sensors.

Chapter 1 is started with the overview on the spintronics research and its impact on the development of magnetic storage technology. The future trend of magnetic storage technology, particularly regarding the development of read sensors is described. The literature review on the one-dimensional spin diffusion model and spin-dependent tunneling mechanism in LSVs and MTJs, respectively, and the corresponding material development associated with these two devices is also given in this chapter. The brief description on the sample preparation and characterization is given in chapter 2.

In chapter 3, the investigation on the transport and microstructure properties of CoFeB/$Mg_{1-x}Ti_xO$ MTJs ($x = 0.05$ and 0.1) is described. The barrier height tuning by substituting Mg with Ti is successfully demonstrated and analyzed based on the Wenzel-Kramer-Brillouin model. The observation of high TMR ratio in CoFeB/$Mg_{1-x}Ti_xO$ MTJs especially for low *RA* devices is the central part of discussion in this chapter. The $Mg_{1-x}Ti_xO$ films was found to grow with (001) out-of-plane texture on the amorphous CoFeB even in the as-deposited state. Upon annealing, the similar microstructure

evolution to that in CoFeB/MgO can be seen in CoFeB/$Mg_{1-x}Ti_xO$ MTJs. This chapter essentially demonstrate the proof of concept of band gap tuning in alloyed/doped MgO barrier to realize low RA MTJs with high TMR ratio.

In chapter 4, the extensive work on the microfabrication process to realize $Co_2Fe(Ga_{0.5}\ Ge_{0.5})$/Cu LSV devices with clean interfaces by a fully top-down process is described. An alternative route for the realization of $Co_2Fe(Ga_{0.5}Ge_{0.5})$/Cu LSVs by the top-down microfabrication process is demonstrated. The dependence of the microfabrication reliability on the choice of cap layer materials was systematically investigated, underlining a challenge in realizing clean FM/NM interfaces in an LSV by the top-down process.

In chapter 5, the temperature dependence of magneto-transport properties of $Co_2Fe\ (Ga_{0.5}Ge_{0.5})$/Cu LSVs is described. The fitting of the d dependence of the spin signals using the one-dimensional spin diffusion model confirms that the effective spin polarization of $Co_2Fe(Ga_{0.5}Ge_{0.5})$ is significantly higher than that of other Heusler alloys incorporated in LSVs, at both room temperature and low temperature. The non-local spin signals are found to exhibit a non-monotonic trend with decreasing temperature at the low temperature range below 50 K . The fit based on the one-dimensional spin diffusion model reveals that the spin diffusion length of Cu exhibits a slight downturn at 36 K and mainly dictates the observed non-monotonic trend in non-local spin signals at low temperatures.

In chapter 6, the summary of the works reported in this thesis is described. The future direction for further works is also given in this chapter.

Chapter 2

Experimental method

This chapter is devoted to briefly describe the experimental equipments and processes used for preparing and charaterizing the lateral spin valves and magnetic tunnel junctions.

2.1 Multilayer deposition

The main deposition system used in our group is classified as physical vapor deposition (PVD). In PVD, the target material that would be deposited is treated under physical process such as heating and sputter. The target materials is in general solid and under physical treatment the phase will change to vapor (quasi-vapor). Due to the kinetic energy it has, the vapor moves towards the specific surface (substrate) at which it will be deposited and returns to solid. For the preparation of thin film in our group, two of PVD systems, e.g. magnetron sputter and electron-beam evaporation, were used. The detail working principle will be described in the following subsections.

2.1.1 Magnetron sputter

The sputter is one of the most-widely used PVD systems in thin film manufacturing. Various materials such as metals, semiconductors, and insulators can be deposited even with atomically-controlled capability. Sputter refers to the process of forcing out an atom from the surface by striking particles with sufficient kinetic energy. The striking particles used is usually generated by plasmas that will ionize certain gas such as Ar, O2, Kr, etc. Under the influence electric field, the particles will move to a certain direction dependent on their charge polarity. The widely used sputters usually has a magnetron which is a permanent magnet system attached below the cathode. The magnetron is design in such a way to exhibit magnetic flux parallel to the surface of material target so that secondary electrons can be controlled to create a closed-loop path and further enhancing the yield of sputter.

Figure 2.1 depicts the schematic diagram of basic magnetron sputter. It is assumed that the gas used is Ar. Upon plasma generation, Ar^+ ions are generated and are moved towards materials target following the electric field direction. As Ar^+ ions hit target atoms, energy/momentum transfer takes place and target atoms can be forced out from the lattice if the energy is large enough to break the bonding with neighboring atoms.

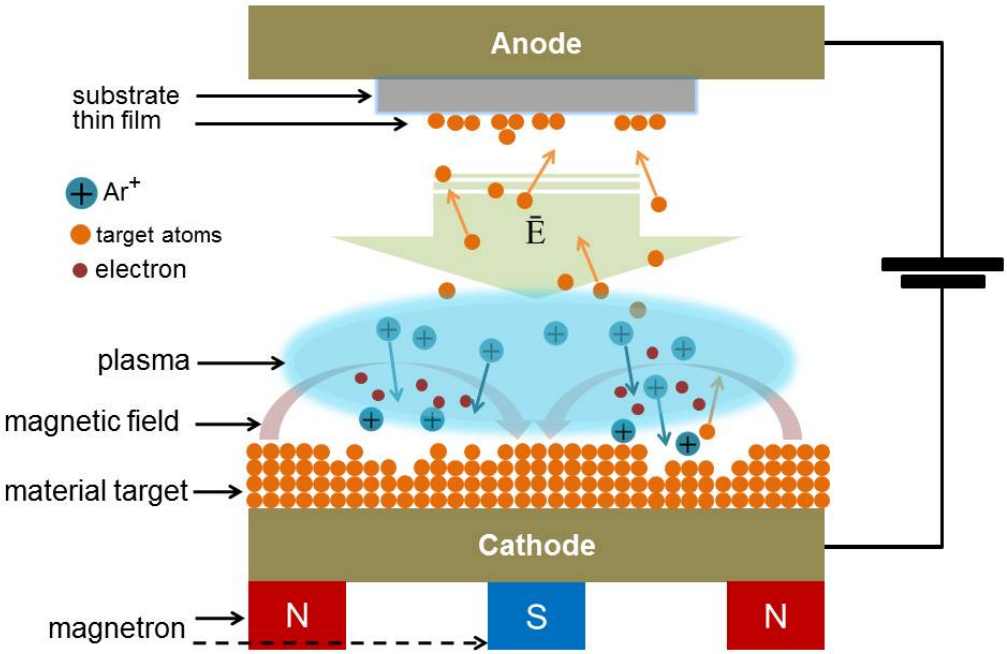

Figure 2.1: The schematic illustration of material deposition by magnetron sputter

2.1.2 Electron beam evaporation

The electron beam evaporation is one of PVD techniques that utilizes electrons bombardment to evaporate the material target. The electron beam is typically generated by thermionic emission of heated filaments. The material target is typically in the form of pellets having specific size and shapes and is put on a crucible typically made of Ta or Tungsten. Sufficient vacuum condition of the chamber is necessary to suppress the interaction between electron beam and residual gas and to ease the evaporation process. The schematic illustration of working mechanism of electron beam evaporation is depicted in Fig. 2.2. The electron beam gains kinetic energy under the application of accelerating voltage and moves towards the material target through a circular path as a consequence of the magnetic force induced by the magnetic field. Upon the bombardment, the kinetic energy of electron beam is converted to thermal energy which will heat up the material target. Over time the heat builds up and increases the temperature of material, which further melts the material specifically at the surface area. Under sufficient vacuum condition the material starts to evaporate. The evaporated material will sublimate into solid once it reaches the substrate or chamber wall. Since the chamber is in vacuum, the evaporated material can travel with long mean free path even without collision with residual gas. This means evaporated materials practically travel with straight trajectories towards the substrate, which makes evaporation technique suitable for lift-off process. In this thesis, electron beam evaporation was used to deposit Cu and MgO onto substrate through a resist mask.

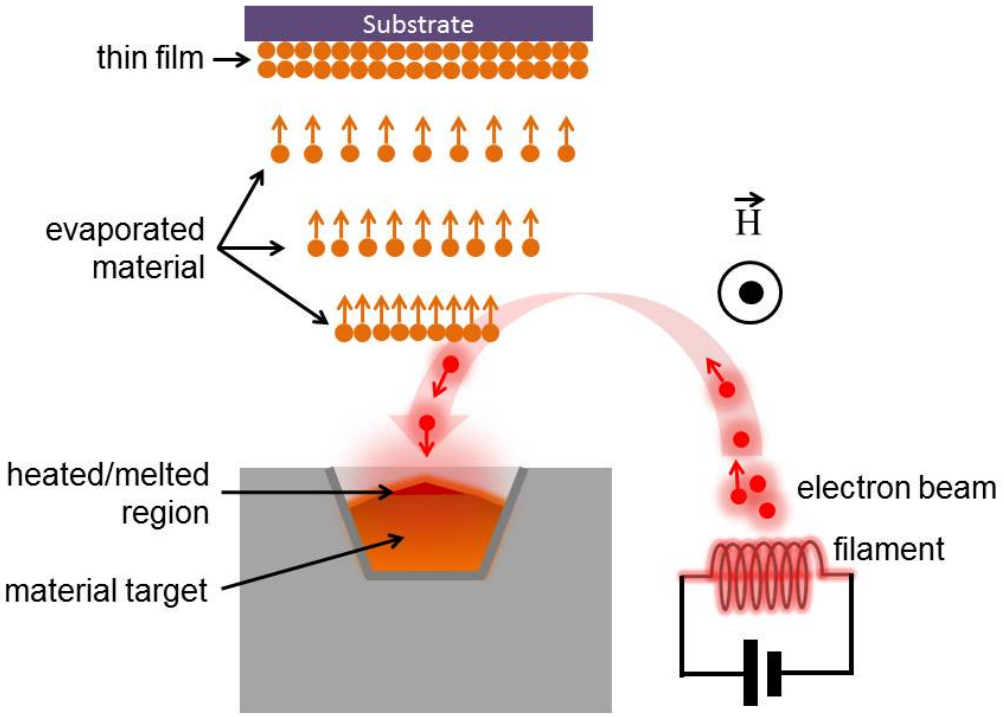

Figure 2.2: The schematic illustration of material deposition by electron beam evaporation

2.2 Microfabrication

2.2.1 Optical lithography

The optical or photo-lithography is one of the most fundamental technology for device microfabrication. It is a process of transferring the geometric patterns onto the resist via the exposure of a certain range of optical wavelength through a photo mask. The resist for optical lithography is usually a liquid solution that is light-sensitive. The micron to sub-micron thick resist is typically coated on the substrate or thin films to be patterned by using a spin coater equipment. The resist are classified into two main groups, i.e. positive tone and negative tone resists. For the positive(negative) tone resist, the portion that is exposed to the light becomes (remains) soluble (insoluble) under development process, while the unexposed portion remains (becomes) insoluble (soluble). The resist should be stable and tough enough after development process in order to maintain its shape and dimensions during the next process such as film deposition (lift-off process) or milling (top down process).

2.2.2 Electron beam lithography

The electron beam lithography is one of lithography techniques that utilizes highly-focused electron beam to make specified patterns on the resist. The electron beam is generated with a relatively similar process to that in the scanning electron microscope, i.e. thermionic emission. Upon entering the resist, the primary incident electrons would undergo forward scattering and transfer their energy to the resist. In addition, back-scattered electrons could be generated if the electrons deeply penetrating the resist are back-scattered by the substrate or thin film. Inelastic collisions of primary incident electrons could

also induce ionization that would generate secondary electrons. As the by-product of primary incident electrons, the back-scattered and secondary electrons could distort the initially-defined exposure area leading to less controllability in the patterning process. Similar to the resist for optical lithography, the resist used for electron beam lithography can be classified into negative tone and positive tone resists. The optimization of exposure condition, coating process of resist, and resist development plays an important role in creating well-defined patterns. In the experiment described in this thesis, the micro-resist 2403^{TM} and *poly-methyl-metacrylate* (PMMA) were used as negative and positive tone resists, respectively. The JEOL electron beam lithography JBX-6300 was used to perform the electron beam exposure.

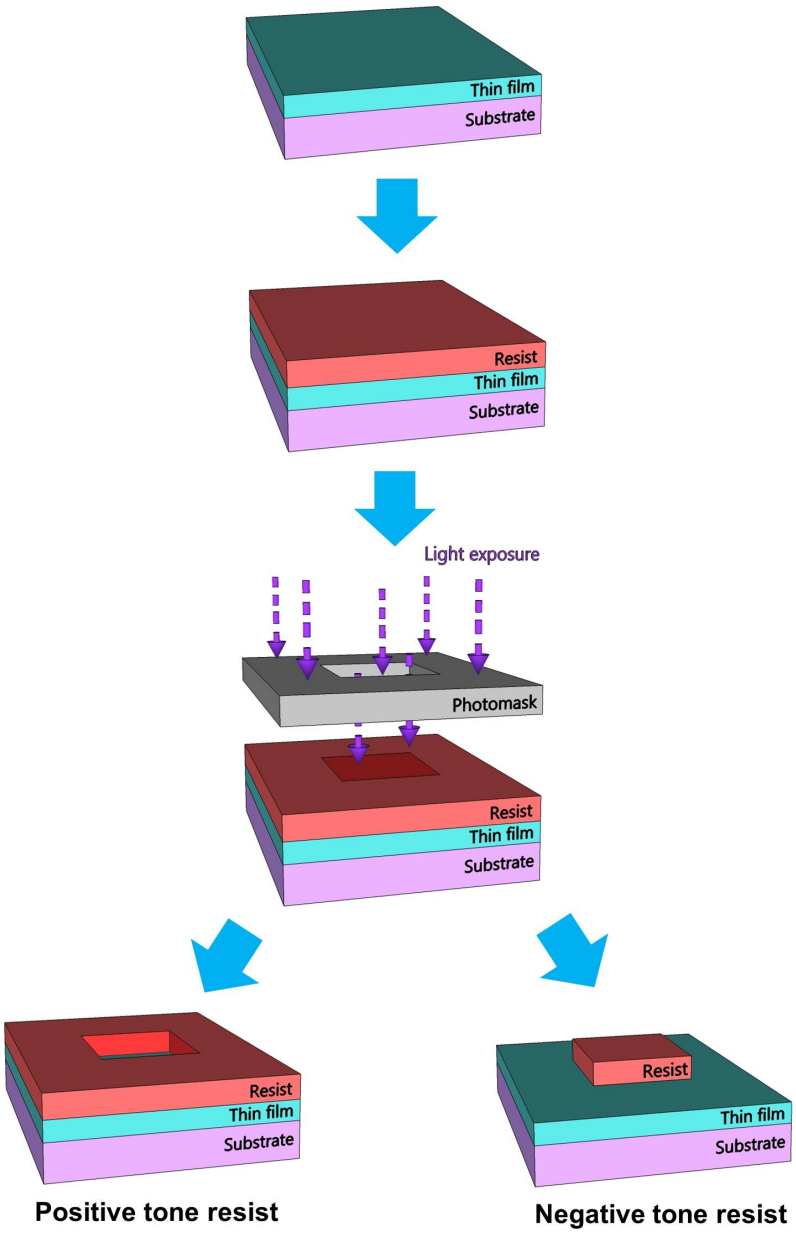

Figure 2.3: The schematic illustration of optical lithography using two different resists. In the electron beam lithography a photo mask is not required, instead the electron beam will scan the surface of the sample just like a drawing process using a pen.

2.3 Thin film and device characterization

2.3.1 X-ray diffraction

The Rigaku X-Ray diffraction machine was used for structure characterization of thin film samples. The XRD machine is equipped with the 2-dimensional detector and the Cu source X-ray generator having wavelength of around 1.54Å. The use of 2-dimensional detector enables the simultaneous acquisition of 2-dimensional intensity map of 2θ and ω scans.

2.3.2 Atomic force microscopy

The characterization of the surface property, in particular the morphology, of thin films is very important to preliminarily clarify their quality. In general, the well-defined and flat interfaces in magnetic heterostructure are required. Accordingly, this indicates the pivotal role of immediate surface characterization in the optimization process of thin film preparation. The atomic force microscope (AFM) produced by Seiko Instrument Inc. was used for this purpose. The AFM would give 1-dimensional to 3-dimensional morphology of the thin film surface with typical scan area of $(0.2\text{-}10)^2 \mu\text{m}^2$.

2.3.3 Scanning electron microscopy

In investigating the particular transport properties of magnetic heterostructures, the thin films typically need to be fabricated into micro- and nano-structured devices with a specific shape. The immediate and practical characterization to preliminarily confirm the success of microfabrication process is necessary. For this purpose, the scanning electron microscope (SEM) produced by Carl-Seizz Instrument was used for surface characterization of devices. The shape and dimensions of devices can be directly confirmed with the SEM. This information is also very important in analyzing the transport properties in the device.

2.3.4 Transmission electron microscopy

The FEI Titan G2 80-200 transmission electron microscopy was used to observe the cross section of magnetic heterostrcutures. The specimen for TEM observation was prepared by the focused ion beam, which is called lift-out method. Using FIB, a very thin specimen down to 100 nm can be prepared. The specimen can be taken from either bare thin films or corresponding devices.

2.3.5 Electrical measurement

The magneto-transport properties of magnetic heterostructure were typically measured by DC 4-probe method. The current is typically injected through the device and the voltage is subsequently measured. During the measurement, the device is placed between two poles of coils that generate external magnetic field. For the measurement at varying temperature of 5 K - 300 K, the device is measured inside a small vacuum chamber that has a sample chip stage connected to the cryogenic system. This small vacuum chamber is placed between two poles of electromagnetic coils that generate the uniform external magnetic field.

Chapter 3

Magnetic tunnel junctions with rock-salt-type $Mg_{1-x}Ti_xO$ barriers

3.1 Introduction

Since the first prediction of giant tunneling magnetoresistance (TMR) in the crystalline MgO barriers [64,65] and the experimental demonstration of TMR over 180% in CoFe/MgO/CoFe [13] and single crystalline Fe/MgO/Fe [14], the development of MTJs has progressed rapidly especially for practical spintronics applications. The main advantage of MgO-based MTJs is that the MgO barrier thickness can be tuned for obtaining wide range of resistance-area product (RA) while keeping the high TMR over 100% [15,74]. Further development of terabit-scale hard disk drives (HDD) and gigabit-scale magnetic random access memory (MRAM) requires MTJs with RA lower than 10 $\Omega\mu m^2$ [15, 73], which is very challenging for MgO considering its relatively wide band gap and consequently high barrier height. In addition, the requirement for very thin MgO barriers of 1 nm in order to achieve the low RA values will put another question on the reliability issue, since for such thin oxides high voltage stress may lead to the lower breakdown voltage of barriers [75]. Alternative barrier materials which can tackle the above mentioned issues should be developed in order to maintain the extendability of MTJs technology in the future.

Doping impurity elements into MgO can be considered to be one of the possible ways to intrinsically tune its band gap. Liu *et al* reported the theoretical study on doping effect of various impurity elements into MgO to the spin-dependent transport in Fe/doped-MgO/Fe MTJs [76]. The authors had found that Al, Ti, and Zn dopants effectively reduce RA of doped-MgO MTJs [76], but at the same time rapid decrease in TMR arises except for the Mg-Zn-O [77]. While a single phase is possibly to be obtained for wide range of Zn concentration, the Mg-Zn-O would form a wurtzite structure with increasing Zn concentration, which is considered to be detrimental for the coherent tunneling . On the other hand, the Mg-Fe-O barrier, which was reported to have higher TMR ratio than the MgO barrier in the corresponding MTJs, showed the problem of the solubility limit resulting in dopants segregation [78]. Thus, it is still desired to find out proper impurity elements that can intrinsically change the band gap of barrier materials and at the same time can preserve the spin filtering effect across the junction.

Here, the $Mg_{1-x}Ti_xO$ (or MTO) is proposed as alternative barriers with more narrow band gap com-

pared to that of MgO, hence possibly realizing low RA MTJs. Previous reports have shown that MTO films has a rock-salt structure and forms a stable phase with just a slight change of lattice constant compared to that of MgO for wide range of Ti-rich compositions [79, 80], making it possible to preserve the coherent tunneling effect across the barrier as in the case of MgO barrier. The wettability of ferromagnetic layer on top of MTO films was also reported to be much better than that on top of MgO ones [79], which will give the opportunity for realizing very thin ferromagnetic electrodes with perpendicular anisotropy required for MRAMs cells [81].

In this chapter, the investigation on the transport and microstructure properties of MTO-based MTJs is described. The MTO films was found to grow with (001) out of plan texture on amorphous CoFeB even in the as-deposited state. This enable the realization of epitaxial growth relation at barrier/ferromagnet interfaces upon annealing the multilayer stack just like in the case of CoFeB/MgO MTJs. The TMR of MTO-based MTJs was found to decrease with increasing Ti concentration and significantly lower than that of MgO-based MTJs for devices with RA higher than 5 $\Omega\mu m^2$. For RA lower than 5 $\Omega\mu m^2$, however, the MTO-based MTJs show higher TMR ratio compared to that of MgO-based ones. The introduction of Ti into MgO is found to decrease the barrier height and significantly reduce the RA of MTJs for a given thickness.

3.2 Experiment

The MTJ stacks of Si-SiO_2 subs./Ta(5)/Ru(10)/Ta(5)/$(Co_{25}Fe_{75})_{85}B_{15}$(5)/MgO or $Mg_{1-x}Ti_xO$ (0.5-1.9)/CoFeB(4)/Ta(5)/Ru(5, thickness in nm) were prepared by using RF/DC magnetron sputter at room temperature. Barriers were deposited from sintered targets and pure Argon was used as the sputter gas. The actual compositions of the 200-nm-thick films deposited from $Mg_{0.9}Ti_{0.1}O$ and $Mg_{0.8}Ti_{0.2}O$ targets were determined to be $Mg_{0.95}Ti_{0.05}O$ and $Mg_{0.9}Ti_{0.1}O$, respectively, by using inductively coupled plasma (ICP) analysis. Accordingly, the Ti concentration x prepared in this work corresponds to $x = 0.05$, and 0.1. The wedge-shaped barriers were deposited by a linearly moving shutter.

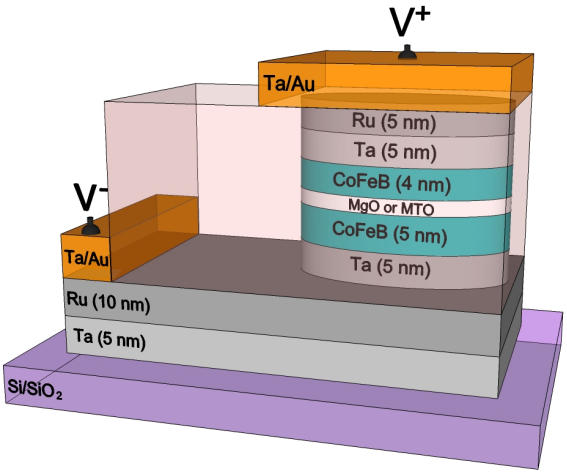

Figure 3.1: Schematic of multilayer stacks and the MTJ device.

The MTJ stacks were fabricated into (elliptical and rectangular) pillar devices with sizes ranging from 200×100 nm^2 to 400×200 nm^2 by using electron beam lithography and Argon-ion milling. The MTJ devices were post annealed at 300°C-500°C for 30 minutes in a vacuum-based furnace without applying magnetic field. The measurement of zero-bias TMR ratio was performed by the four-probe method at room temperature with bias voltage of 0.1-2 mV. On the other hand, the temperature dependence of transport measurement was performed by the four-probe method in a cryogenic chamber at temperature range of 10 K - 275 K. For microstructure characterization, the FEI Titan G2 80-200 scanning transmission electron microscopy (STEM) equipped with Cs-corrector for illumination, electron energy loss spectroscopy (EELS), and energy dispersive X-ray spectroscopy (EDS) were used. The corresponding specimen for microstructure characterization was prepared by lift-out technique using focused ion beam (FIB).

3.3 TMR ratio and microstructures

Figures 3.2(a)-(c) show the TMR ratio as a function of RA in the parallel state for MTJs with MgO, $Mg_{0.95}Ti_{0.05}O$, and $Mg_{0.9}Ti_{0.1}O$ barriers, respectively, which were annealed at different temperatures and were measured at room temperature. It can be seen that the TMR ratio of MTJs with three different barriers generally increases with increasing annealing temperature up to 450°C. The TMR ratio of MgO-based MTJs is clearly seen to be higher than that of MTO-based ones for RA higher than 5 $\Omega\mu m^2$ for all range of annealing temperatures. In general, the trend shows that TMR ratio drops with increasing Ti concentration. The high TMR ratio over 100% for MTO-based MTJs suggests that symmetry filtering effect, to a certain degree, still preserves across barriers even in the presence of Ti dopants. The fact that the TMR ratio decreases with decreasing RA, which is a direct consequence of decreasing thickness of barriers, is in good agreement with the theoretical study [64]. On the other hand, the TMR ratio of MTO-based MTJs surpasses that of MgO-based ones at RA lower than 5 $\Omega\mu m^2$ for all annealing temperatures.

Figure 3.2(d) shows RA in the parallel state as a function of barrier thickness for MTJs annealed at 300°C. It can be seen that indeed MTO-based MTJs show lower RA for a given thickness, which is a consequence of the intrinsically lower barrier height resulting from narrow band gap of MTO. It is of fundamental interest to quantitatively clarify the change of barrier height in $Mg_{1-x}Ti_xO$ for varying Ti concentration. The slope α of $\ln(RA/\Omega\mu m^2)$ as a function of barrier thickness, according to Wenzel-Kramer-Brillouin (WKB) approximation, is proportional to $4\pi(2m^*\phi)^2/h$, where m^*, ϕ, and h are the effective electron mass, barrier height, and Plancks constant, respectively [14]. Since the decrease of the slope is observed with increasing Ti concentration (Fig.3.2(d)), the barrier height is likely to decrease. Assuming that $m^* \approx m_e$, free electron mass, the ϕ of $Mg_{0.95}Ti_{0.05}O$ and $Mg_{0.9}Ti_{0.1}O$ is estimated to be 0.45 eV and 0.4 eV, respectively, which are slightly smaller than $\phi_{MgO} = 0.59$ eV.

Black arrows in the Figs. 3.2(a)-(c) indicate the point of critical RA below which the TMR rapidly decreases and the trend fall on a single line regardless of annealing temperatures. The critical RA value decreases with increasing Ti concentration. Previous report has suggested that up to 4 monolayers (0.85 nm) MgO barriers form amorphous structure [74]. The critical RA value of MgO-based MTJs in the current study corresponds to barrier thickness of around 0.9 nm which is quite close to the critical thickness for obtaining crystalline MgO barrier in the previous report [74]. The critical RA of

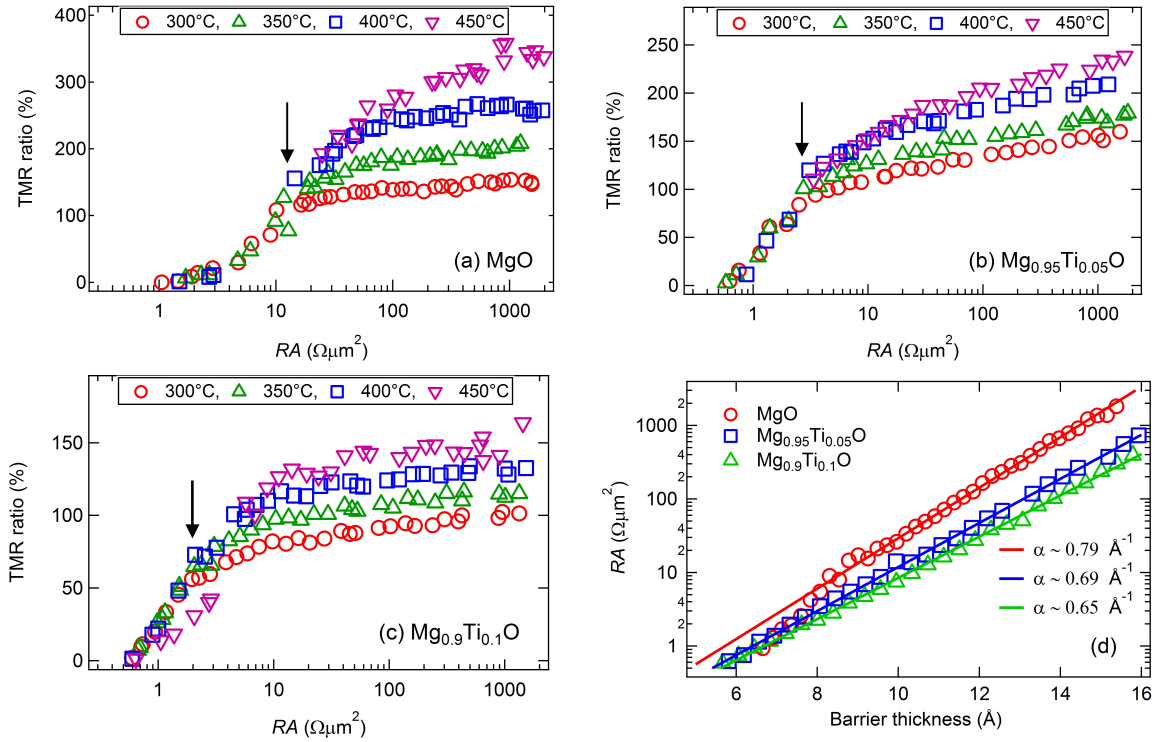

Figure 3.2: TMR ratio as a function of RA in the parallel state for MTJs with barrier composed of (a) MgO, (b) $Mg_{0.95}Ti_{0.05}O$, and (c) $Mg_{0.9}Ti_{0.1}O$. (d) RA in the parallel state as a function of barrier thickness for MTJs post-annealed at 300°C. The lines are fit to the WKB model and the slope α of $\ln(RA/\Omega\mu m^2)$ for each barrier is also shown.

MgO-based MTJs can be seen to coincide with the marked change in the trend of RA-t in Fig. 3.2(d), which is correlated with the critical thickness for obtaining crystalline MgO barrier and is possibly the origin of rapid decrease in the TMR ratio below this RA. On the other hand, the lower critical RA for MTO-based cannot be solely attributed to the thicker barriers compared to that of MgO-based ones. In contrast to MgO-based MTJs, RA for MTO-based ones still falls on the same trend line even below the critical RA range, suggesting no dramatic microstructure change appears within the range of barrier thicknesses prepared in this experiment. It is speculated that the introduction of Ti into barrier may result in a better wettability [79, 82] hence preserving the high crystallinity and suppressing the presence of pin holes for very thin MTO barriers. It accordingly may explain the higher TMR ratio of the MTO-based MTJs compared with that of the MgO-based MTJs at RA range lower than $5\Omega\mu m^2$.

It was previously reported that upon annealing the (001) texture of MgO barriers will improve, while initially amorphous CoFeB electrodes will crystallize into CoFe with (001) texture, leading a grain-to-grain epitaxy with orientation relation of (001)[110]MgO//(001)[100]CoFe [69, 70]. Consequently the microstructure requirement for the coherent tunneling is fulfilled [64, 65], leading to high TMR ratio upon annealing. The MTJs with MTO barriers can be expected to exhibit similar mechanism of microstructure improvement upon annealing as clearly confirmed by TEM observation. Figure 3.3 shows the cross sectional bright field STEM images of $Mg_{0.95}Ti_{0.05}O$-based and $Mg_{0.9}Ti_{0.1}O$-based MTJs for the as-deposited and the post-annealed samples. In the as-deposited state (Figs. 3.3(a) and 3.3(c)), both compositions of MTO barrier exhibit out-of-plane texture of (001), while CoFeB layers are amorphous. After post-annealing process at 450°C, the initially amorphous CoFeB layers in both

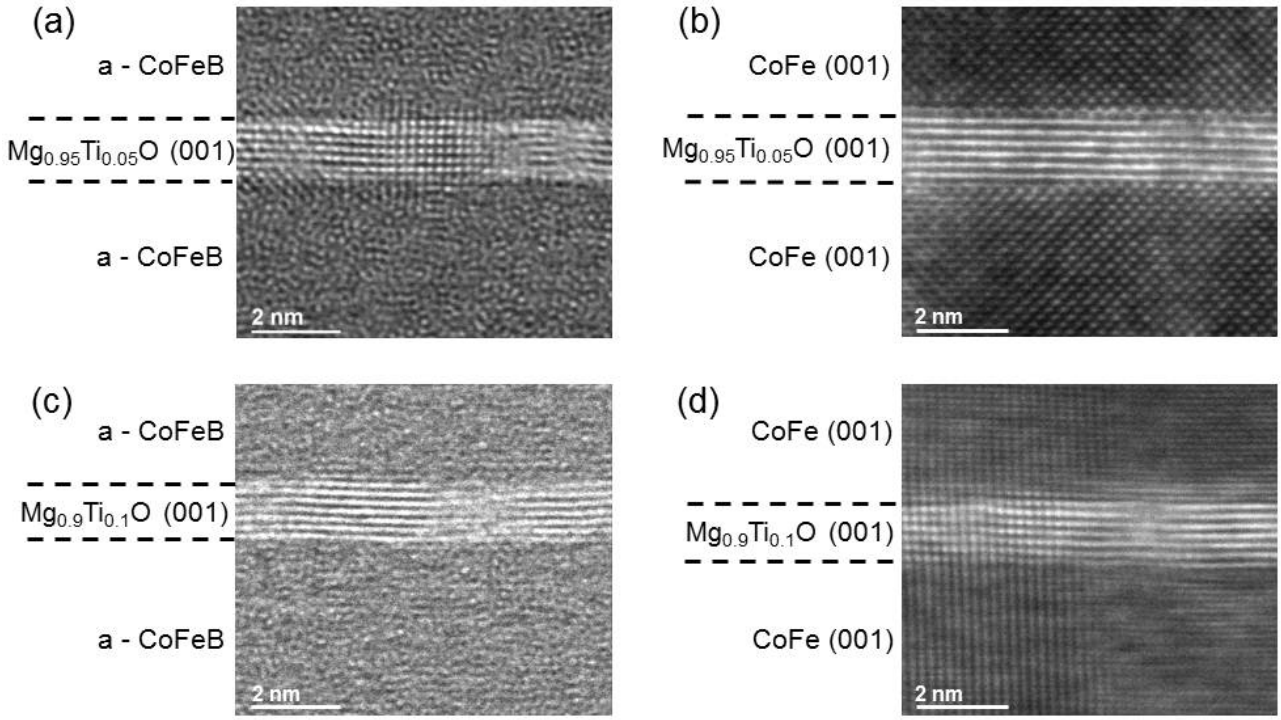

Figure 3.3: The cross-sectional BF-STEM image of (a) and (b) $Mg_{0.95}Ti_{0.05}O$-based and (c) and (d) $Mg_{0.9}Ti_{0.1}O$- based MTJs. (a) and (c) correspond to the as-deposited samples while (b) and (d) correspond to those post-annealed at 450°C.

samples can be seen to form crystalline CoFe. The grain-to-grain epitaxy with orientation relation of (001)[110]MTO//(001)[100]CoFe was confirmed for these two MTO compositions. The epitaxial relationship similar to that in CoFeB/MgO is held in CoFeB/MTO fulfilling the microstructure requirement of coherent tunneling and is possibly the origin of high TMR ratio.

Figures 3.4 (a)-(c) show the temperature dependence (10 K 275 K) of TMR ratio and RA in parallel and antiparallel states for devices post-annealed at 450°C. The measured devices were selected to have RA in the parallel state of around 600-800 $\Omega\mu m^2$. It can be clearly seen that TMR ratio monotonically decreases with increasing temperature for all barriers. The RA in the parallel state for each barrier is relatively constant within the range of measurement temperature. This trend has been widely observed in MTJs with crystalline barriers that exhibit symmetry filtering effect [13, 14, 83]. On the other hand, the RA in the antiparallel state exhibits strong temperature dependence which, consequently, dominantly dictates the observed change of TMR ratio at varying temperature. The normalized TMR ratio, which enables the comparison of temperature dependence of TMR ratio for MTJs with different absolute values of TMR ratio, is shown in Fig. 3.4(d) for each barrier. The degree of temperature dependence of TMR ratio can be seen to be lower with increasing Ti concentration. This trend is in contrast to MTJs with Mg-Zn-O barriers that shows stronger temperature dependence of TMR ratio with increasing Zn concentration [77]. The origin of the difference is still unclear and beyond the scope oh this chapter.

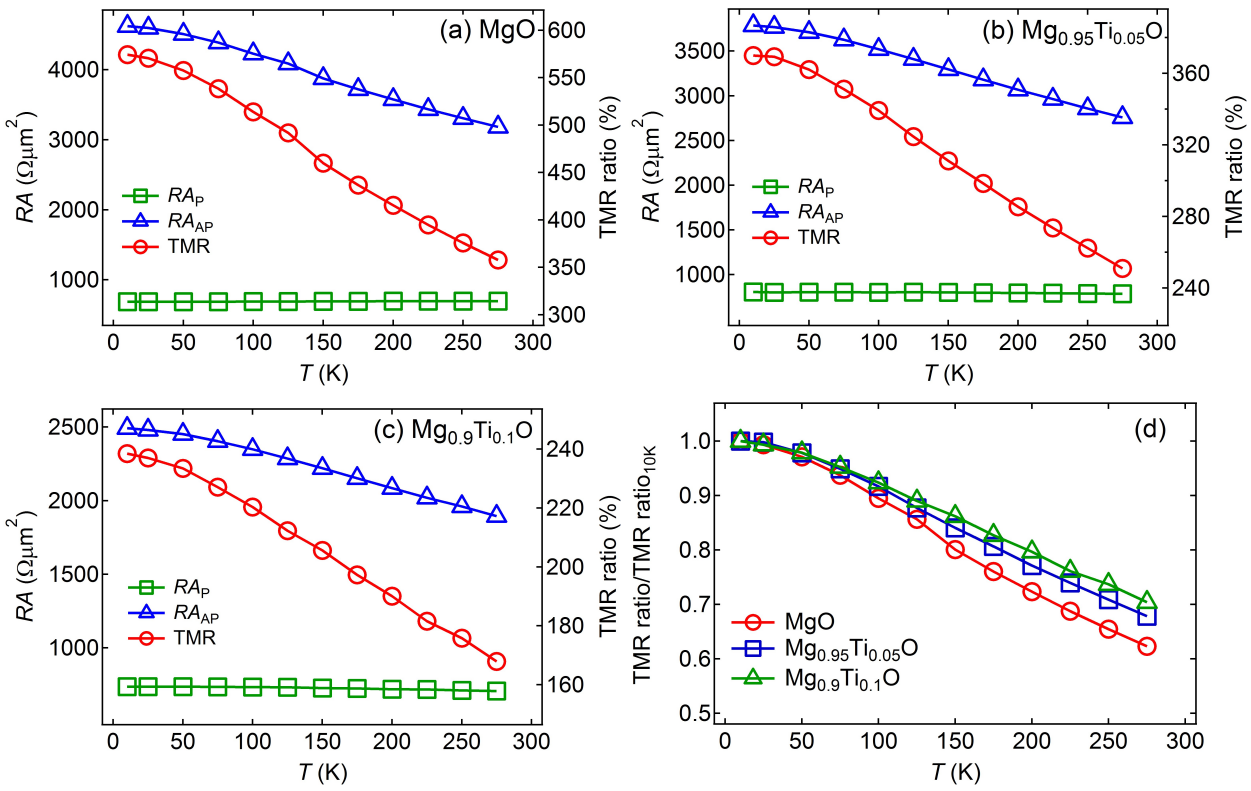

Figure 3.4: The *RA* measured at varying temperatures of 10 K 275 K for (a) MgO-based, (b) $Mg_{0.95}Ti_{0.05}O$-based and (c) $Mg_{0.9}Ti_{0.1}O$-based MTJs that were post-annealed at 450°C. (d) The normalized TMR ratio at varying temperatures for each barrier.

3.4 Benchmark with theoretical study

The high TMR ratio observed in the current MTO-based MTJs is also in contrast with the theoretical study reported in Ref [76]. The result of theoretical calculation showed that the TMR ratio of MTO-based MTJs rapidly decays with increasing Ti concentration and would vanish at x $\sim$ 0.2. The decrease in TMR ratio was attributed to the presence of diffusive hotspots in antiparallel state as Ti concentration increases [76]. Though the trend of decreasing TMR ratio with increasing Ti concentration observed in the current work can be qualitatively correlated with the explanation in Ref. [76], the marked difference on vanishing TMR ratio predicted in the latter is in question. The current experimental results can be a good model for further development of theoretical study on the spin-dependent tunneling of alloyed-MgO barriers.

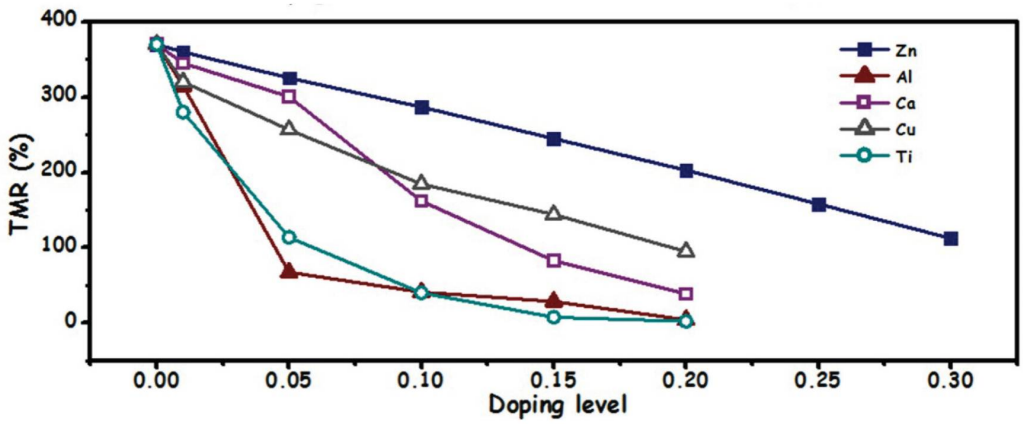

Figure 3.5: The calculated TMR ratio vs dopant level y for Fe/$Mg_{1-y}X_yO$/Fe MTJs with various dopant elements X(taken from [76])

3.5 Bias voltage dependence of tunneling conductance and TMR ratio

Figures 3.6 (a) and (b) show the differential conductance $G = dI/dV$ as a function of bias voltage at parallel and antiparallel states, respectively, for MTJs post-annealed at 450°C and measured at 275 K. Positive voltage corresponds to the tunneling electron flowing from bottom CoFeB to the top one. For each barrier, the shape of differential conductance is relatively symmetric suggesting the similar interface quality at top and bottom interfaces of barrier/ferromagnet. Within the range of bias voltage, the conductance of MgO-based MTJ at the parallel state just exhibits a slight change of less than 10% and shows pronounced dips at ±0.3 V as widely observed in previous reports [84–87]. On the other hand, both MTO-based MTJs exhibit more rapid conductance increase with increasing Ti concentration. The dips clearly observed in the MgO-based MTJ gradually disappear with increasing Ti concentration for MTO-based MTJs. The more rapid increase of differential conductance with increasing Ti concentration can be consistently seen in the antiparallel state. Based on the Brinkman model for the symmetric barrier height [59], the normalized differential conductance can be expressed as

$$G_{norm.} = 1 + \left(\frac{\pi^2 e^2}{h^2}\frac{m^* t^2}{\phi}\right) V^2$$

It was found that 0.2 nm of barrier thickness difference (Δt) does not significantly affect the trend of normalized differential conductance. Therefore, this rapid conductance change can be attributed to the lower barrier height with increasing Ti, supporting the analysis based on WKB model discussed above.

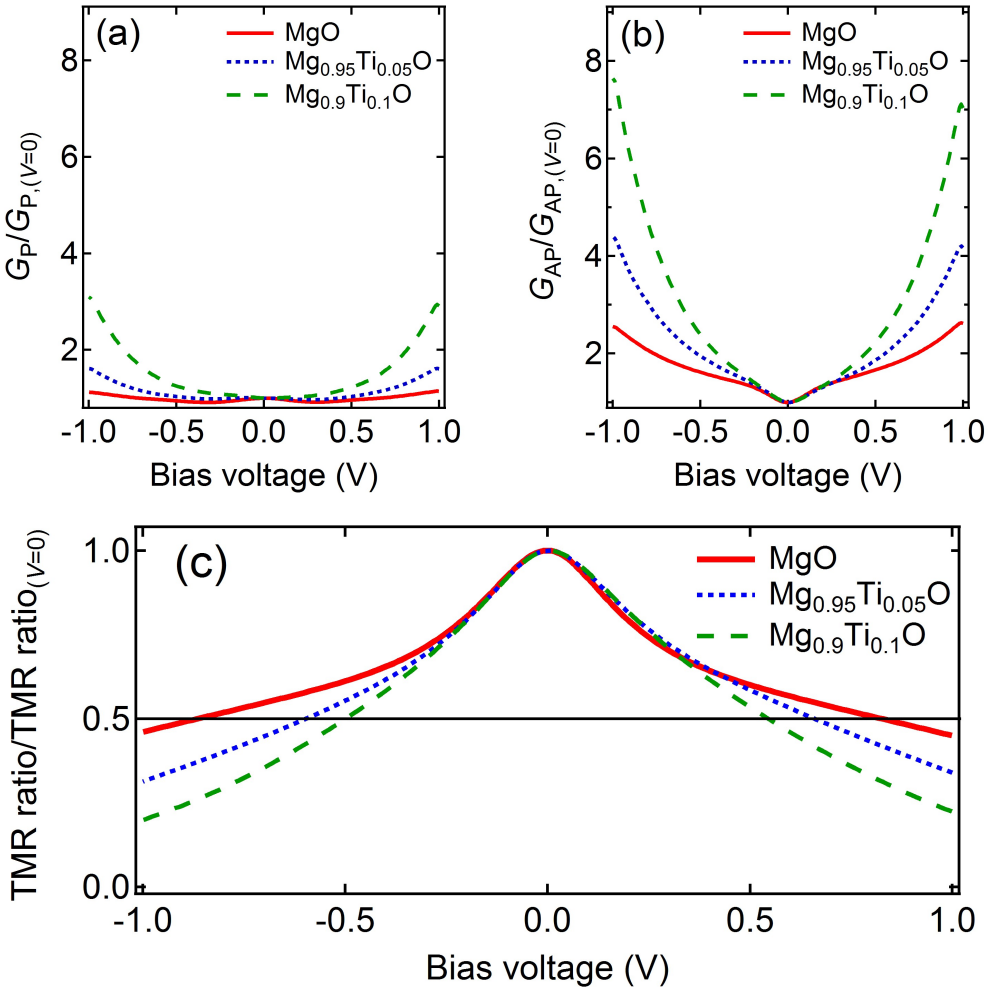

Figure 3.6: The differential conductance $G{=}dI/dV$ normalized to the value at $V = 0$ for (a) parallel and (b) anti-parallel states measured at 275 K. (c) The normalized TMR ratio of each barrier as a function of bias voltage measured at 275 K

Figure 3.6(c) shows the normalized TMR ratio as a function of bias voltage measured at 275 K. The V_{half}, the bias voltage at which TMR ratio reduce to half maximum, can be seen to decrease with increasing Ti concentration. This is in correlation with the rapid increase in the differential conductance observed in MTO-based MTJs having lower barrier height, hence suggesting that a dilemma arise if barriers with narrow band gap are used; the corresponding TMR ratio drastically decrease with bias voltage. Though the large V_{half} has been frequently regarded to indicate the high figure of merit of an MTJ for practical applications, it does not necessarily suggest that MTO-based MTJs have no potential for HDD read sensors as well as MRAM. In fact, the typical bias voltage in HDD sensor is around 100-200 mV [88], a voltage range at which the voltage dependence of TMR ratio in MTO-based MTJs is the same as that in MgO-based MTJs.

3.6 Summary

In summary, the preparation, spin-dependent tunneling transport, and microstructure of CoFeB/ $Mg_{1-x}Ti_xO$ MTJs was investigated. The $Mg_{1-x}Ti_xO$ barriers were found to have a rock-salt structure and grow with (001) texture on CoFeB electrodes. The high TMR ratio over 200% and 150% were observed for $Mg_{0.95}Ti_{0.05}O$-based and $Mg_{0.9}Ti_{0.1}O$-based MTJs respectively, at the optimum annealing temperature. This observation of high TMR ratio over 100% implies the presence of symmetry filtering even in the alloyed-MgO barriers. The $Mg_{1-x}Ti_xO$ barriers were clearly confirmed to have lower RA values compared to those of MgO ones for a given thickness, suggesting the intrinsically narrow band gap, hence lower barrier height, in the former case. The $Mg_{1-x}Ti_xO$-based MTJs exhibit higher TMR ratio than that of MgO-based one for RA lower than 5 $\Omega\mu m^2$as a consequence of thicker barriers and better wettability as discussed above. The promising applications of $Mg_{1-x}Ti_xO$ barriers for MTJs with low RA is successfully demonstrated.

Finally, the comment on the possibility of improving the TMR ratio in $Mg_{1-x}Ti_xO$-based MTJs is given. Previous studies have demonstrated that several techniques, such as Ta getter [89], Mg insertion [90], Co-Fe insertion [91], and *in situ* annealing of barriers [15], can be used to improve the microstructure of MgO-based MTJ leading to higher TMR ratio and even lower RA for a given barrier thickness. It can be anticipated that the same approaches mentioned above will work well, to a certain extent, even for $Mg_{1-x}Ti_xO$-based MTJs and further improve the TMR ratio from the current values reported here.

Chapter 4

Preparation of $Co_2Fe(Ga_{0.5}Ge_{0.5})$/Cu lateral spin valves by the top-down microfabrication process

4.1 Introduction

The manipulation of spin accumulation in a lateral spin valve (LSV) has received wide interest in the last decade due to its interesting flexibility in exploring spin-dependent transport phenomena of ferromagnet (FM) - nonmagnet (NM) systems [22, 26, 92–94]. In an LSV, the transport of a spin-polarized current as well as a pure spin current can be explored just by changing the measurement configurations on the same device. While the local configuration of an LSV is fundamentally analogous to the current-perpendicular-to-plane giant magnetoresistive (CPP-GMR) device that makes use of a spin-polarized current, the non-local configuration enables the generation and detection of a pure spin current without any charge current. The LSV has been envisaged to have the potential for narrow gap read sensor applications in the high density hard-disk drive (HDD) [23], because in an LSV the two FM layers are laterally separated, enabling a narrow read gap ($\leq$20 nm) for high density recording exceeding 2 Tbit/in^2 [18]. In addition, the free of charge feature of the spin current is expected to suppress the detrimental effect of joule heating which would be more pronounced as the dimension of the conventional read sensor scales down to achieve the high-resolution operation.

Since the spin accumulation inside a NM channel is generated by the spin-polarized current injected from a FM layer, the characteristic of FM/NM interfaces makes an important role in determining the efficiency of spin accumulation and spin current generation in an LSV. In general, the FM/NM interfaces in an LSV can be classified into three types, i.e., transparent (almost zero resistance), ohmic, and tunnelling contacts [26, 92, 93, 95]. Due to the demand for high data transfer rate in the high density HDD, low contact resistance fulfilled by either transparent or ohmic contact is considered to be suitable for read sensor applications. However, the low contact resistance LSV faces a serious problem on spin injection efficiency owing to the spin conductivity mismatch between metallic FM and NM channel materials [93, 96]. For transparent and ohmic contacts, this issue might be resolved by using half-metallic FM materials that enable highly efficient current conversion into fully spin-polarized current in a NM channel.

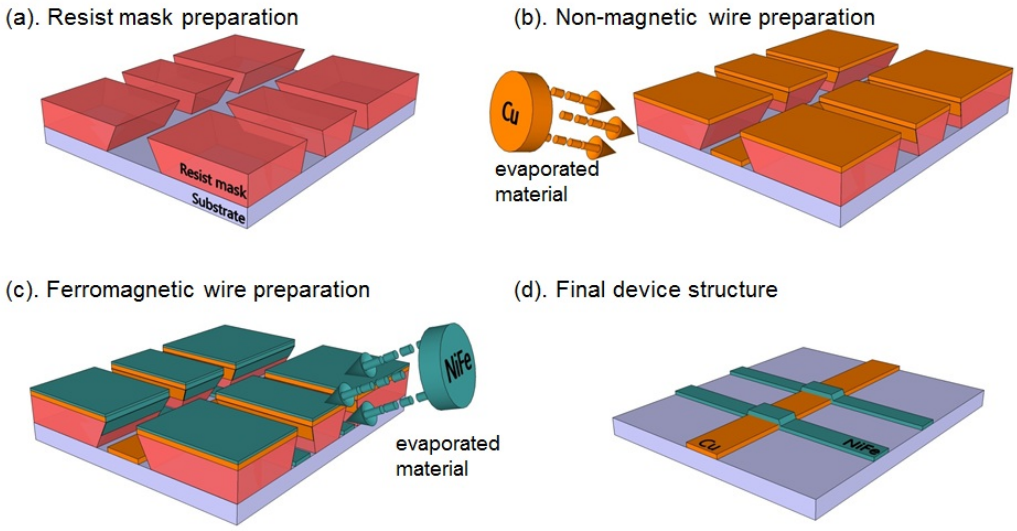

Figure 4.1: The typical procedure of shadow mask evaporation technique for preparing lateral spin valves

The microfabrication method of an LSV device is very crucial, since the realization of clean interfaces is highly required to investigate the intrinsic nature of the spin-dependent transport. The shadow mask evaporation technique has been widely utilized to prepare LSV devices with clean interfaces in the sub-micron scale dimension (see Fig. 4.1) [97–100]. Using the evaporation method, however, the choice of FM materials is limited to pure metals and some binary alloys. As such there have been only a few reports on LSVs utilizing highly spin-polarized FM materials such as Co-based Heusler alloys [22, 101–103], hampering to gain a comprehensive understanding of the potential of an LSV for read sensor applications.

Recently, the spin injection and detection in LSVs for the Co_2 $Fe(Ga_{0.5}Ge_{0.5})$/Cu system at room temperature [22] were demonstrated. The utilization of milling and lift-off processes has enabled the preparation of LSV devices from the $Co_2Fe(Ga_{0.5}Ge_{0.5})$ thin film with a specified composition exhibiting a high spin polarization. The spin signal, ΔR_S, of around 12.8 mΩ in the non-local configuration was obtained for the center-to-center ferromagnetic wires distance (d) of 350 nm, the largest ΔR_S for an all-metallic LSV at the time of the publication. In this chapter, the detail work on the microfabrication process to realize $Co_2Fe(Ga_{0.5}Ge_{0.5})$/Cu LSV devices with clean interfaces by a fully top-down process is described. The microfabrication route is compared to that in [22]. The detail microstructure characterization of the fabricated LSV devices was carried out by scanning transmission electron microscopy (STEM) to systematically clarify the suitability of the microfabrication process and its correlation with the spin-dependent transport.

4.2 Experiments

The multilayer stack of Cr(1 nm)/Ag(10 nm)/$Co_2Fe(Ga_{0.5}Ge_{0.5})$(20 nm)/Cu(20 nm)/cap layer was deposited on a single-crystalline MgO (001) substrate. The depositions of all layers were carried out using an ultrahigh vacuum magnetron sputtering machine at room temperature. The composition of the $Co_2Fe(Ga_{0.5}Ge_{0.5})$ layer was determined to be $Co_{49}Fe_{23}Ga_{14}Ge_{14}$ (at.%) using an inductively

coupled plasma analysis, which was slightly poor in Co and Fe and rich in Ga and Ge with respect to the stoichiometric $Co_2Fe(Ga_{0.5}Ge_{0.5})$. Right after the deposition of the $Co_2Fe(Ga_{0.5}Ge_{0.5})$ layer, the whole multilayer stack was annealed at 500°C in an ultrahigh vacuum chamber to promote the atomic order in the $Co_2Fe(Ga_{0.5}Ge_{0.5})$ layer. After cooling down to room temperature, the Cu (termed as pre-deposited Cu layer) and cap layers were deposited. The cap layer used in this work was Ru (5 nm) or MgO (2 nm), hence there will be two main sets of LSV devices distinguished by the cap layer used in the starting multilayer stack, the Ru-capped and MgO-capped ones. The multilayer stack was microfabricated into two 200 nm wide wires with d ranging from 350 to 1070 nm by the electron beam lithography (EBL) and the Argon-ion milling technique (Figs. 4.2(a)-(b)). Then, SiO_2 was sputter-deposited onto the milled area to ensure the insulation between two $Co_2Fe(Ga_{0.5}Ge_{0.5})$ wires (Fig. 4.2(d)). After lifting off the remaining resist mask (Fig. 4.2(d)), the sample was subsequently put into another Argon-ion milling machine to remove the cap and several nm thick Cu layers as shown in Fig. 4.2(e). Hereafter, this step is termed *in situ* milling to distinguish it from the other Argon-ion milling processes performed to prepare the LSV devices.

Here, the effect of *in situ* milling stop position on the ΔR_S of LSVs by varying the *in situ* milling time is investigated. The *in situ* milling time was determined so that the milling was terminated within the Cu layer. This milling stop position was intended to keep the atomic order of the $Co_2Fe(Ga_{0.5}Ge_{0.5})$ layer around the $Co_2Fe(Ga_{0.5}Ge_{0.5})$/Cu interface. After finishing the *in situ* milling process, the sample was then transferred into a vacuum-connected sputtering chamber to deposit 100 nm thick Cu layer (termed as post-deposited Cu layer) and 5 nm thick SiO_2 cap layer (Fig. 4.2(f)). As for the Ru-capped (MgO-capped) stack, the post-deposited Cu layer was prepared using the electron beam evaporation (sputtering) technique. Finally the Cu layer was patterned into 117 nm wide wire channel connecting the two $Co_2Fe(Ga_{0.5}Ge_{0.5})$ wires by using the electron beam lithography (EBL) and the Argon-ion milling technique (Figs. 4.2(g)-(h)). Note that in the previous report [22], the Cu wire was fabricated by means of the lift-off process which was preceded by milling the multilayer stack wires until the middle of the pre-deposited Cu layer in the presence of *polymethyl methacrylate* (PMMA) resist pattern. Then 100 nm thick Cu and SiO_2 cap layers were deposited in a separate evaporation chamber after the sample had been exposed to air to form a NM wire channel [22].

The final device structure as observed by the scanning electron microscopy (SEM) and the measurement schematic are shown in Fig. 4.3. A current was typically injected from the left $Co_2Fe(Ga_{0.5}Ge_{0.5})$ wire into the Cu wire by the reversed direct current (DC) technique with nominal current of around 100-500 μA. The electrochemical potential between the right $Co_2Fe(Ga_{0.5}Ge_{0.5})$ wire and the Cu wire was probed by a nanovoltmeter simultaneously. During the measurement an external magnetic field $\mu_0 H$ was applied parallel to the longitudinal direction of the $Co_2Fe(Ga_{0.5}Ge_{0.5})$ wires. Different switching fields of the $Co_2Fe(Ga_{0.5}Ge_{0.5})$ wires enabled the control of parallel and antiparallel states of the magnetizations. The actual dimension of the LSV devices was determined by scanning electron microscopy (SEM). The cross section observations of representative device structures were carried out by using the FEI Titan G2 80-200 scanning transmission electron microscopy (STEM) equipped with Cs-corrector for illumination and energy dispersive X-ray spectroscopy (EDS).

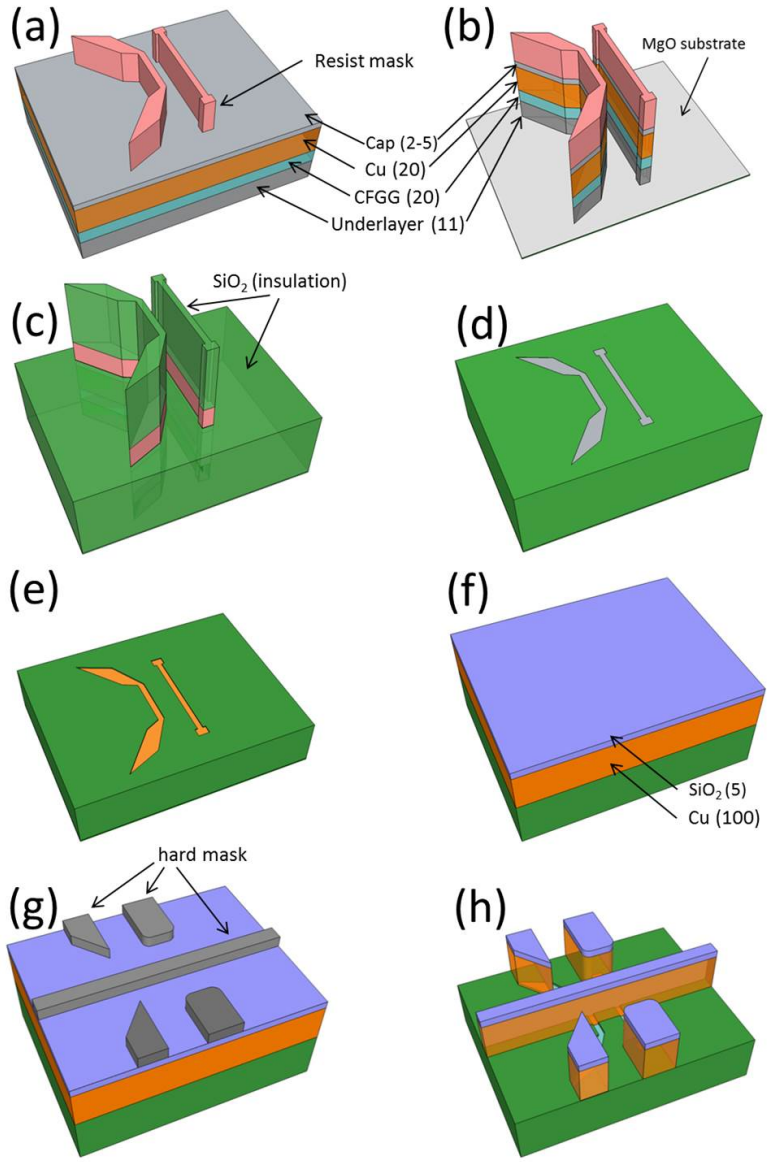

Figure 4.2: The microfabrication process of an LSV device. (a) The patterning of wires with various distances by using the EBL and negative resist mask. (b) The Argon-ion milling process to form wires. (c) The insulation of milled area by depositing SiO_2. (d) The lift-off of the remaining resist mask on wires. (e) The *in situ* milling process to remove the MgO cap layer and a several nm thick Cu layer. (f) The deposition of 100 nm thick Cu and 5 nm thick SiO_2 layers. (g) The patterning of a wire channel and electrode templates by using the EBL and hard mask. (g) The Argon-ion milling process to form the wire channel. Note that the pictures are not accurately to scale.

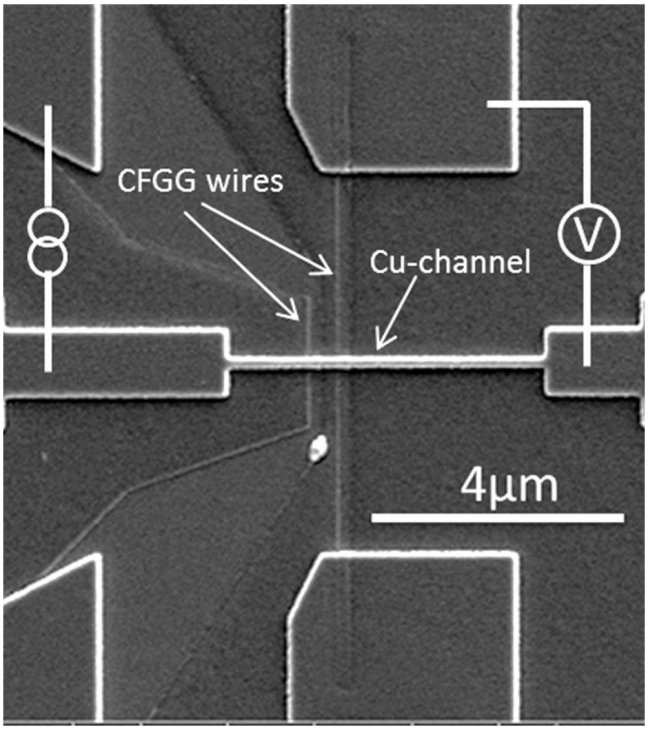

Figure 4.3: The SEM image of a representative LSV device covered by Ni-shunting layer and the schematic of non-local measurement.

4.3 Results

4.3.1 Ru-capped LSVs

The high-angle annular dark-field (HAADF)-STEM image of a cross-sectional sample prepared from a Ru-capped LSV device that was *in situ* milled for 210 s is shown in Fig. 4.4(a). The red arrows indicate two $Co_2Fe(Ga_{0.5}Ge_{0.5})$/Cu interfaces, both of which are sharp and clean. The nano beam electron diffraction (NBD) patterns taken from regions (i)-(vi) in Fig. 4.4(a) are shown in Fig. 4.4(b). The NBD pattern taken from the $Co_2Fe(Ga_{0.5}Ge_{0.5})$ layer (iii) shows the {001} spots in the [011] zone axis pattern, indicating the B2 order. The Cu layer (iv) pre-deposited on the $Co_2Fe(Ga_{0.5}Ge_{0.5})$ layer also shows the [001] zone axis pattern, indicating the orientation relationship of [011](001)$Co_2Fe(Ga_{0.5}Ge_{0.5})$//[001](020)Cu. The Cu layer post-deposited after the *in situ* milling process (v) grows epitaxially on the pre-deposited Cu layer (iv). However, the part of the Cu layer deposited on the SiO_2 is polycrystalline. This extended epitaxial-growth of the Cu layer on top of the $Co_2Fe(Ga_{0.5}Ge_{0.5})$ layer suggests the pre-deposited Cu layer surface was clean after the *in situ* milling process. The EDS maps taken from the right part of the LSV device (Fig. 4.4(c)) show no significant indication of interdiffusion with abrupt change in composition at the interface. The microstructure of the Ru-capped LSV device that was *in situ* milled for 300 s features the same characteristic as that milled for 210 s; hence it can be concluded that the LSV devices were consistently well fabricated for all ranges of *in situ* milling time.

The non-local resistance (V/I) as a function of magnetic field ($\mu_0 H$) of LSVs with d=500 nm is shown in Fig. 4.5(a) for each *in situ* milling time. Clear steps in non-local resistance, from positive (parallel state) to negative (antiparallel state) and vice versa, are observed, indicating the different switching fields of the $Co_2Fe(Ga_{0.5}Ge_{0.5})$ wires. Note that the ΔR_S values depend on *in situ* milling time, i.e., ΔR_S increases with increasing *in situ* milling time. This trend was consistently observed for all ranges of d as shown in Fig. 4.5(b). Since the *in situ* milling process involves the high energetic collision between the accelerated Argon beam and the target material, it is likely that cap-layer atoms may be implanted into the pre-deposited Cu layer during the ion milling process. If Ru atoms with significantly short spin diffusion length are implanted into the pre-deposited Cu layer [104, 105], a detrimental effect on spin transport is likely to occur since Ru atoms would rapidly relax the spin accumulation inside the Cu wire, hence suppressing the measured ΔR_S.

To clarify the possibility of implanted Ru atoms, the EDS mapping near the $Co_2Fe(Ga_{0.5}Ge_{0.5})$/Cu interface was performed. Figure 4.6(a) shows the HAADF-STEM image of the left part of the device shown in Fig. 4.4(a) and the red rectangle corresponds to the mapped region. Figure 4.6(b) showing the detail of EDS maps confirms the presence of implanted Ru atoms around the pre-deposited Cu/post-deposited Cu interface. The EDS mapping obtained from the sample *in situ* milled for 300 s did not give clear information on the presence of Ru atoms, suggesting the amount of implanted Ru atoms greatly reduces with increasing *in situ* milling time. Based on these EDS maps, the smaller ΔR_S obtained from the samples *in situ* milled for the shorter period of times is attributed to the implantation of Ru atoms into the Cu wire in the LSVs.

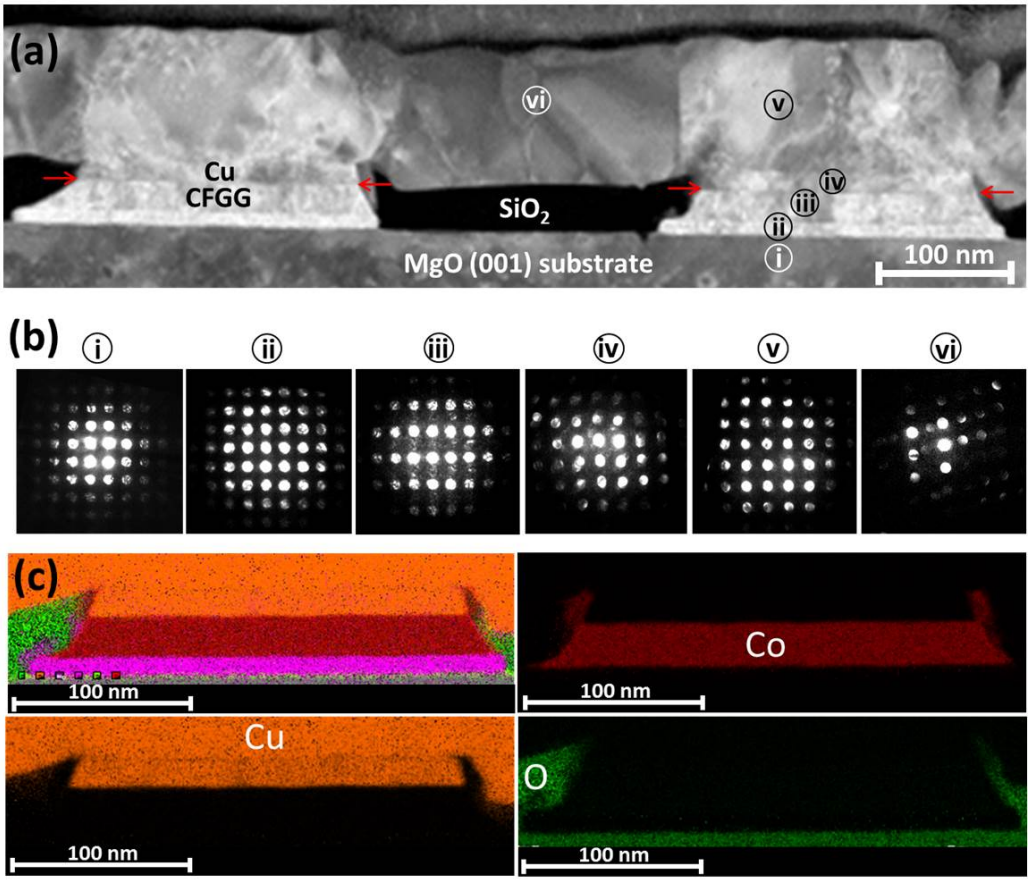

Figure 4.4: (a) The HAADF-STEM image of the Ru-capped LSV device cross section. Red arrowheads indicate the interfaces of $Co_2Fe(Ga_{0.5}Ge_{0.5})$/Cu. (b) The nano-beam electron diffraction patterns for each selected area as indicated in (a). (i), (ii), (iii), (iv), (v), and (vi) correspond to the MgO substrate, Ag underlayer, $Co_2Fe(Ga_{0.5}Ge_{0.5})$ layer (FM wire), pre-deposited Cu layer (NM wire), post-deposited Cu layer (NM wire) on Cu, and post-deposited Cu layer (NM wire) on SiO_2, respectively. The electron beam direction is parallel to (100) zone axis of the MgO substrate. (c) EDS maps of the right $Co_2Fe(Ga_{0.5}Ge_{0.5})$/Cu interface with each elemental map for Co (in red, the $Co_2Fe(Ga_{0.5}Ge_{0.5})$ representative), Cu (in orange, the wire channel representative), and O (in green, the MgO substrate and SiO_2 insulation representative).

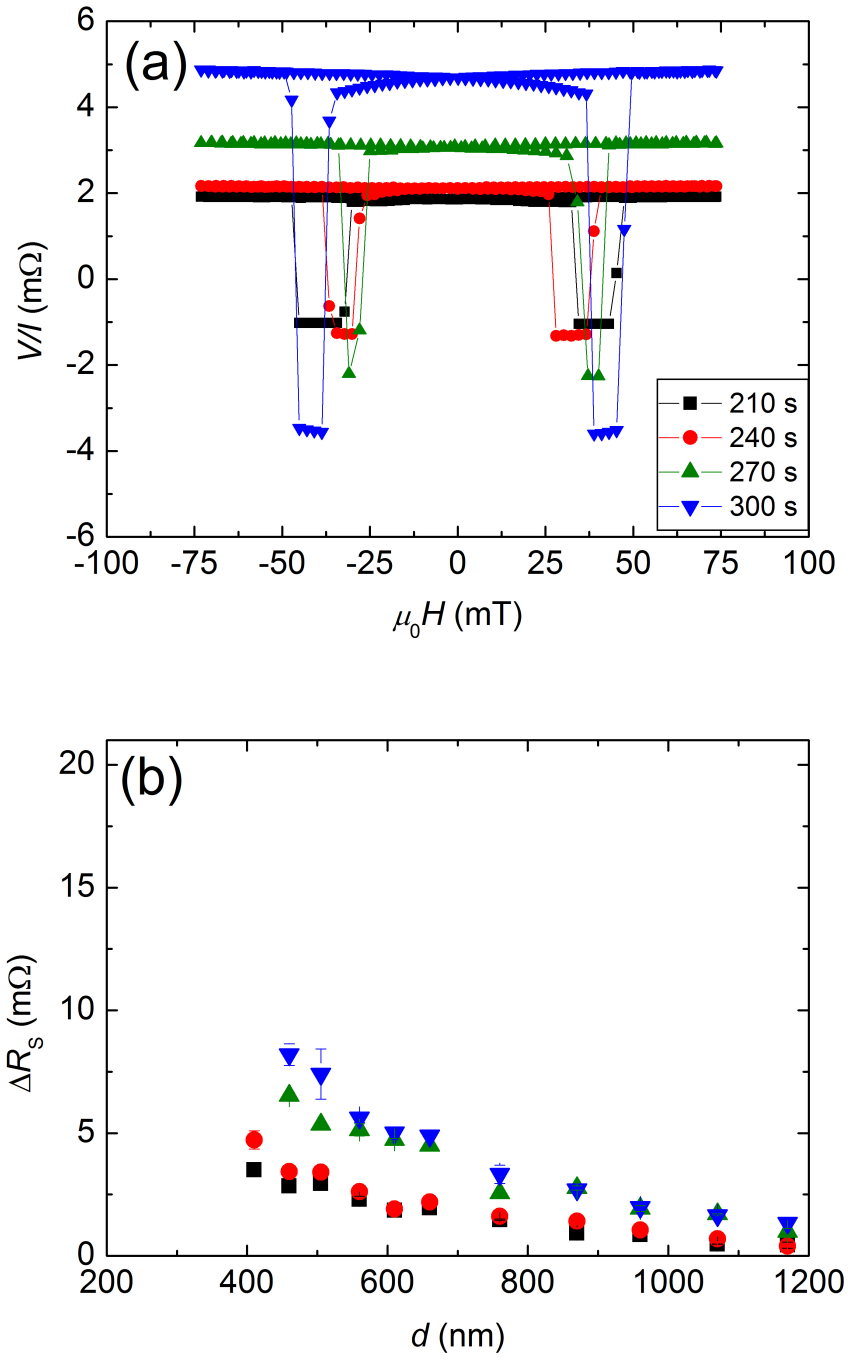

Figure 4.5: (a) The non-local resistance (V/I) as a function of magnetic field ($\mu_0 H$) for 210 s (black rectangles), 240 s (red circles), 270 s (green up-triangles) and 300 s (blue down-triangles) *in situ* milled Ru-capped LSVs with d of 500 nm. (b) The ΔR_S as a function of d for each *in situ* milling time (the legend is the same as that in (a)).

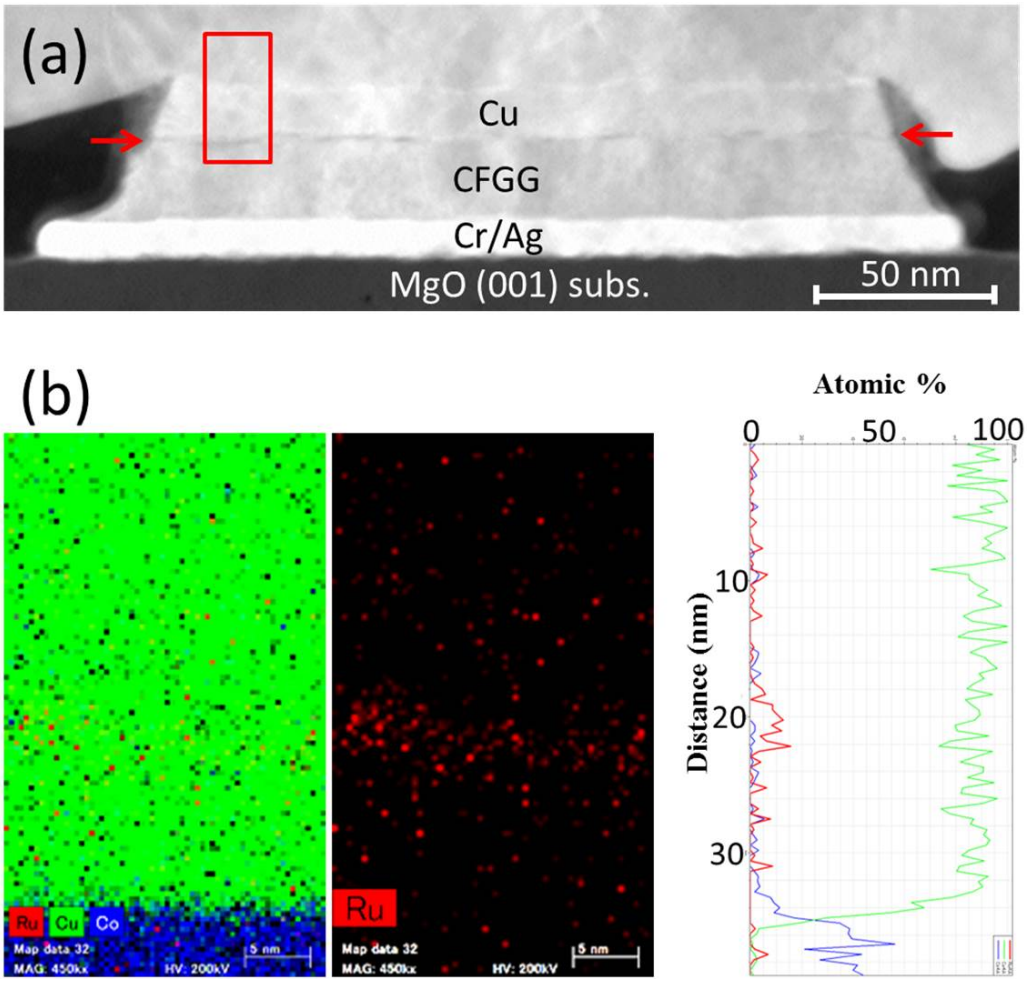

Figure 4.6: (a) The HAADF-STEM image of cross section for a Ru-capped LSV device *in situ* milled for 210 s. The red arrowheads indicate the interface of $Co_2Fe(Ga_{0.5}Ge_{0.5})$ wire (lower part) and Cu wire (upper part). The red rectangle corresponds to the selected area mapped by EDS which is shown in (c). (c) The EDS maps of Ru (in red), Cu (in green), and Co (in blue) atoms near the $Co_2Fe(Ga_{0.5}Ge_{0.5})$/Cu interface. The presence of little amount of Ru atoms is confirmed inside the Cu wire near to the $Co_2Fe(Ga_{0.5}Ge_{0.5})$/Cu interface.

4.3.2 MgO-capped LSVs

The HAADF-STEM image of a MgO-capped LSV device that was *in situ* milled for 180 s is shown in Fig. 4.7(a). The device has well-defined injector, detector, and channel parts. Figure 4.7(a) also shows clean and abrupt $Co_2Fe(Ga_{0.5}Ge_{0.5})$/Cu interfaces suggesting that the microfabrication process does not degrade the interface quality. The crystallographic orientation relationships of all the layers (Fig. 4.7(b)) are the same as those observed in the Ru-capped LSV device. The EDS maps show all the interfaces are chemically abrupt.

While there was almost no microstructure difference between the Ru-capped and MgO-capped LSV devices, the non-local resistance (V/I) change (Fig. 4.8(a)) and ΔR_{S} as functions of d (Fig. 4.8(b)) are almost the same regardless of the *in situ* milling times. In addition, the ΔR_S values of MgO-capped LSVs are larger compared to those for the Ru-capped ones for a given *d*. The maximum ΔR_{S} is 17.3 mΩ for d =350 nm, one of the largest value reported so far for an all-metallic LSV measured at room temperature.

As shown in Fig. 4.6, the Ru atoms were found to be implanted into the pre-deposited Cu layer during the *in situ* milling process. This is expected to give a detrimental effect to the spin accumulation of the Ru-capped LSVs processed with short milling times. On the other hand, MgO is expected to be ion-milled firmly due to a less wettability between oxides and noble metals, thereby not being easily implanted into the underlying Cu layer compared to Ru which forms the intermetallic bonding with Cu. Should Mg and O be implanted into the underlying Cu layer, the influence on the spin current transport will be negligible since Mg and O exhibits very small spin-orbit interaction. Although the microfabrication route reported in this work is highly flexible in selecting the combinations of FM/NM materials, a care must be taken for the selection of a cap layer such as Ru or Ta which exhibits short spin diffusion length due to significant spin-orbit interaction [104–106]. Therefore the choice of cap layer materials should be limited to those having small atomic mass or negligible spin-orbit interaction.

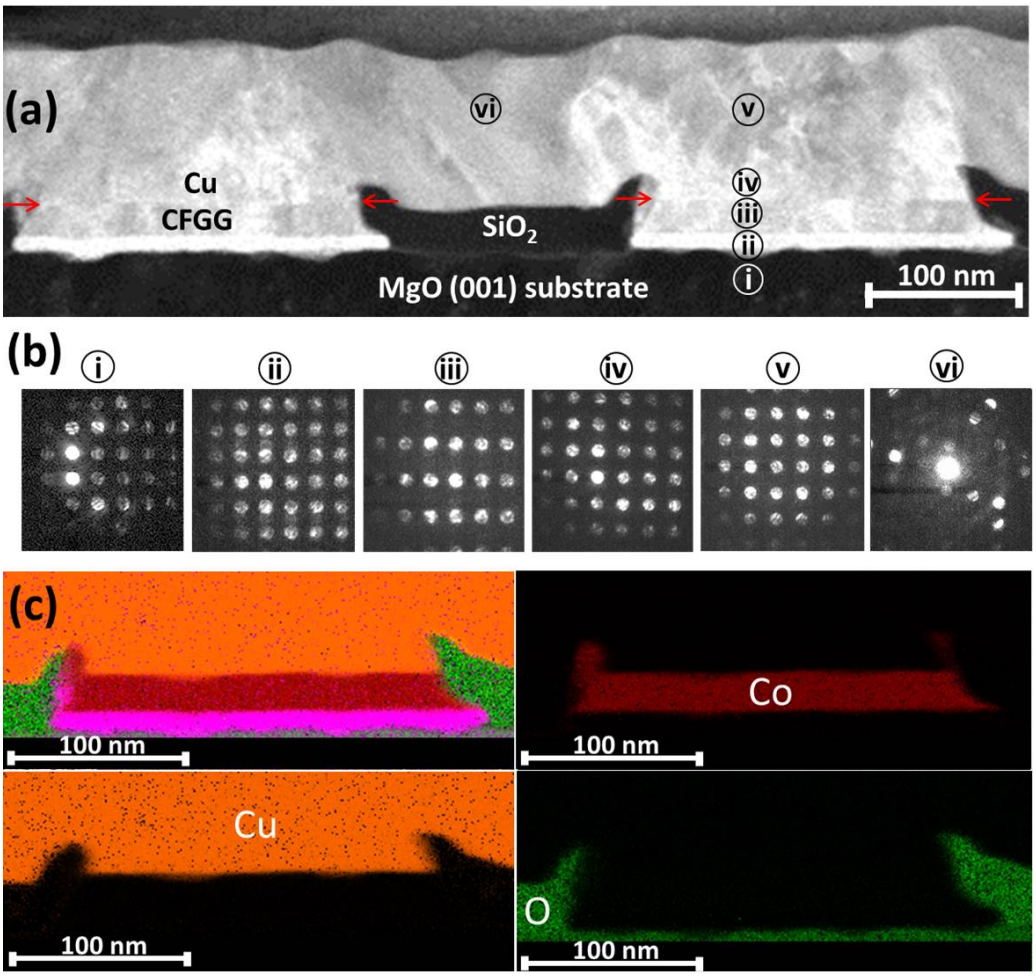

Figure 4.7: (a) The HAADF-STEM image of the MgO-capped LSV device cross section. Red arrowheads indicate the interfaces of $Co_2Fe(Ga_{0.5}Ge_{0.5})$/Cu. (b) The nano-beam electron diffraction patterns for each selected area as indicated in (a). (i), (ii), (iii), (iv), (v), and (vi) correspond to the MgO substrate, Ag underlayer, $Co_2Fe(Ga_{0.5}Ge_{0.5})$ layer (FM wire), pre-deposited Cu layer (NM wire), post-deposited Cu layer (NM wire) on Cu, and post-deposited Cu layer (NM wire) on SiO_2, respectively. The electron beam direction is parallel to (100) zone axis of the MgO substrate. (c) EDS maps of the right $Co_2Fe(Ga_{0.5}Ge_{0.5})$/Cu interface with each elemental map for Co (in red, the $Co_2Fe(Ga_{0.5}Ge_{0.5})$ representative), Cu (in orange, the wire channel representative), and O (in green, the MgO substrate and SiO_2 insulation representative).

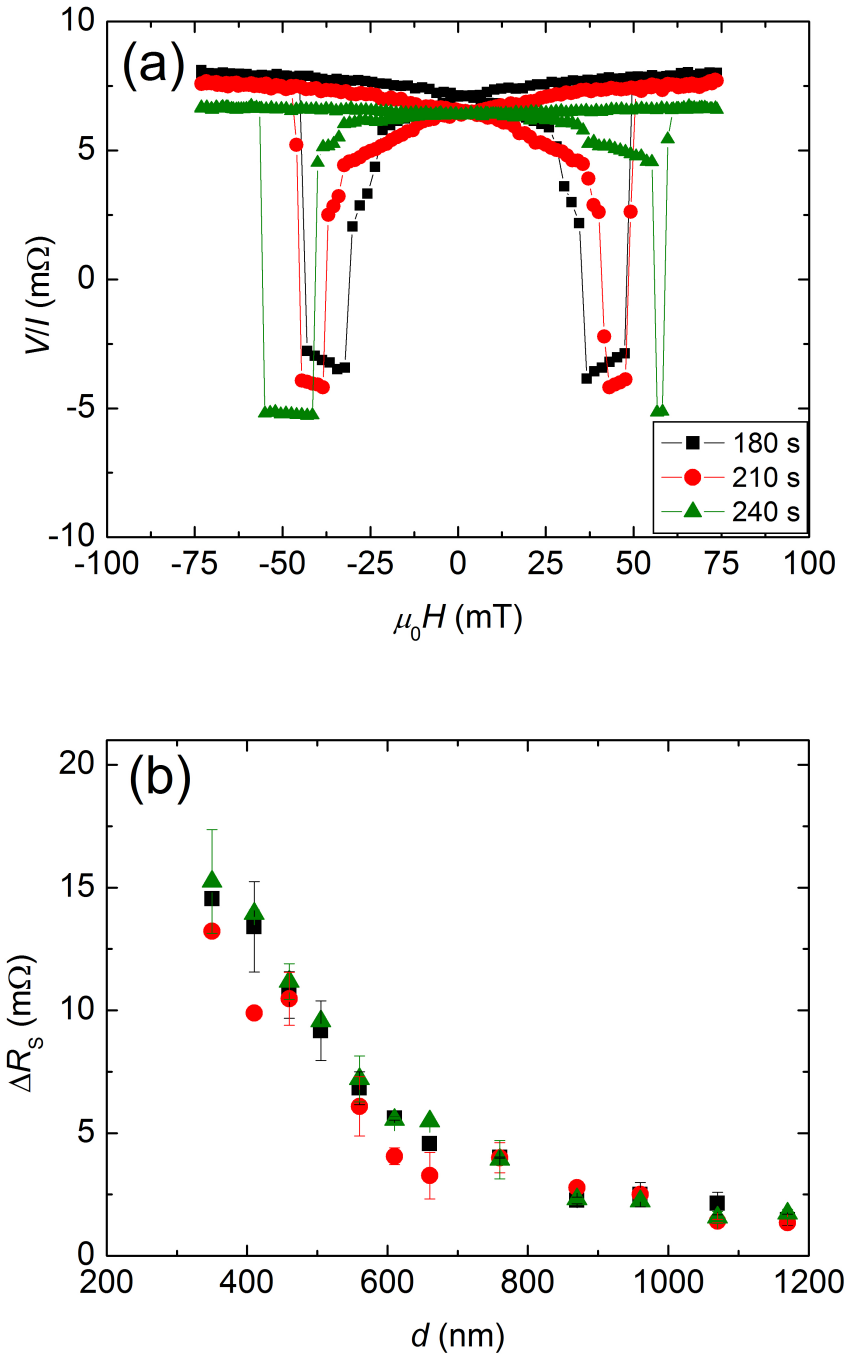

Figure 4.8: (a) The non-local resistance as a function of magnetic field ($\mu_0 H$) for 180 s (black rectangles), 210 s (red circles), and 240 s (green up-triangles) *in situ* milled MgO-cap LSVs with d of 450 nm. (b) The ΔR_S as a function of d for each *in situ* milling time (The legend is the same as that in (a)).

4.3.3 The effective contact resistance of FM/NM interfaces

Figure 4.9 shows the resistance-area product (RA) of FM/NM interfaces as a function of *in situ* milling time measured from Ru-capped and MgO-capped LSVs. The measured RA was found to be higher by 2-3 fold than that measured in CPP-GMR devices with $Co_2Fe(Ga_{0.5}Ge_{0.5})$/(Ag or Cu) interfaces. It should be noted that these are not necessarily the intrinsic RA of FM/NM interfaces since the contribution from $Co_2Fe(Ga_{0.5}Ge_{0.5})$ layer was inevitably measured. When the current is flowing through the FM wires, the current would be likely to flow in Ag underlayer which has much lower resistivity (one order of magnitude) compared to that of $Co_2Fe(Ga_{0.5}Ge_{0.5})$. A simple calculation considering the resistivity of $Co_2Fe(Ga_{0.5}Ge_{0.5})$ [107] and Ag confirms that more than 90% of electrons would flow through Ag under layer. As the current approaches the CFGG/Cu interface, it would be likely to flow in perpendicular direction to the interface, hence giving voltage drop accross the $Co_2Fe(Ga_{0.5}Ge_{0.5})$ layer and $Co_2Fe(Ga_{0.5}Ge_{0.5})$/Cu interface detected by the nanovoltmeter. In addition, the thin Ag layer is likely to give rise to current crowding effect at low resistive interfaces which possibly obscures the measurement of RA. Therefore, the measurement of intrinsic RA of FM/NM interfaces in the current device structure could not be performed accurately.

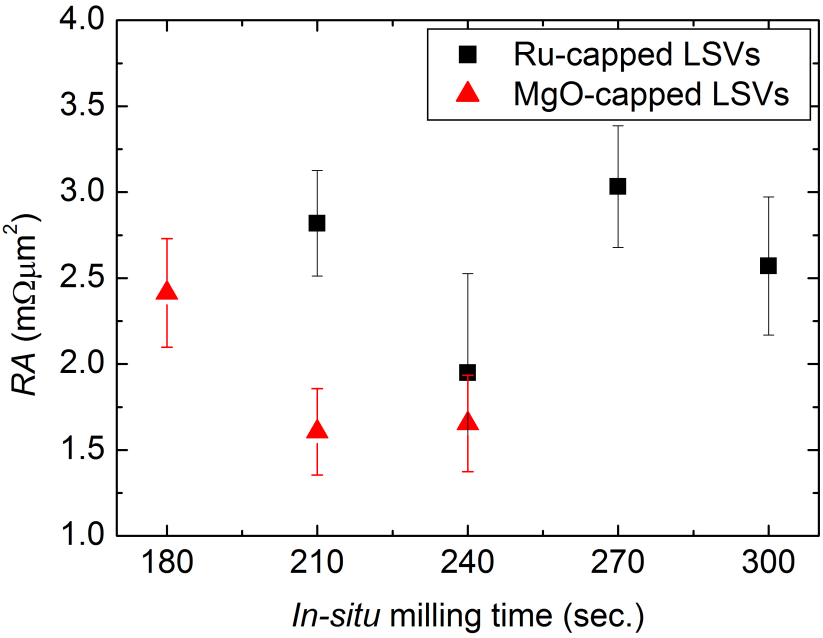

Figure 4.9: The effective RA of FM/NM interfaces

4.4 Discussion based on one-dimensional spin diffusional model

The fitting on ΔR_S as a function of d based on the one dimensional spin diffusion model is performed to quantitatively analyze the difference in ΔR_S for different process and *in situ* milling time [93]. As previously mentioned, the intrinsic RA of FM/NM interfaces cannot be accurately measured, hence hampering the use of general expression of Eq. 1.17. Nevertheless, the assumption of transparent interfaces, which consequently ignores interface spin polarization, is justified for the purpose of comparing the series of LSV devices in the present work. Please refer to the Appendix A for detail discussion on

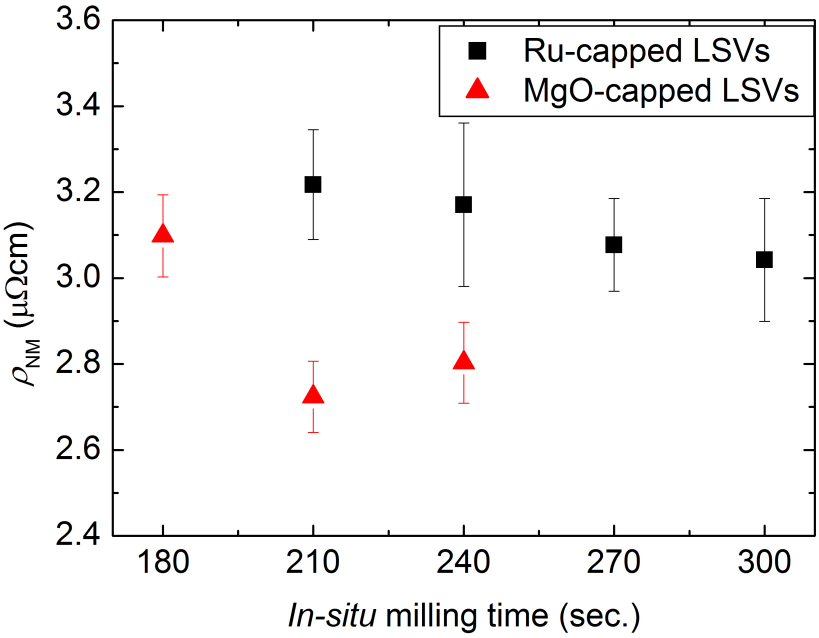

Figure 4.10: The ρ_{NM} of Cu wires.

fitting with and without the assumption of transparent interfaces. The simplified expression of one dimensional spin diffusion model for transparent assumption is given as

$$\Delta R_{\mathrm{S}} = 4R_{\mathrm{S}} \frac{\left(\frac{P_{\mathrm{FM}}}{1-P_{\mathrm{FM}}^2}\frac{R_{\mathrm{FM}}}{R_{\mathrm{NM}}}\right)^2 e^{\frac{-d}{\lambda_{\mathrm{NM}}}}}{\left(1+\frac{2}{1-P_{\mathrm{FM}}^2}\frac{R_{\mathrm{FM}}}{R_{\mathrm{NM}}}\right)^2 - e^{\frac{-2d}{\lambda_{\mathrm{NM}}}}} \tag{4.1}$$

where $R_{\mathrm{FM}} = \rho_{\mathrm{FM}}\lambda_{\mathrm{FM}}/A_{\mathrm{J}}$ and $R_{\mathrm{NM}} = \rho_{\mathrm{NM}}\lambda_{\mathrm{NM}}/\mathrm{A}_{\mathrm{NM}}$ are the spin resistance of FM and NM, respectively, with ρ, λ, and A correspond to resistivity, spin diffusion length, and effective cross section for spin current, respectively. The P_{FM} is the bulk spin polarizations. Figure 4.10 shows the resistivity of Cu wires for Ru-capped and MgO-capped LSVs with different *in situ* milling time, which are quite similar one with another. For this fitting it is assumed that the $Co_2Fe(Ga_{0.5}Ge_{0.5})$ has the same λ_{FM} and ρ_{NM} as those deduced from the CPP-GMR devices annealed at 500°C [107], i.e., λ_{FM}=2.1 nm, and ρ_{FM}=65 $\mu\Omega$cm. The preparation condition for $Co_2Fe(Ga_{0.5}Ge_{0.5})$ layer in the present LSVs is the same as that in ref [107] hence it is plausible to treat the $Co_2Fe(Ga_{0.5}Ge_{0.5})$ quality to be the same. Using these parameters the fitting is performed to deduce P_{FM} and λ_{NM}.

Figure 4.11(a) shows P_{FM} as function of *in situ* milling time for both Ru-capped and MgO-capped LSVs. As for the Ru-capped LSVs, P_{FM} changes from negative to positive with increasing *in situ* milling time, implying the implanted Ru atoms significantly influence the spin-dependent transport. On the other hand, the P_{FM} values of the MgO-capped LSVs, within the range of 0.79-0.81, are relatively similar one with another regardless of the *in situ* milling times and are much larger than those of Ru-capped ones, suggesting the reproducibility of the interface quality.

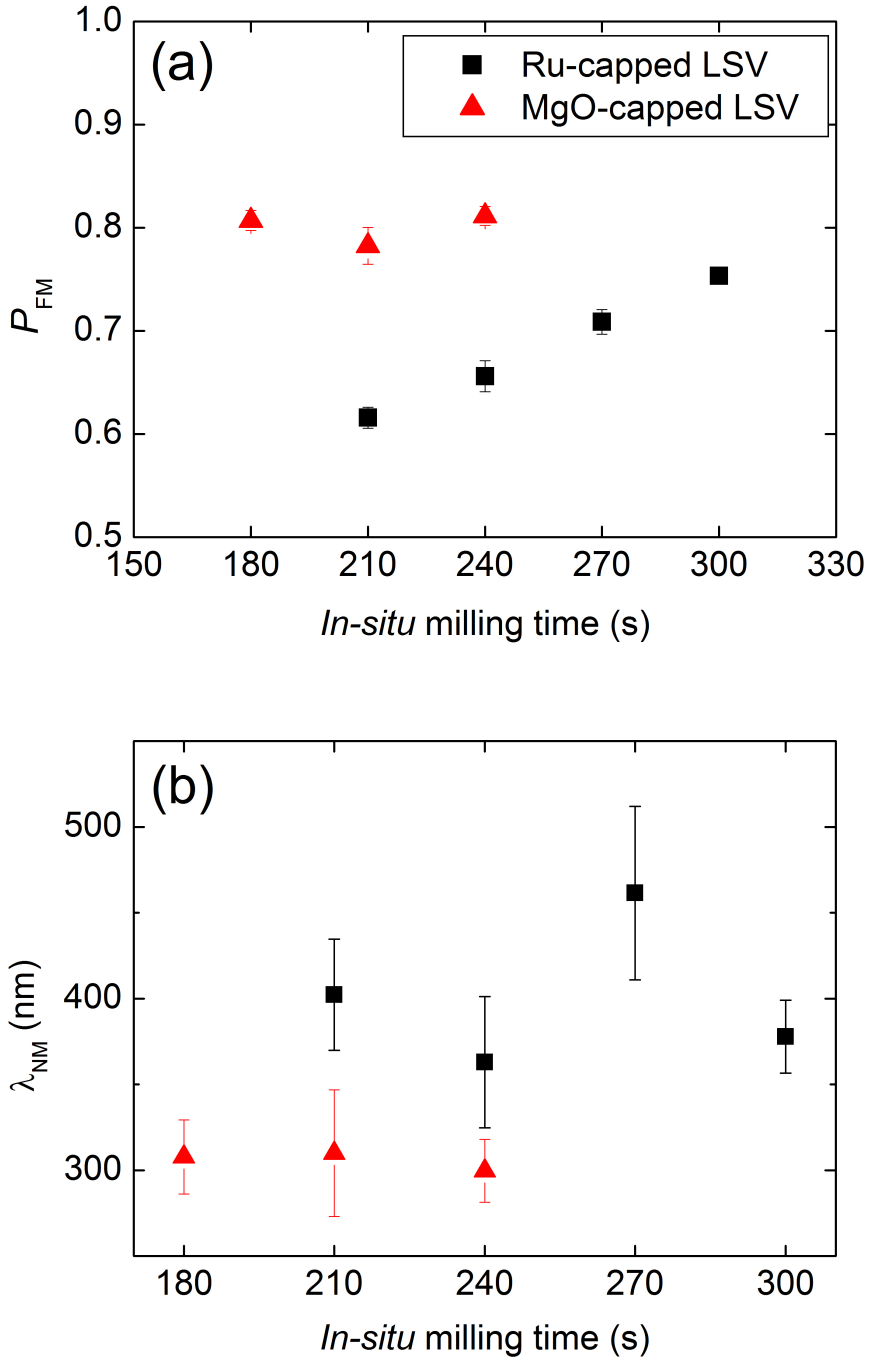

Figure 4.11: The deduced P_{FM} and (b) λ_{NM} as a function of *in situ* milling time for Ru-capped (black rectangles) and MgO-capped (red triangles) LSVs. The legend is the same for both figures.

Figure 4.11(b) shows that the λ_{NM} of Ru-capped LSVs, of around 363-464 nm, is significantly longer by 60-160 nm than that of the MgO-capped LSVs possibly due to the difference in the post-deposited Cu layer deposition method. Despite the longer λ_{NM} for the Ru-capped LSVs compared to those of the MgO-capped LSVs (Fig. 8(b)), the contribution of larger P_{FM} for the MgO-capped LSVs is considered to be more dominant to the larger ΔR_S, since the λ_{NM} itself mainly dictates the decay rate of ΔR_S with increasing *d*. Therefore, the realization of clean FM/NM interfaces in LSVs plays a crucial role in affecting the effective spin polarization which significantly contributes to the magnitude of ΔR_S.

The comparison between the present LSVs with those previously reported on the same $Co_2Fe(Ga_{0.5}Ge_{0.5})$/Cu system but with a different microfabrication route [22] is performed. For this purpose, the notation of $\Delta R_S A_G$ from ref. [102] is adapted, where A_G corresponds to $(A_{J,1}A_{J,2}/A_{NM})$, to compare non-local spin signal magnitude from different sets of LSVs with significantly different dimension. It is noted that including A_G essentially does not change Eq. 4.1 since a constant is just multiplied to both sides of this equation. The data of LSVs in ref. [22] is fitted by assuming the same parameters of $Co_2Fe(Ga_{0.5}Ge_{0.5})$ layer as used in the present LSVs and used other parameters as stated in the reference.

4.5 Process dependence : *in situ* milling and *ex situ* milling

Figure 4.12 shows $\Delta R_S A_G$ as a function of d as well as fitted curves for the present LSVs (the representatives of Ru-capped and MgO-capped ones) and those in ref. [22]. The $\Delta R_S A_G$ of LSVs in ref. [22] is smaller than that of the 300 s milled Ru-capped LSVs (the highest for this set of devices) and 240 s milled MgO-capped LSVs. On the other hand, the $\Delta R_S A_G$ of 210 s Ru-capped LSVs (the lowest for this set of devices) is clearly seen to be much smaller than the other sets of devices, because of the presence of implanted Ru atoms in the pre-deposited Cu layer. In fact, the P_{FM} of LSVs in ref. [22] was deduced to be around 0.74±0.004, slightly smaller than that of 300 s Ru-capped LSVs, which follows the trend of $\Delta R_S A_G$. Therefore, the deduced P_{FM} of each set of LSVs directly correlates with the observed trend of $\Delta R_S A_G$ despite the difference in λ_{NM} among those devices.

The significant difference in $\Delta R_S A_G$ as well as P_{FM} of LSVs in ref. [22] compared to that of MgO-capped ones reported here is somewhat intriguing since in ref. [22] SiO_2 was used as a cap layer and expected to perform as reliable as the MgO cap layer in the present report. Figures 4.13(a) and (b)-(f) show the cross-sectional bright-field STEM image and EDS maps, respectively, of a representative LSV device in ref. [22]. The STEM image shows the interface between the pre-deposited Cu layer and the post-deposited Cu wire is preferentially milled with a narrow metallic path of about 5 nm. The EDS maps shows the presence of a kind of oxides in this region which originates from a consequence of breaking the vacuum before deposition of Cu wire and/or re-deposited PMMA resist during the milling process. The Si-elemental map in Fig. 4.13(f) confirmed that this oxide cannot be attributed to SiO_2, the most possible source of oxide around the Cu/Cu interface since it was used as cap and insulation layers. Nevertheless, the presence of the thin oxide layer at the Cu/Cu interface was likely to be the reason the lower $\Delta R_S A_G$ compared to the MgO-capped ones.

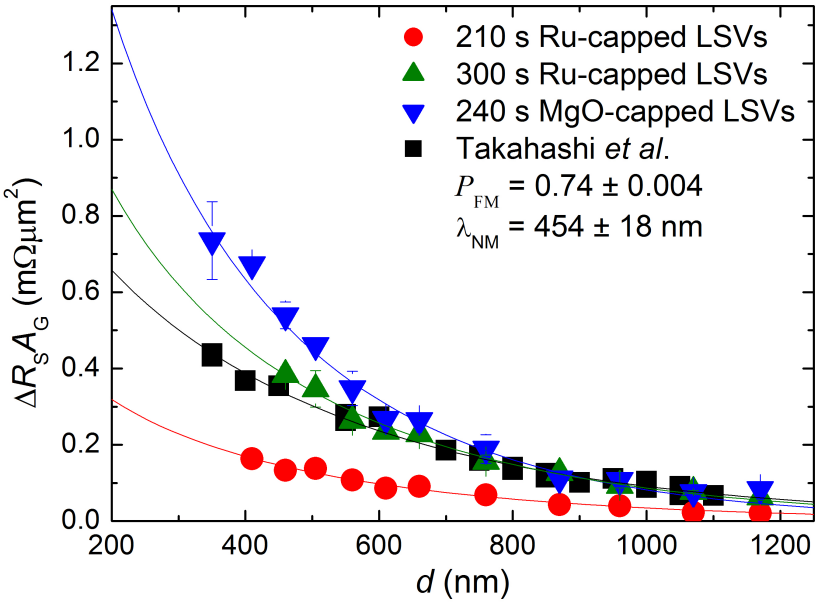

Figure 4.12: The $\Delta R_S A_G$ as a function of d for LSVs in Ref. [22] (black rectangles) and those of representatives of Ru-capped (210 s in red circles and 300 s in green up-triangles) as well as MgO-capped LSVs (240 s in blue down-triangles). The solid lines correspond to the best fits based on Eq. (1). The deduced P_{FM} and λ_{NM} for LSVs in Ref. [22] is shown along with the legend.

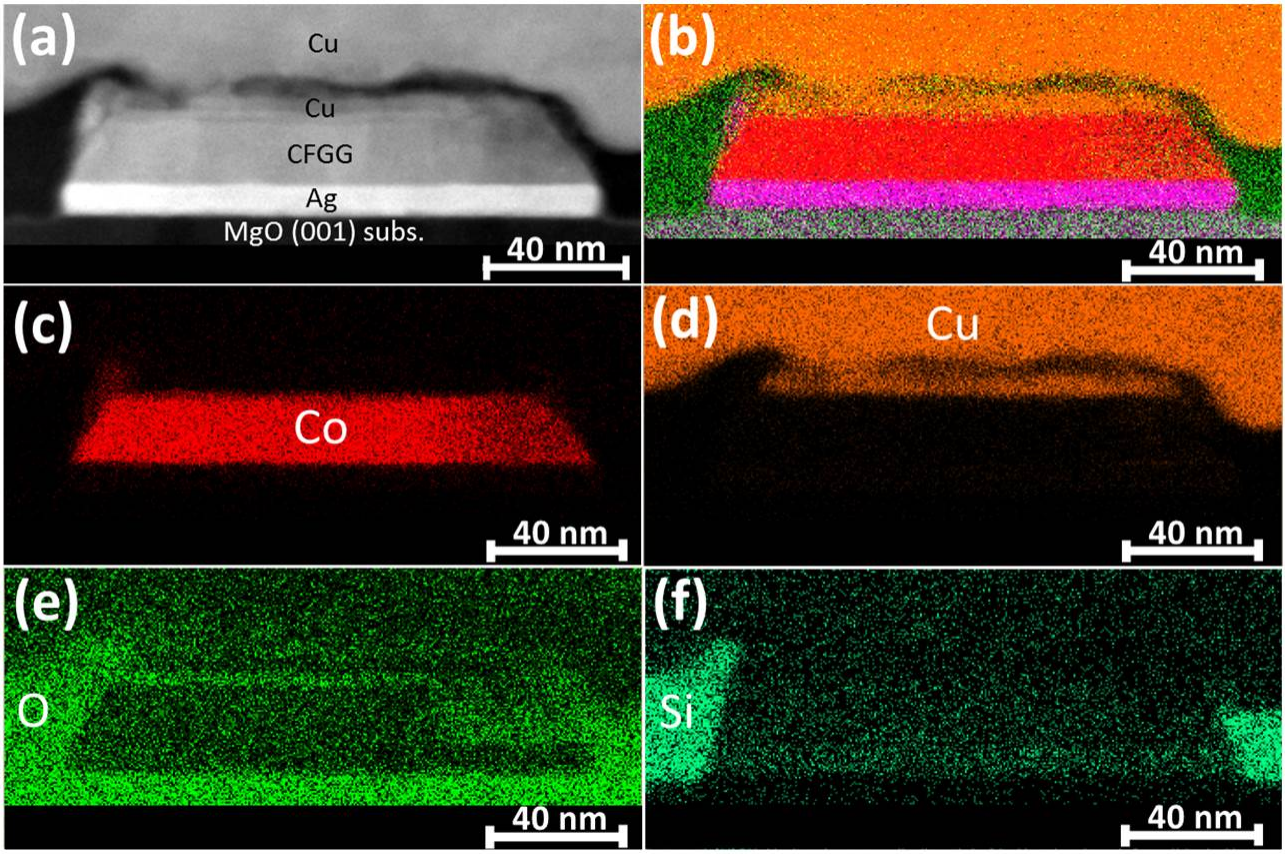

Figure 4.13: (a) The HAADF-STEM image of a $Co_2Fe(Ga_{0.5}Ge_{0.5})$/Cu interface of a representative LSV device in ref. citeTaka2012. (b) The corresponding EDS maps and each elemental map for (c) Co (in red, the $Co_2Fe(Ga_{0.5}Ge_{0.5})$ representative), (d) Cu (in orange, the wire channel representative), (e) O (in green, the MgO substrate and SiO_2 insulation representative), and (f) Si (in light green, the SiO_2 insulation representative).

4.6 Summary

An alternative route for the realization of $Co_2Fe(Ga_{0.5}Ge_{0.5})$/Cu LSVs by the top-down microfabrication process was successfully demonstrated. The dependence of the microfabrication reliability on the choice of cap layer materials was systematically investigated, underlining a challenge in realizing clean FM/NM interfaces in an LSV by the top-down process. A very large ΔR_S of 17.3 mΩ was obtained at room temperature suggesting the high effective spin polarization of the bulk $Co_2Fe(Ga_{0.5}Ge_{0.5})$ as well as the importance of clean FM/NM interfaces to achieve efficient spin injection into a NM channel.

Chapter 5

Temperature dependence of magneto-transport properties in $Co_2Fe(Ga_{0.5}Ge_{0.5})$/Cu lateral spin valves

5.1 Introduction

There have been only a few reports on the utilization of Co-based Heusler alloys as FM wires in all-metallic lateral spin valves (LSVs) with detail temperature dependence measurement of spin signals [101–103]. In 2011, Bridoux *et al.* reported the observation of enhanced spin signal of around 12 mΩ at 77 K for LSVs using polycrystalline Co_2FeAl and Al channels [101]. In this first report of Heusler-alloy-based LSVs, the authors attributed the highly spin polarized and highly resistive Co_2FeAl as the main origin of enhanced spin signals in their experiment. In 2012, Oki *et al.* demonstrated a spin signal of 7.5 mΩ at 77 K in CoFeAl/Cu LSVs [103]. They argued that the large spin signal observed in their experiment can be mainly attributed to the high spin polarization of low-resistive CoFeAl film, emphasizing the contribution of highly B2 ordered CoFeAl films [103]. Later, Kimura *et al.* reported the use of epitaxially grown Co_2FeSi films as FM wires combined with a Cu channel and observed spin signals over 10 mΩ at temperature below 70 K, which is also attributed to the high spin polarization of Co_2FeSi film [102]. Apart from that, the result described in the previous chapter indeed show high spin signals over 10 mΩ even at room temperature in $Co_2Fe(Ga_{0.5}Ge_{0.5})$/Cu LSVs. This result has put forward the possibility of using highly spin polarized Heusler alloys for spintronics applications such as read sensors of hard-disk drives, which has been supported by the recent demonstration of $Co_2(Fe_{0.4}Mn_{0.6})Si$/Cu LSVs at room temperature for much smaller dimensions with a junction area of 50 nm^2 [108]. In the view of applications, spin signals at room temperature are important; nevertheless, the report on the temperature dependence of spin signals in LSVs utilizing $Co_2Fe(Ga_{0.5}Ge_{0.5})$ as well as $Co_2(Fe_{0.4}Mn_{0.6})Si$ can give insights into the true nature of LSVs with half-metallic FMs.

In this chapter, the work on the temperature dependence of magneto-transport properties in $Co_2Fe(Ga_{0.5}Ge_{0.5})$/Cu LSVs is described. Very large non-local spin signals of 13 mΩ and 54 mΩ were

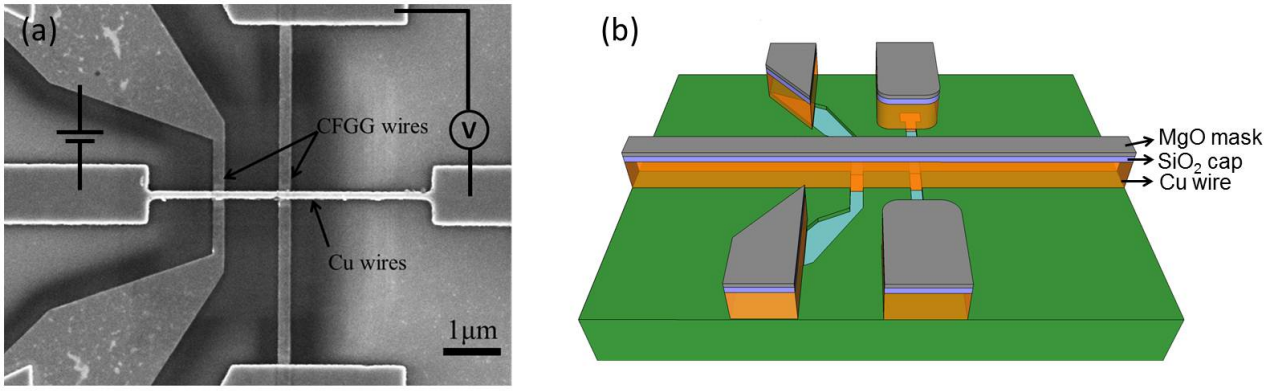

Figure 5.1: (a) The top view of a final device observed by a scanning electron microscope (SEM). The non-local configuration of transport measurement is schematically pictured. (b) The schematic illustration of side view of a final device. The top surface of Cu wires is capped by SiO2 layer and the remaining MgO mask

measured at 290 K (room temperature) and 5 K respectively for a device with the center-to-center FM wire distance of d=400 nm. The fitting of the d dependence of the spin signals to the one-dimensional spin diffusion model [93] confirms that the effective spin polarization of $Co_2Fe(Ga_{0.5}Ge_{0.5})$ is significantly higher than that of other Heusler alloys incorporated in LSVs [101–103], at both room temperature and low temperature. The non-local spin signals are found to exhibit a non-monotonic trend with decreasing temperature at the low temperature range below 50 K. In order to clarify the possible origin of the observed non-monotonic trend in non-local spin signals, the temperature dependence of the effective spin polarization of $Co_2Fe(Ga_{0.5}Ge_{0.5})$ and the spin diffusion length of Cu is investigated.

5.2 Experiment

The multilayer stack of Cr(3 nm)/Ag(10 nm)/ $Co_2Fe(Ga_{0.5}Ge_{0.5})$ (20 nm)/Cu(10 nm)/SiO_2(2 nm) was deposited on a single-crystalline MgO (001) substrate by using an ultrahigh vacuum magnetron sputtering machine. The deposition of each layer was carried out at room temperature. To induce the B2 chemical order in the $Co_2Fe(Ga_{0.5}Ge_{0.5})$, the multilayer stack was annealed at 500°C in an ultrahigh vacuum chamber right after the deposition of 20 nm thick $Co_2Fe(Ga_{0.5}Ge_{0.5})$ layer. The top-down microfabrication process, thoroughly described in the previous chapter, was performed to prepare LSV devices with submicron scale dimensions (Fig. 5.1) as reported in detail elsewhere [109]. The typical $Co_2Fe(Ga_{0.5}Ge_{0.5})$ wires width w_{FM} was around 190 nm with the d ranging from 400 to 800 nm, while the Cu wire thickness t_{NM} was around 100 nm with wire width w_{NM} of 115 nm. The surface of Cu wires was capped with SiO_2 layer and the remaining MgO mask, leaving the sidewall of wires to be exposed to the ambient atmosphere after device fabrication (Fig. 5.1(b)). The electrical measurement was performed in a non-local configuration with DC reversal method (Fig. 5.1(a)) at varying temperatures from 4 K to 290 K. During the measurement, the external magnetic field was applied parallel to the easy axis of $Co_2Fe(Ga_{0.5}Ge_{0.5})$ wires to obtain clear switching between parallel and anti-parallel states. The difference of measured voltage at detector part between parallel and anti-parallel states was normalized to the injected current and was defined as a non-local spin signal ΔR_S.

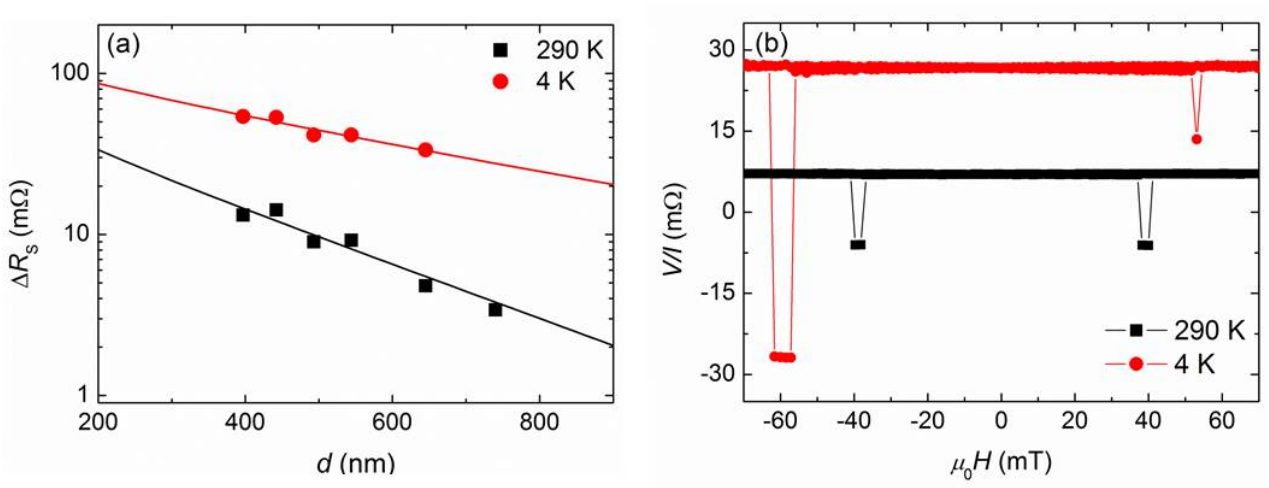

Figure 5.2: (a) The non-local spin signals for various d as measured at 290 K and 4 K. The red and black lines correspond to the fit based on the one-dimensional spin diffusion model. (b) The non-local resistance change for an LSV device with d of 400 nm measured at 290 K and 4 K.

5.3 The magneto-transport properties at 4 K and 290 K

Figure 5.2(a) shows the non-local spin signals of LSV devices measured at 290 K and 4 K for various *d*. For all range of d, non-local spin signals increase markedly by a factor of 4-5 from 290 K to 4 K. The non-local spin signal for d=400 nm reaches 13 mΩ and 54 mΩ at 290 K and 4 K, respectively (Fig. 5.2(b)). This large non-local spin signal, especially at low temperature, is among the largest for all-metallic LSVs with sub-micron size dimensions (w_{FM}, w_{NM}within the range of 100-200nm). In order to clarify the origin of increasing non-local spin signals at low temperature, the effective spin polarization of $Co_2Fe(Ga_{0.5}Ge_{0.5})$ and the spin diffusion length of Cu for the current LSVs are deduced based on the one-dimensional spin diffusion model [93] for transparent contact, given as

$$\Delta R_{\mathrm{S}} = 4R_{\mathrm{S}}\frac{\left(\frac{P_{\mathrm{FM}}}{1-P_{\mathrm{FM}}^2}\frac{R_{\mathrm{FM}}}{R_{\mathrm{NM}}}\right)^2 e^{\frac{-d}{\lambda_{\mathrm{NM}}}}}{\left(1+\frac{2}{1-P_{\mathrm{FM}}^2}\frac{R_{\mathrm{FM}}}{R_{\mathrm{NM}}}\right)^2 - e^{\frac{-2d}{\lambda_{\mathrm{NM}}}}} \tag{5.1}$$

where $R_{\mathrm{FM}} = \rho_{\mathrm{FM}}\lambda_{\mathrm{FM}}/\mathrm{A_J}$ and $R_{\mathrm{NM}} = \rho_{\mathrm{NM}}\lambda_{\mathrm{NM}}/\mathrm{A_{NM}}$ are the spin resistance of FM and NM, respectively, ρ, λ, $\mathrm{A_J}$ and $\mathrm{A_{NM}}$ correspond to resistivity, spin diffusion length, area of FM/NM interfaces ($w_{\mathrm{FM}}w_{\mathrm{NM}}$), and area of NM wires ($t_{\mathrm{NM}}w_{NM}$), respectively. The P_{FM} is the effective bulk spin polarizations of FM wires. For fitting the data, it is assumed that λ_{FM} is 2.1 nm and ρ_{FM} is 65 $\mu\Omega$cm at 290 K, having the same values as those of $Co_2Fe(Ga_{0.5}Ge_{0.5})$ prepared with the same composition and annealing temperature in current perpendicular to plane giant magnetoresistive (CPP-GMR) devices as reported by Goripati *et al.* [107]. The product of λ_{FM} and ρ_{FM} is assumed to be constant for all range of measurement temperature as a consequence of the inversely-proportional relationship between these two parameters. ρ_{NM} of Cu wire is experimentally measured to be around 1.61 $\mu\Omega$cm and 3.68 $\mu\Omega$cm at 4 K and 290 K, respectively. The moderately higher ρ_{NM} compared with previously reported data [22,102,103,109] can be attributed to the rough edge of Cu wires as a result of Argon-ion milling process to fabricate the wires. The fitting of the data (Fig. 5.2(a)) gives P_{FM} and λ_{FM} of 0.84±0.02 (0.88±0.02) and 259±55 nm (545±157 nm) at 290 K (4 K), respectively. According to the fitting result, the increase in both the effective spin polarization of $Co_2Fe(Ga_{0.5}Ge_{0.5})$ and the spin diffusion

length of Cu contributes to the enhancement of spin signals at low temperature.

As the current work is compared with other reports on Heusler alloys-based LSVs (Table 5.1), the effective spin polarization of $Co_2Fe(Ga_{0.5}Ge_{0.5})$ is found to be significantly higher than that for other Heusler alloys both at room temperature and low temperature. Please note that all data shown in Table 5.1 were deduced within the assumption of transparent FM/NM interfaces. The higher effective spin polarization of B2-ordered $Co_2Fe(Ga_{0.5}Ge_{0.5})$ over that of CoFeAl and Co_2FeSi at low temperature is in agreement with the trend of their spin polarization values as deduced by point contact Andreev reflection (PCAR) for bulk samples [39]. The highly ordered quaternary Heusler alloys were widely demonstrated to exhibit higher spin polarization over that of ternary ones, as a consequence of Fermi-level tuning and increase in the majority electron density of states for the former case [39]. By fitting the magnetoresistive output (ΔRA) as a function of the thickness of FM layers in current-perpendicular-to-plane giant magnetoresistance (CPP-GMR) pseudo spin valves (PSVs), Li *et al.* deduced bulk spin polarization of $Co_2Fe(Ga_{0.5}Ge_{0.5})$ to be 0.93 and 0.83 at 10 K and room temperature [36], respectively. According to this result, the bulk spin polarization of $Co_2Fe(Ga_{0.5}Ge_{0.5})$ reduces at room temperature by about 10%. On the other hand, Sakuraba *et al.* measured the change of the anisotropic magnetoresistance that is claimed to scale with the spin polarization change, and concluded that the bulk spin polarization of $Co_2Fe(Ga_{0.5}Ge_{0.5})$ is hardly degraded at RT [110]. The present result obtained by fitting the d-dependence of spin signals in LSVs support the latter results, i.e., the degradation of the bulk spin polarization of $Co_2Fe(Ga_{0.5}Ge_{0.5})$ at room temperature is relatively small compared to that at low temperature. The considerably high effective spin polarization at room temperature shown in this work emphasizes the promising feature of $Co_2Fe(Ga_{0.5}Ge_{0.5})$ as a spin injector as well as a spin detector for LSVs-based read head applications.

Table 5.1: The effective spin polarization PFM of Heusler alloys in all-metallic LSVs deduced at room temperature (290K) and low temperature (LT)

FM/NM	P_{FM}(290K)	P_{FM}(290K)	References
CoFeAl/Cu	0.55	0.74	S. Oki(77 K) *et al.* [103]
Co_2FeSi/Cu	0.55	0.73 (80 K)	Kimura *et al.* [102]
$Co_2Fe(Ga_{0.5}Ge_{0.5})$/Cu	0.84	0.88 (4 K)	Current work

5.4 Detail temperature dependence of spin dependent transport

Figure 5.3 (a) shows the temperature dependence of non-local spin signals for LSV devices with d=400, 500, and 650 nm, respectively. It can be seen that for all the devices, the non-local spin signals initially increase from 290 K down to 36 K, below which the non-local spin signal exhibit a slight downturn as the temperature further decreases to 4 K. This non-monotonic trend of non-local spin signal at the low temperature range has been widely observed in various combinations of FM and NM materials and is the subject of much debate with regards to its underlying physics. In Figs. 3(b) and 3(c), the temperature dependence of the effective spin polarization of $Co_2Fe(Ga_{0.5}Ge_{0.5})$ and the spin diffusion length of Cu, respectively, are shown. The data are deduced from fitting the spin signals of 3 LSV devices shown in Fig. 5.3(a). Note that the nominal effective spin polarization of $Co_2Fe(Ga_{0.5}Ge_{0.5})$ and spin diffusion length of Cu in Fig. 5.3 (just for 3 devices) at both 290 K and 4 K are slightly

different from those deduced from the data in Fig. 5.2 as a consequence of different number of devices involved in the fit. Nevertheless, the difference in values is still within the uncertainty of fitting result and can be used for analyzing the trend of temperature dependence data. The spin diffusion length of Cu is significantly enhanced with decreasing temperature from 290 K down to 36 K, below which it exhibits a slight downturn. On the other hand, the effective spin polarization of $Co_2Fe(Ga_{0.5}Ge_{0.5})$ also increases with decreasing temperature down to 50 K, below which it saturates. It is accordingly argued that the spin diffusion length of Cu mainly dictates the non-monotonic trend observed in spin signal at the low temperature range.

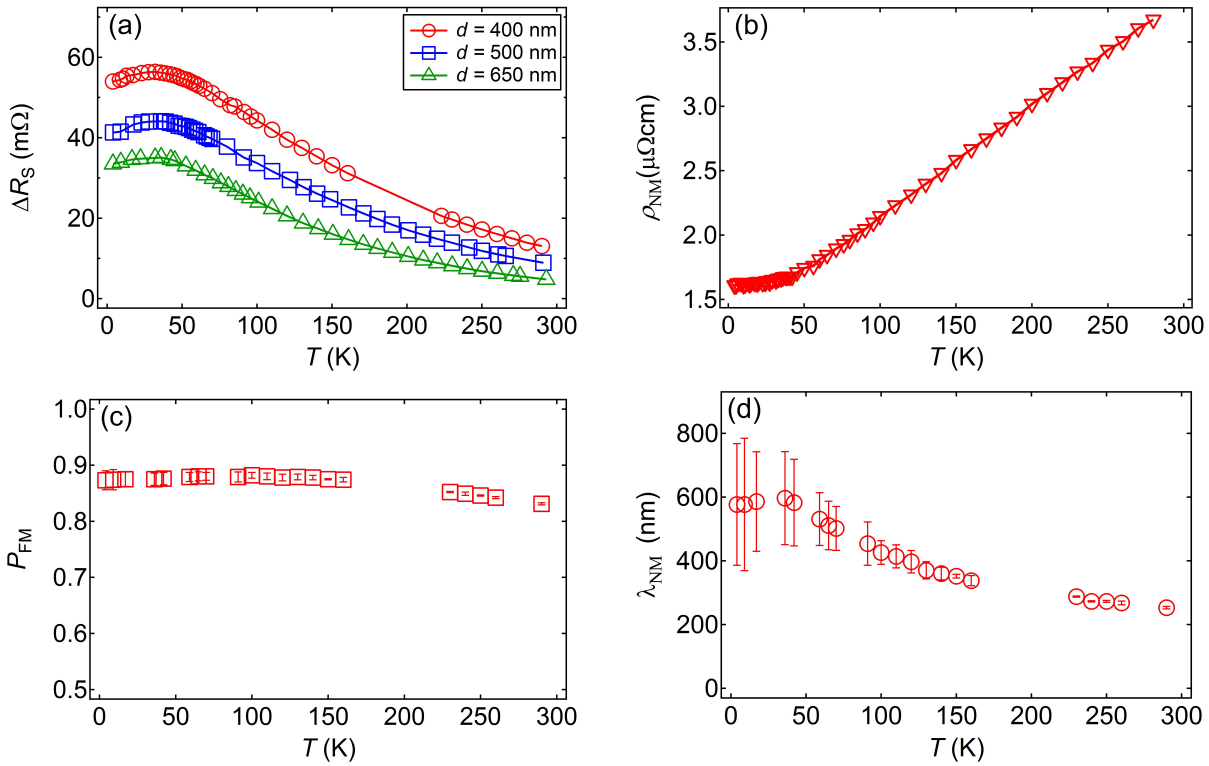

Figure 5.3: (a) The temperature dependence of non-local spin signal for 3 different LSV devices. (b) The effective spin polarization P_{FM} of $Co_2Fe(Ga_{0.5}Ge_{0.5})$ and (b) the spin diffusion length λ_{FM} of Cu which are deduced by fitting the d dependence of spin signals of 3 LSV devices in (a) using the one-dimensional spin diffusion model. The bars in (b) and (c) correspond to the standard error of the fitting.

The spin diffusion length of non-magnetic wires is proportional to the spin relaxation time τ_{sf} following the relation , where D_{NM} corresponds to the diffusion constant. Accordingly, the drop of spin diffusion length at 36 K observed here is a direct consequence of the suppression of τ_{sf} inside the Cu wires. This suppression of τ_{sf} at the low temperature range has been observed in Cu wires and been attributed to the enhanced surface spin flip scattering of oxidized Cu surface [111], the presence of magnetic impurities either at the side surface [112] or in the bulk of Cu wires [113], and Kondo effect in the vicinity of FM/NM interfaces [114]. The presence of randomly distributed magnetic impurities is attributed as the main origin of the suppressed τ_{sf} in Cu wires of the current work. These magnetic impurities might be introduced through sputter target material. This speculation is supported by a recent report from Batley *et al.* [115] who clearly demonstrated that Cu wires made of source material of 99.99% purity exhibit a clear downturn in the spin diffusion length at 30 K, while those of 99.9999%

purity do not. The authors proposed that the presence of magnetic impurities in Cu wires induces Kondo scattering at low temperatures which further suppresses τ_{sf} [115]. Considering that the surface of Cu wires with different purities in Ref. [115] is supposed to be naturally oxidized within the same rate, the enhanced spin flip scattering at the oxidized Cu surface [111] is unlikely to play a dominant role in suppressing τ_{sf} at low temperature. The presence of magnetic impurities at the side surface of Cu wires [112] can also be ruled out in the current LSVs considering that Cu wires were prepared by the top-down process [109]. On the other hand, the Kondo effect in the vicinity of FM/NM interfaces [114] is very unlikely to occur in the current LSVs since the effective spin polarization of $Co_2Fe(Ga_{0.5}Ge_{0.5})$ does not exhibit a downturn at the low temperature range.

5.5 The absence of downturn in CPP-GMR: ballistic vs diffusive transport

Despite the possibility of biased conclusion due to the model of spin-dependent transport and uncertainties in the fitting, the observation of downturn in spin signals of LSVs is convincing. The use of Heusler alloys-based LSVs in this study enables a direct comparison with the temperature dependence of magneto-transport in CPP-GMR devices, considering the similarities of these two systems. In fact the ΔRA of $Co_2Fe(Ga_{0.5}Ge_{0.5})$/Cu-based CPP-GMR monotonically increase with decreasing temperature [49]. The main difference between LSVs and CPP-GMR lies in the spin-dependent transport in Cu wires having different dimensions. If the detrimental Kondo effect (due to magnetic impurities) mainly occurs at the interface as proposed in Ref. [114], CPP-GMR devices would exhibit a similar downturn in spin signals at the low temperature range, which actually is not the case. The quasi-ballistic nature of electron transport inside the Cu spacer of CPP-GMR devices may suppress the interaction of spins with magnetic impurities hence resulting in the monotonic trend of spin signals with decreasing temperature. In LSVs, the transport inside Cu wires is within the diffusive regime and spins more frequently scatter and more frequently interact with any impurities, resulting in the significant downturn in spin signals as observed here.

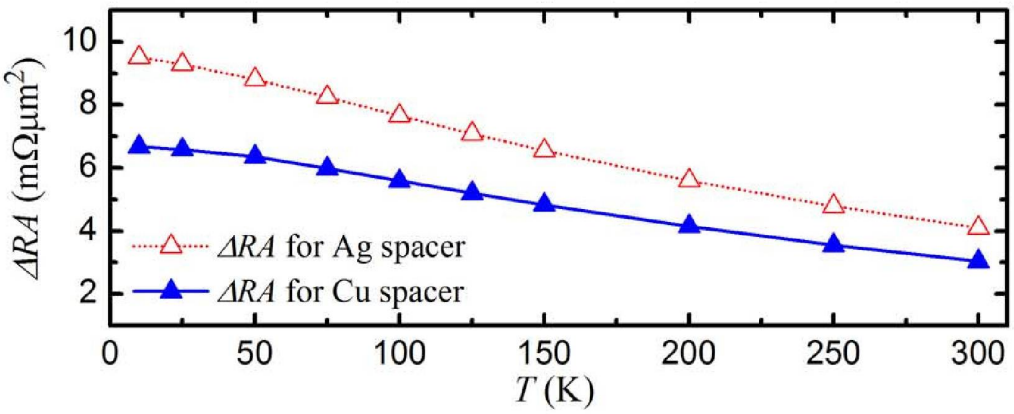

Figure 5.4: The temperature dependence of ΔRA in CPP-GMR devices(After Li *et al*[49])

5.6 Summary

In summary, the observation of large non-local spin signals of 13 mΩ and 54 mΩ measured at 290 K and 4 K, respectively, is reported. It demonstrates the highly efficient spin injection and detection using $Co_2Fe(Ga_{0.5}Ge_{0.5})$ Heusler alloy. The spin polarization of $Co_2Fe(Ga_{0.5}Ge_{0.5})$ was estimated to be 0.88±0.02 at 10 K and 0.84±0.02 at room temperature by fitting to the one dimensional diffusion model, indicating the half-metallic nature of $Co_2Fe(Ga_{0.5}Ge_{0.5})$ even at room temperature. The LSVs shows a non-monotonic trend of non-local spin signal at the low temperature range with a significant downturn at 36 K. The fit based on the one-dimensional spin diffusion model reveals that the spin diffusion length of Cu exhibits a slight downturn at 36 K, which is attributed to the non-monotonic trend in non-local spin signals at low temperatures. The suppressed spin diffusion length of Cu wires at the low temperature range can be attributed to the presence of magnetic impurities possibly introduced through sputter target material. The diffusive nature of spin-dependent transport in long Cu wires of LSVs makes the detrimental impurities effect becomes more pronounced compared with that in CPP-GMR devices having very thin spacer layer and hence quasi-ballistic nature of transport.

Chapter 6

Summary and future directions

6.1 Summary

The works described in this thesis is intended for the investigation of spin-dependent transport in low RA magnetoresistive devices. As HDD read sensors need to be shrunk down, the RA of corresponding devices also needs to be reduced. The development of barrier materials with narrow band gap was carried out and proposed as an alternative to the widely-used MgO barriers. On the other hand, the so-called lateral spin valve (LSV) structure was demonstrated as a potential alternative to resolve the issue on the physical dimension of generic spin valve structures. The main and important results described in this thesis can be summarized as follows.

1. The spin-dependent tunneling and microstructure of CoFeB/$Mg_{1-x}Ti_xO$ MTJs (x = 0.05 and 0.1) were investigated. The high TMR ratio up to 240% and 160% at room temperature were observed for $Mg_{0.95}Ti_{0.05}O$-based and $Mg_{0.9}Ti_{0.1}O$-based MTJs respectively, at the optimum annealing temperature. This observation of high TMR ratio over 100% implies the presence of symmetry filtering effect even in the alloyed-MgO barriers. The $Mg_{1-x}Ti_xO$ barriers were found to have a rock-salt structure and grow with (001) texture on CoFeB electrodes. The similar microstructure evolution to that in CoFeB/MgO was observed in CoFeB/$Mg_{1-x}Ti_xO$ MTJs upon annealing, leading to the grain-to-grain epitaxy with orientation relation of (001)[110]$Mg_{1-x}Ti_xO$ //(001)[100]CoFe. The $Mg_{1-x}Ti_xO$ barriers were clearly confirmed to have lower RA values compared to those of MgO ones for a given thickness. The fit based on Wenzel-Kramer-Brillouin model confirms the decreasing barrier height with increasing Ti concentration in $Mg_{1-x}Ti_xO$ barriers. The $Mg_{1-x}Ti_xO$-based MTJs exhibit higher TMR ratio than that of MgO-based one for RA lower than 5 $\Omega\mu m^2$ as a consequence of thicker barriers and better wettability. The potential of $Mg_{1-x}Ti_xO$ barriers for MTJs with low RA was demonstrated.

2. The alternative route for the realization of $Co_2Fe(Ga_{0.5}Ge_{0.5})$/Cu LSVs by the top-down microfabrication process was demonstrated. The dependence of the microfabrication reliability on the choice of cap layer materials was systematically investigated, underlining a challenge in realizing clean FM/NM interfaces in a LSV by the top-down process. The use of cap layer materials with significant spin orbit interaction should be avoided in order to anticipate the implanted atoms of cap layer during microfabrication process. As a result of the proper choice of cap layer materials, a very large ΔR_S of 17.3 mΩ could be obtained at room temperature suggesting the importance of clean FM/NM interfaces to achieve efficient spin injection into a NM channel.

3. The large non-local spin signals of 13 mΩ and 54 mΩ were observed at 290 K and 4 K, respectively, demonstrating the highly efficient spin injection and detection using $Co_2Fe(Ga_{0.5}Ge_{0.5})$ Heusler alloy. The spin polarization of $Co_2Fe(Ga_{0.5}Ge_{0.5})$ was estimated to be 0.88±0.02 at 10 K and 0.84±0.02 at room temperature, indicating the half-metallic nature of $Co_2Fe(Ga_{0.5}Ge_{0.5})$ even at room temperature. The LSVs shows a non-monotonic trend of non-local spin signal at the low temperature range with a significant downturn at 36 K. The fit based on the one-dimensional spin diffusion model reveals that the spin diffusion length of Cu exhibits a slight downturn at 36 K, which is attributed to the non-monotonic trend in non-local spin signals at low temperatures. The suppressed spin diffusion length of Cu wires at the low temperature range can be attributed to the presence of magnetic impurities possibly introduced through sputter target material. The diffusive nature of spin-dependent transport in long Cu wires of LSVs makes the detrimental impurities effect becomes more pronounced compared with that in CPP-GMR devices having very thin spacer layer and hence quasi-ballistic nature of transport.

6.2 Future directions

The use of metallic elements as dopants/constituents can be considered as one of potential directions to obtain low-*RA* MTJs. Despite the good TMR properties (high TMR ratio) of $Mg_{1-x}Ti_xO$-based MTJs, there is still plenty of rooms for the improvements. Considering the typical valence electrons of Ti around 4, while it is 2 for Mg, the $Mg_{1-x}Ti_xO$ barriers prepared for this thesis might be non-stoichiometric or contains a lot of oxygen vacancies. The post-oxidation treatment on $Mg_{1-x}Ti_xO$ barriers can give a good extention of this study regardless of the possible TMR ratio that might be obtained. On the other hand, further increasing the concentration of Ti is likely to result in more narrow band gap, that may reveal the lowest possible *RA* we can obtain with $Mg_{1-x}Ti_xO$ barriers while keeping sufficiently high TMR ratio. The investigation on other dopant elements can be easily chosen as an extension of the $Mg_{1-x}Ti_xO$ work. In fact, Mn and Fe dopants/substituents were already demonstrated to keep the high TMR ratio of alloyed-MgO MTJs [78], though the detail mechanism is still unclear. While the $Mg_{1-x}Ti_xO$ barrier investigated in this thesis was prepared with in-plane CoFeB electrodes, it is of practical importance to extend the use of the narrow band materials for perpendicular MTJs that can benefit, in particular, the development of MRAM. The interfacial perpendicular magnetic anistropy of thin CoFeB adjacent to oxide barriers is likely to be observed with the use of $Mg_{1-x}Ti_xO$ barrier.

LSV devices described in this thesis were prepared from epitaxial films. Nevertheless, it is of practical importance to use polycrystalline films that are more preferred in industry due to the lower preparation cost. Some Heusler alloys, in fact, were already reported to show high atomic order at lower annealing temperature in the form of polycrystalline films [108, 116]. Since the spin signal in LSV is roughly proportional to the spin diffusion length of NM channels, the use of NM materials that have longer spin diffusion length compared with that of Cu should be investigated. Unfortunately, the choice is very limited since in fact Cu itself is considered as one of the most conductive metals. This situation just leaves Ag, the most conductive metal, as the only remaining option. Fortunately, some variants of Ag alloys exist such as AgZn [117], AgMg [118], and AgSn [119]. By adjusting the concentration of substituting element, we might be able to find the trade-off composition for which the spin diffusion length of Ag alloys is longer or comparable to that of Cu, while having the advantage of smaller lattice

mismatch with Heusler alloys electrodes. The interfacial engineering by which a very thin material is inserted in between FM and NM layers can be considered as a potential strategy to improve the spin signal of LSVs. For instance, a very thin NiAl was recently reported to improve the band matching between FM and NM layers, leading to the high MR ratio in CPP-GMR devices [120]. The same approach can be anticipated to work as well in LSVs. The different procedure of microfabrication process, of course, can still be explored. The so-called etch-back process [121], in which the NM layer is deposited below the FM layer, is a good alternative for preparing LSV devices without doing the *in situ* milling process. Nevertheless, detail crystal growth optimization is necessary if the Heusler alloys to be used as FM layers. The NM layer grown above the insulating oxide underlayer should provide a flat and a good template (orientation matching) for the Heusler alloy layer. In fact, it is widely known that highly conductive NM layers are difficult to grow with the good flatness on oxide underlayers, hence hindering the high quality growth of the Heusler alloy layers and presenting a big challenge for the etch-back process.

Appendix A

The fitting procedure

The fitting of ΔR_S vs d based on the one-dimensional spin diffusion model can be performed using data analysis software such as Igor Pro, Origin, Mathlab, and so on. In order to have a a good fitting result, several physical parameters needs be known or assumed while the ones that need to deduced from the fitting can be set as free fitting parameter. The P_{FM}, P_J, and λ_{NM} are the parameters that are usually deduced in the fitting while other parameters are known from a direct measurement or literature. The general expression of the one-dimensional spin diffusion model basically allows us to deduced these three parameters at the same time supposed that the FM/NM interface resistance is non-negligible. However, due the dependencies between bulk FM and interfacial FM/NM contributions in the equation, the fitting would result in deduced parameters having large standard deviation which can be seen in Fig A.1. In addition, the deduced values are strongly dependent on the initial value, though the fitting (line) quality would be the same. Therefore, it indicates that we need to avoid deducing P_{FM} and P_J, simultaneously, in order to get a reliable value. It is noted that the deduced λ_{NM} is almost the same regardless of P_{FM} and P_J values, indicating the former is a reliable value and mainly dependent on the decay rate of ΔR_S with d.

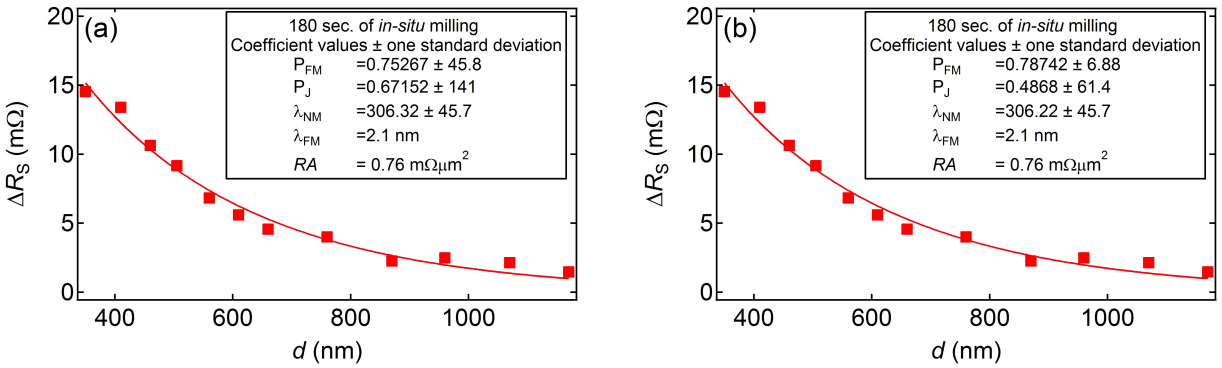

Figure A.1: The fitting to ΔR_S vs d for different initial values of P_{FM} and P_J. The P_{FM}, P_J, and λ_{NM} are set as free parameters to be deduced.

For the treatment of data in chapter 3, it is reasonable if we then assume the value of P_{FM} according to report of Goripati *et al.* [107], while set P_J as a free parameters to be deduced, since the change in ΔR_S with in-situ milling time for Ru-capped LSVs can be anticipated to originate from the FM/NM interfaces. In addition, the λ_{NM} can also be deduced simultaneously. Since the RA of FM/NM interfaces cannot be measured accurately in the current LSVs, a range of 0.05-1.5 m$\Omega\mu$m^2 is assumed.

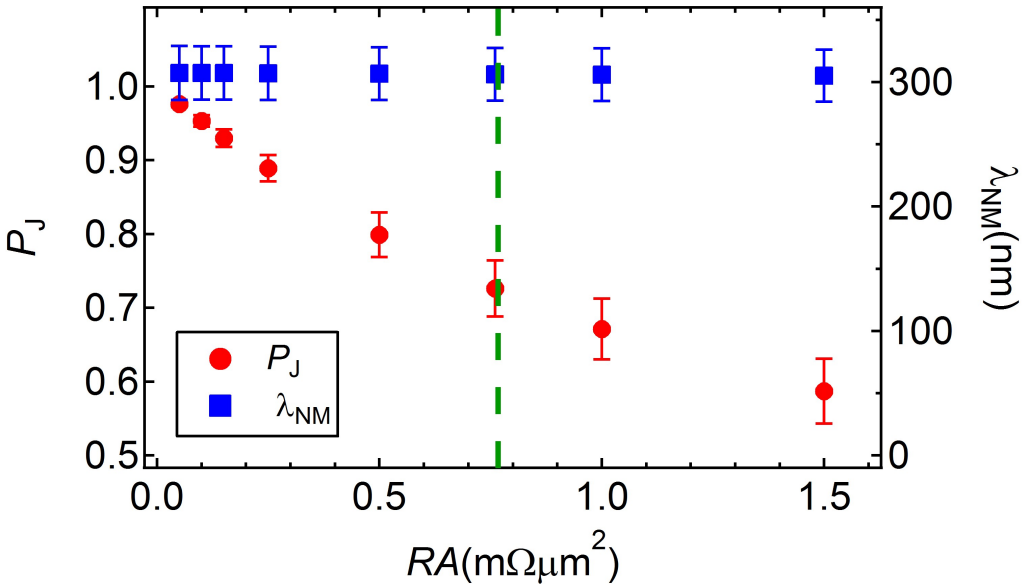

Figure A.2: The deduced P_J and λ_{NM} for a range of assumed RA of $Co_2Fe(Ga_{0.5}Ge_{0.5})$/Cu interfaces. The green dashed line corresponds to RA of $Co_2Fe(Ga_{0.5}Ge_{0.5})$/Ag interfaces, $0.76\pm0.25 m\Omega\mu m^2$ measured by Goripati *et al*[107].

It can be seen in Fig. A.2 that deduced values of λ_{NM} are consistent and in agreement with those in A.1. On the other hand, deduced values of P_J are strongly dependent on the RA of FM/NM interfaces, indicating a great care needs to be taken in deducing P_J.

Table A.1: The RA of Heusler alloy/NM interfaces

FM/NM	RA $m\Omega\mu m^2$	References
$Co_2Fe(Al_{0.5}Si_{0.5})$/Ag	$0.25^{+0.30}_{-0.25}$	Nakatani *et al.* [122]
$Co_2Fe(Ga_{0.5}Ge_{0.5})$/Ag	$0.76^{+0.25}_{-0.25}$	Goripati *et al.* [107]

In order to avoid this uncertainty that might lead to the unreliable P_J, it is quite plausible to assume a transparent interface, $RA \approx 0$, considering the relatively low RA of Heusler-alloy/NM (NM = Ag or Cu) in the literature (see Table A.1). The transparent interface would accordingly ignore the contribution of P_J. In Fig. A.3 the deduced values of P_{FM} for two different P_J assumptions are shown. The P_J are chosen to be 0.3 and 0.61. The P_J of 0.61 is adapted from the report of Li *et al* on $Co_2Fe(Ga_{0.5}Ge_{0.5})$/(Ag or Cu) CPP-GMR devices and set as the top limit. While the P_J of 0.3 is chosen to see how the P_{FM} varies if the P_J reduces by two-fold. In addition, the P_{FM} deduced by the transparent assumption is also shown and indicated by a black dashed line. It can be seen that, the P_{FM} is relatively less sensitive with the change of RA of FM/NM interfaces as well as P_J. In comparison with the transparent assumption value, the deduced P_{FM} just changes within 7% for $RA \leq 1$ $m\Omega\mu m^2$ if P_{FM} is assumed to be 0.61. While it hardly changes for P_{FM} of 0.3. Indeed the deduced λ_{NM} is still consistent for any assumption chosen here. Considering all of these factors, the assumption of transparent interfaces is plausible to use in analyzing the spin-dependent transport of all-metallic LSVs described in this thesis.

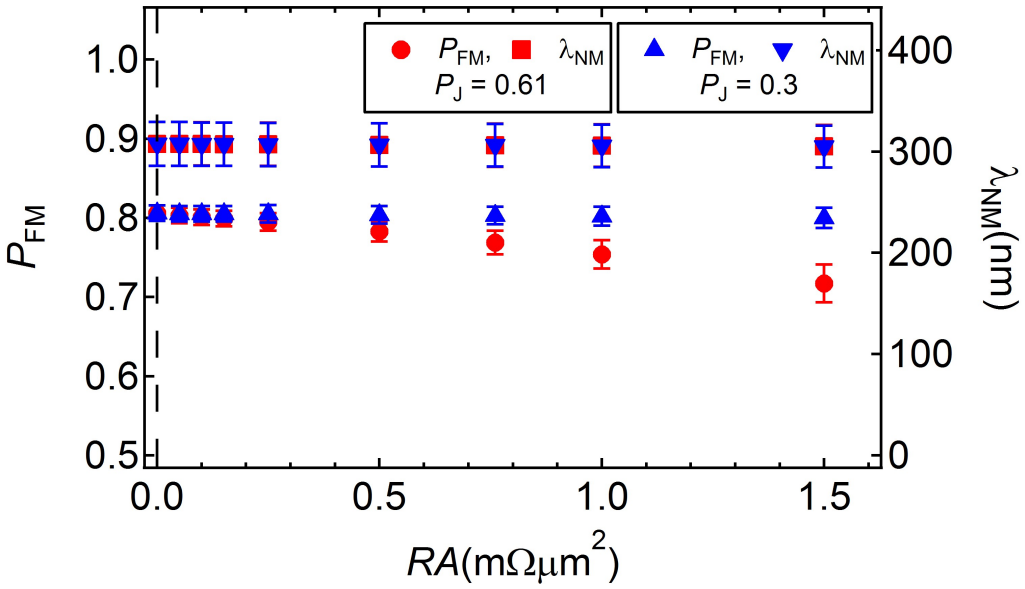

Figure A.3: The deduced P_{FM} and λ_{NM} for a range of assumed RA of $Co_2Fe(Ga_{0.5}Ge_{0.5})$/Cu interfaces. The result for two different P_{J} values are shown. The result for the transparent interface assumption is indicated by the black dashed line.

References

[1] Wolf, S. A. *et al.* Spintronics: A spin-based electronics vision for the future. *Science* **294**, 1488 (2001).

[2] Žutić, I., Fabian, J. & Das Sarma, S. Spintronics: Fundamentals and applications. *Rev. Mod. Phys.* **76**, 323 (2004).

[3] Chappert, C., Fert, A. & Van Dau, F. N. a. The emergence of spin electronics in data storage. *Nat. Mater.* **6**, 813 (2007).

[4] Mott, N. Electrons in transition metals. *Advances in Physics* **13**, 325 (1964).

[5] Fert, A. & Campbell, I. A. Electrical resistivity of ferromagnetic Nickel and Iron based alloys. *Journal of Physics F: Metal Physics* **6**, 849 (1976).

[6] Baibich, M. N. *et al.* Giant magnetoresistance of (001)Fe/(001)Cr magnetic superlattices. *Phys. Rev. Lett.* **61**, 2472 (1988).

[7] Binasch, G., Grünberg, P., Saurenbach, F. & Zinn, W. Enhanced magnetoresistance in layered magnetic structures with antiferromagnetic interlayer exchange. *Phys. Rev. B* **39**, 4828 (1989).

[8] Grunberg, P. Magnetic field sensor with ferromagnetic thin layers having magnetically antiparallel polarized components (1990). US Patent 4,949,039.

[9] Daughton, J. GMR applications. *J. Magn. Magn. Mater.* **192**, 334 (1999).

[10] Moodera, J. S., Kinder, L. R., Wong, T. M. & Meservey, R. Large magnetoresistance at room temperature in ferromagnetic thin film tunnel junctions. *Phys. Rev. Lett.* **74**, 3273–3276 (1995).

[11] Miyazaki, T. & Tezuka, N. Giant magnetic tunneling effect in $Fe/Al_2O_3/Fe$ junction. *J. Magn. Magn. Mater.* **139**, L231 (1995).

[12] Tehrani, S. *et al.* Recent developments in magnetic tunnel junction MRAM. *IEEE Trans. Magn.* **36**, 2752–2757 (2000).

[13] Parkin, S. S. P. *et al.* Giant tunnelling magnetoresistance at room temperature with MgO (100) tunnel barriers. *Nat Mater.* **3**, 862 (2004).

[14] Yuasa, S., Nagahama, T., Fukushima, A., Suzuki, Y. & Ando, K. Giant room-temperature magnetoresistance in single-crystal Fe/MgO/Fe magnetic tunnel junctions. *Nat Mater.* **3**, 868 (2004).

[15] Maehara, H. *et al.* Tunnel magnetoresistance above 170% and resistance-area product of 1 $\Omega(\mu\mathrm{m})^2$ attained by in situ annealing of ultra-thin MgO tunnel barrier. *Appl. Phys. Express* **4**, 033002 (2011).

[16] Fullerton, E. E. & Childress, J. R. Spintronics, magnetoresistive heads, and the emergence of the digital world. *Proceedings of the IEEE* **PP**, 1 (2016).

[17] Nagasaka, K. CPP-GMR technology for magnetic read heads of future high-density recording systems. *J. Magn. Magn. Mat.* **321**, 508 (2009).

[18] Takagishi, M., Yamada, K., Iwasaki, H., Fuke, H. N. & Hashimoto, S. Magnetoresistance ratio and resistance area design of CPP-MR film for 2 Tbit/in^2 read sensors. *IEEE Trans. Magn.* **46**, 2086 (2010).

[19] Yakushiji, K. *et al.* Ultralow-voltage spin-transfer switching in perpendicularly magnetized magnetic tunnel junctions with synthetic antiferromagnetic reference layer. *Appl. Phys. Express* **6**, 113006 (2013).

[20] Childress, J. R. *et al.* All-metal current-perpendicular-to-plane giant magnetoresistance sensors for narrow-track magnetic recording. *IEEE Trans. Magn.* **44**, 90–94 (2008).

[21] Nakatani, T. M. *et al.* Co-based heusler alloys for CPP-GMR spin-valves with large magnetoresistive outputs. *IEEE Trans. Magn.* **48**, 1751 (2012).

[22] Takahashi, Y. K., Kasai, S., Hirayama, S., Mitani, S. & Hono, K. All-metallic lateral spin valves using $Co_2Fe(Ge_{0.5}Ga_{0.5})$ Heusler alloy with a large spin signal. *Appl. Phys. Lett.* **100**, 052405 (2012).

[23] Yamada, M. *et al.* Scalability of spin accumulation sensor. *IEEE Trans. Magn.* **49**, 713 (2013).

[24] Aronov, A. Spin injection in metals and polarization of nuclei. *JETP Lett.* **24**, 32 (1976).

[25] Johnson, M. & Silsbee, R. H. Interfacial charge-spin soupling: injection and detection of spin magnetization in metals. *Phys. Rev. Lett.* **55**, 1790 (1985).

[26] Jedema, F. J., Filip, A. T. & van Wees, B. J. Electrical spin injection and accumulation at room temperature in an all-metal mesoscopic spin valve. *Nature* **410**, 345 (2001).

[27] Jedema, F. J. *Electrical Spin Injection in Metallic Mesoscopic Spin Valve.* Ph.D. thesis, University of Groningen (2002).

[28] Garzon, S. *Spin Injection and Detection in Copper Spin Valve Structures.* Ph.D. thesis, University of Maryland (2005).

[29] Takahashi, S. & Maekawa, S. Spin current in metals and superconductors. *J. Phys. Soc. Jpn.* **77**, 031009 (2008).

[30] Heusler, F. *Ver Dtsch. Phys. Ges.* **5**, 219 (1903).

[31] de Groot, R. A., Mueller, F. M., Engen, P. G. v. & Buschow, K. H. J. New class of materials: Half-metallic ferromagnets. *Phys. Rev. Lett.* **50**, 2024 (1983).

[32] Graf, T., Felser, C. & Parkin, S. Simple rules for the understanding of Heusler compounds. *Progress in Solid State Chemistry* **39**, 1 (2011).

[33] Picozzi, S., Continenza, A. & Freeman, A. J. Role of structural defects on the half-metallic character of Co_2MnGe and Co_2MnSi Heusler alloys. *Phys. Rev. B* **69**, 094423 (2004).

[34] Miura, Y., Nagao, K. & Shirai, M. Atomic disorder effects on half-metallicity of the full-heusler alloys $Co_2(Cr_{1-x}Fe_x)$al: A first-principles study. *Phys. Rev. B* **69**, 144413 (2004).

[35] Sakuraba, Y. *et al.* Mechanism of large magnetoresistance in Co_2MnSi/Ag/Co_2MnSi devices with current perpendicular to the plane. *Phys. Rev. B* **82**, 094444 (2010).

[36] Li, S., Takahashi, Y. K., Furubayashi, T. & Hono, K. Enhancement of giant magnetoresistance by $L2_1$ ordering in $Co_2Fe(Ge_{0.5}Ga_{0.5})$ Heusler alloy current-perpendicular-to-plane pseudo spin valves. *Appl. Phys. Lett.* **103**, 042405 (2013).

[37] Diao, Z. *et al.* Half-metal CPP GMR sensor for magnetic recording. *J. Magn. Magn. Mat.* **356**, 73 (2014).

[38] Balke, B. *et al.* Properties of the quaternary half-metal-type heusler alloy $Co_2Mn_{1-x}Fe_xSi$. *Phys. Rev. B* **74**, 104405 (2006).

[39] Varaprasad, B. *et al.* Spin polarization and Gilbert damping of $Co_2Fe(Ga_{0.5}Ge_{0.5})$ Heusler alloys. *Acta Materialia* **60**, 6257 (2012).

[40] Sato, J., Oogane, M., Naganuma, H. & Ando, Y. Large magnetoresistance effect in epitaxial $Co_2Fe_{0.4}Mn_{0.6}Si$/Ag/$Co_2Fe_{0.4}Mn_{0.6}Si$ devices. *Appl. Phys. Express* **4**, 113005 (2011).

[41] Soulen, R. J. *et al.* Measuring the spin polarization of a metal with a superconducting point contact. *Science* **282**, 85 (1998).

[42] Li, S. *et al.* Large enhancement of bulk spin polarization by suppressing CoMn anti-sites in $Co_2Mn(Ge_{0.75}Ga_{0.25})$ Heusler alloy thin film. *Appl. Phys. Lett.* **108**, 122404 (2016).

[43] Moges, K. *et al.* Enhanced half-metallicity of off-stoichiometric quaternary Heusler alloy $Co_2(Mn, Fe)Si$ investigated through saturation magnetization and tunneling magnetoresistance. *Phys. Rev. B* **93**, 134403 (2016).

[44] Furubayashi, T. *et al.* Structure and transport properties of current-perpendicular-to-plane spin valves using $Co_2FeAl_{0.5}Si_{0.5}$ and Co_2MnSi Heusler alloy electrodes. *J. Appl. Phys.* **107**, 113917 (2010).

[45] Lari, L. *et al.* Correlations between atomic structure and giant magnetoresistance ratio in Co_2(Fe,Mn)Si spin valves. *J. Phys. D: Appl. Phys.* **47**, 322003 (2014).

[46] Chen, J., Li, S., Furubayashi, T., Takahashi, Y. K. & Hono, K. Crystal orientation dependence of current-perpendicular-to-plane giant magnetoresistance of pseudo spin-valves with epitaxial $Co_2FeGe_{0.5}Ga_{0.5}$ Heusler alloy layers. *J. Appl. Phys.* **115**, 233905 (2014).

[47] Chen, J., Furubayashi, T., Takahashi, Y. K., Sasaki, T. T. & Hono, K. Crystal orientation dependence of band matching in all-B2-trilayer current-perpendicular-to-plane giant magnetoresistance pseudo spin-valves using $Co_2FeGe_{0.5}Ga_{0.5}$ Heusler alloy and NiAl spacer. *J. Appl. Phys.* **117**, 17C119 (2015).

[48] Hase, N. *et al.* Current-perpendicular-to-plane spin valves with a $Co_2MnGa_{0.5}Sn_{0.5}$ Heusler alloy. *J. Appl. Phys.* **108**, 093916 (2010).

[49] Li, S., Goripati, H., Takahashi, Y., Furubayashi, T. & Hono, K. Current-perpendicular-to-plane giant magnetoresistance in pseudo spin valves with $Co_2Fe(Ga_{0.5}Ge_{0.5})$ Heusler alloy ferromagnetic layers and Cu/Ag spacer. *IEEE Trans. Magn.* **49**, 4413–4416 (2013).

[50] Miura, Y., Futatsukawa, K., Nakajima, S., Abe, K. & Shirai, M. First-principles study of ballistic transport properties in Co_2MnSi/X/Co_2MnSi(001) (X= Ag, Au, Al, V, Cr) trilayers. *Phys. Rev. B* **84**, 134432 (2011).

[51] Miura, Y., Abe, K. & Shirai, M. Effects of interfacial noncollinear magnetic structures on spin-dependent conductance in Co_2MnSi/MgO/Co_2MnSi magnetic tunnel junctions: A first-principles study. *Phys. Rev. B* **83**, 214411 (2011).

[52] Tsunegi, S. *et al.* Observation of magnetic moments at the interface region in magnetic tunnel junctions using depth-resolved x-ray magnetic circular dichroism. *Phys. Rev. B* **85**, 180408 (2012).

[53] Sakuraba, Y. *et al.* Extensive study of giant magnetoresistance properties in half-metallic Co_2(Fe,Mn)Si-based devices. *Appl. Phys. Lett.* **101**, 252408 (2012).

[54] Nedelkoski, Z. *et al.* The effect of atomic structure on interface spin-polarization of half-metallic spin valves: Co_2(Mn)Si/Ag epitaxial interfaces. *Appl. Phys. Lett.* **107**, 212404 (2015).

[55] Tedrow, P. M. & Meservey, R. Spin-dependent tunneling into ferromagnetic Nickel. *Phys. Rev. Lett.* **26**, 192 (1971).

[56] Julliere, M. Tunneling between ferromagnetic films. *Physics Letters A* **54**, 225 – 226 (1975).

[57] De Teresa, J. M. *et al.* Role of metal-oxide interface in determining the spin polarization of magnetic tunnel junctions. *Science* **286**, 507–509 (1999).

[58] Sakuraba, Y. *et al.* Giant tunneling magnetoresistance in Co_2MnSi/Al-O/Co_2MnSi magnetic tunnel junctions. *App. Phys. Lett.* **88**, 192508 (2006).

[59] Swagten, H. J. M. Chapter one spin-dependent tunneling in magnetic junctions. *Handbook of Magnetic Materials* **17**, 1 (2007).

[60] Yuasa, S. & Djayaprawira, D. D. Giant tunnel magnetoresistance in magnetic tunnel junctions with a crystalline MgO(001) barrier. *J. Phys. D: Appl. Phys.* **40**, R337 (2007).

[61] Sining, M. *et al.* Commercial TMR heads for hard disk drives: characterization and extendibility at 300 Gbit/in^2. *IEEE Trans. Magn.* **42**, 97–102 (2006).

[62] Engel, B. N. *et al.* A 4-mb toggle MRAM based on a novel bit and switching method. *IEEE Trans. Magn.* **41**, 132–136 (2005).

[63] Tezuka, N. *et al.* Tunnel magnetoresistance for junctions with epitaxial full-Heusler $Co_2FeAl_{0.5}Si_{0.5}$ electrodes with B2 and $L2_1$ structures. *Appl. Phys. Lett.* **89**, 112514 (2006).

[64] Butler, W. H., Zhang, X.-G., Schulthess, T. C. & MacLaren, J. M. Spin-dependent tunneling conductance of Fe|MgO|Fe sandwiches. *Phys. Rev. B* **63**, 054416 (2001).

[65] Mathon, J. & Umerski, A. Theory of tunneling magnetoresistance of an epitaxial Fe/MgO/Fe(001) junction. *Phys. Rev. B* **63**, 220403 (2001).

[66] Djayaprawira, D. D. *et al.* 230% room-temperature magnetoresistance in CoFeB/MgO/CoFeB magnetic tunnel junctions. *Appl. Phys. Lett.* **86**, 092502 (2005).

[67] Choi, Y. S., Tsunekawa, K., Nagamine, Y. & Djayaprawira, D. Transmission electron microscopy study on the polycrystalline CoFeBMgOCoFeB based magnetic tunnel junction showing a high tunneling magnetoresistance, predicted in single crystal magnetic tunnel junction. *J. Appl. Phys.* **101**, 013907 (2007).

[68] Miyajima, T. *et al.* Transmission electron microscopy study on the crystallization and boron distribution of CoFeB/MgO/CoFeB magnetic tunnel junctions with various capping layers. *Appl. Phys. Lett.* **94**, 122501 (2009).

[69] Karthik, S. V. *et al.* Transmission electron microscopy investigation of CoFeB/MgO/CoFeB pseudospin valves annealed at different temperatures. *J. Appl. Phys.* **106**, 023920 (2009).

[70] Ikeda, S. *et al.* Tunnel magnetoresistance of 604% at 300K by suppression of Ta diffusion in CoFeB/MgO/CoFeB pseudo-spin-valves annealed at high temperature. *Appl. Phys. Lett.* **93**, 082508 (2008).

[71] Khvalkovskiy, A. V. *et al.* Basic principles of STT-MRAM cell operation in memory arrays. *J. Phys. D: Appl. Phys.* **46**, 074001 (2013).

[72] Tsunekawa, K. Progress in deposition technology of magnetic tunnel junctions. *J. of the Vac. Soc. of Japan* **57**, 91 (2014).

[73] Yuasa, S. *et al.* Future prospects of MRAM technologies 311 (2013).

[74] Yuasa, S., Suzuki, Y., Katayama, T. & Ando, K. Characterization of growth and crystallization processes in CoFeB/MgO/CoFeB magnetic tunnel junction structure by reflective high-energy electron diffraction. *Appl. Phys. Lett.* **87**, 242503 (2005).

[75] Schfers, M. *et al.* Electric breakdown in ultrathin MgO tunnel barrier junctions for spin-transfer torque switching. *Appl. Phys. Lett.* **95**, 232119 (2009).

[76] Liu, D., Han, X. F. & Guo, H. Junction resistance, tunnel magnetoresistance ratio, and spin-transfer torque in Zn-doped magnetic tunnel junctions. *Phys. Rev. B* **85**, 245436 (2012).

[77] Li, D. L. *et al.* Controlling spin-dependent tunneling by bandgap tuning in epitaxial rocksalt MgZnO films. *Scientific Reports* **4**, 7277 (2014).

[78] E. Kitagawa, E. *et al.* Controlling spin-dependent tunneling by bandgap tuning in epitaxial rocksalt MgZnO films. *U.S. Patent* **US 2014/0264673 A1** (Sep. 18, 2014).

[79] Varaprasad, B. S. D. C. S., Takahashi, Y. K., Ajan, A. & Hono, K. Electrically conductive $(Mg_{0.2}Ti_{0.8})O$ underlayer to grow FePt-based perpendicular recording media on glass substrates. *J. Appl. Phys.* **113**, 203907 (2013).

[80] Du, Y., Furubayashi, T., Takahashi, Y., Sakuraba, Y. & Hono, K. Polycrystalline CPP-GMR pseudo spin-valves using (001) textured $Co_2Fe(Ga_{0.5}Ge_{0.5})$ layer grown on conductive $Mg_{0.5}Ti_{0.5}O$ buffer layer. *IEEE Trans. Magn.* **PP**, 1–1 (2015).

[81] Ikeda, S. *et al.* A perpendicular-anisotropy CoFeB/MgO magnetic tunnel junction. *Nat. Mater.* **9**, 721 (2010).

[82] Wang, W. H. *et al.* Growth of atomically smooth MgO films on graphene by molecular beam epitaxy. *Appl. Phys. Lett.* **93**, 183107 (2008).

[83] Sukegawa, H. *et al.* Tunnel magnetoresistance with improved bias voltage dependence in lattice-matched Fe/spinel-$MgAl_2O_4$/Fe(001) junctions. *Appl. Phys. Lett.* **96**, 212505 (2010).

[84] Ikeda, S. *et al.* Tunnel magnetoresistance in MgO-barrier magnetic tunnel junctions with bcc-CoFe(B) and fcc-CoFe free layers. *J. Appl. Phys.* **99**, 08A907 (2006).

[85] Matsumoto, R. *et al.* Dependence on annealing temperatures of tunneling spectra in high-resistance CoFeB/MgO/CoFeB magnetic tunnel junctions. *Solid State Communications* **143**, 574 (2007).

[86] Teixeira, J. M. *et al.* Electrode band structure effects in thin MgO magnetic tunnel junctions. *Appl. Phys. Lett.* **100**, 072406 (2012).

[87] Ringer, S., Vieth, M., Bär, L., Rührig, M. & Bayreuther, G. Conductance anomalies of CoFeB/MgO/CoFeB magnetic tunnel junctions. *Phys. Rev. B* **90**, 174401 (2014).

[88] Maat, S. & Marley, A. C. *Physics and Design of Hard Disk Drive Magnetic Recording Read Heads*, 1 (Springer Netherlands, 2013).

[89] Choi, Y. S. *et al.* Effect of Ta getter on the quality of MgO tunnel barrier in the polycrystalline CoFeB/MgO/CoFeB magnetic tunnel junction. *Appl. Phys. Lett.* **90**, 012505 (2007).

[90] Tsunekawa, K. *et al.* Giant tunneling magnetoresistance effect in low-resistance CoFeB/MgO(001)/CoFeB magnetic tunnel junctions for read-head applications. *Appl. Phys. Lett.* **87**, 072503 (2005).

[91] Hosoya, H., Nagamine, Y., Tsunekawa, K., Zayets, V. & Yuasa, S. Characterization of ultra-thin Fe-Co layer grown on amorphous Co-Fe-B by in situ reflective high-energy eleada pctron diffraction. *Appl. Phys. Express* **6**, 063003 (2013).

[92] Jedema, F. J., Heersche, H. B., Filip, A. T., Baselmans, J. J. A. & van Wees, B. J. Electrical detection of spin precession in a metallic mesoscopic spin valve. *Nature* **416**, 713 (2002).

[93] Takahashi, S. & Maekawa, S. Spin injection and detection in magnetic nanostructures. *Phys. Rev. B* **67**, 052409 (2003).

[94] Johnson, M. Optimized device characteristics of lateral spin valves. *IEEE Trans. Elec. Dev.* **54**, 1024 (2007).

[95] Kimura, T. & Otani, Y. Large spin accumulation in a Permalloy-Silver lateral spin valve. *Phys. Rev. Lett.* **99**, 196604 (2007).

[96] Schmidt, G., Ferrand, D., Molenkamp, L. W., Filip, A. T. & van Wees, B. J. Fundamental obstacle for electrical spin injection from a ferromagnetic metal into a diffusive semiconductor. *Phys. Rev. B* **62**, R4790 (2000).

[97] Valenzuela, S. O. & Tinkham, M. Spin-polarized tunneling in room-temperature mesoscopic spin valves. *Appl. Phys. Lett.* **85**, 5914 (2004).

[98] Ji, Y., Hoffmann, A., Pearson, J. E. & Bader, S. D. Enhanced spin injection polarization in Co/Cu/Co nonlocal lateral spin valves. *Appl. Phys. Lett.* **88**, 052509 (2006).

[99] Yang, T., Kimura, T. & Otani, Y. Giant spin-accumulation signal and pure spin-current-induced reversible magnetization switching. *Nat. Phys.* **4**, 851 (2008).

[100] Casanova, F., Sharoni, A., Erekhinsky, M. & Schuller, I. K. Control of spin injection by direct current in lateral spin valves. *Phys. Rev. B* **79**, 184415 (2009).

[101] Bridoux, G., Costache, M. V., Van de Vondel, J., Neumann, I. & Valenzuela, S. O. Enhanced spin signal in nonlocal devices based on a ferromagnetic CoFeAl alloy. *Appl. Phys. Lett.* **99**, 102107 (2011).

[102] Kimura, T., Hashimoto, N., Yamada, S., Miyao, M. & Hamaya, K. Room-temperature generation of giant pure spin currents using epitaxial Co_2FeSi spin injectors. *NPG Asia Mater* **4** (2012).

[103] Oki, S. *et al.* Effect of addition of Al to single-crystalline CoFe electrodes on nonlocal spin signals in lateral spin-valve devices. *Appl. Phys. Express* **5**, 063004 (2012).

[104] Eid, K., Fonck, R., Darwish, M. A., Pratt, W. P. & Bass, J. Current-perpendicular-to-plane-magnetoresistance properties of Ru and Co/Ru interfaces. *J. Appl. Phys.* **91**, 8102 (2002).

[105] Khasawneh, M. A., Klose, C., Pratt, W. P. & Birge, N. O. Spin-memory loss at Co/Ru interfaces. *Phys. Rev. B* **84**, 014425 (2011).

[106] Morota, M. *et al.* Indication of intrinsic spin hall effect in 4d and 5d transition metals. *Phys. Rev. B* **83**, 174405 (2011).

[107] Goripati, H. S., Furubayashi, T., Takahashi, Y. K. & Hono, K. Current-perpendicular-to-plane giant magnetoresistance using $Co_2Fe(Ga_{1-x}Ge_x)$ Heusler alloy. *J. Appl. Phys.* **113**, 043901 (2013).

[108] Shirotori, S., Hashimoto, S., Takagishi, M., Kamiguchi, Y. & Iwasaki, H. All-metallic nonlocal spin valves using polycrystalline $Co_2(FeMn)Si$ Heusler alloy with large output. *Appl. Phys. Lett.* **8**, 023103 (2015).

[109] Ikhtiar *et al.* Magneto-transport and microstructure of $Co_2Fe(Ga_{0.5}Ge_{0.5})$/Cu lateral spin valves prepared by top-down microfabrication process. *J. Appl. Phys.* **115**, 173912 (2014).

[110] Sakuraba, Y. *et al.* Quantitative analysis of anisotropic magnetoresistance in Co_2MnZ and Co_2FeZ epitaxial thin films: A facile way to investigate spin-polarization in half-metallic Heusler compounds. *Appl. Phys. Lett.* **104**, 172407 (2014).

[111] Kimura, T., Sato, T. & Otani, Y. Temperature evolution of spin relaxation in a NiFe/Cu lateral spin valve. *Phys. Rev. Lett.* **100**, 066602 (2008).

[112] Zou, H. & Ji, Y. The origin of high surface spin-flip rate in metallic nonlocal spin valves. *Appl. Phys. Lett.* **101**, 082401 (2012).

[113] Villamor, E., Isasa, M., Hueso, L. E. & Casanova, F. Contribution of defects to the spin relaxation in copper nanowires. *Phys. Rev. B* **87**, 094417 (2013).

[114] O'Brien, L. *et al.* Kondo physics in non-local metallic spin transport devices. *Nat. Commun.* **5**, 1 (2014).

[115] Batley, J. T. *et al.* Spin relaxation through Kondo scattering in Cu/Py lateral spin valves. *Phys. Rev. B* **92**, 220420 (2015).

[116] Iwasaki, H., Hashimoto, S., Takagishi, M., Shirotori, S. & Kasai, S. CPP-GMR using continuous MgAlCu-O spacer with low *RA* and high MR ratio. *13th Joint MMM-Intermag Conference* (2016).

[117] Du, Y. *et al.* Large magnetoresistance in current-perpendicular-to-plane pseudo spin-valves using $Co_2Fe(Ga_{0.5}Ge_{0.5})$ Heusler alloy and AgZn spacer. *Appl. Phys. Lett.* **107**, 112405 (2015).

[118] Narisawa, H., Kubota, T. & Takanashi, K. Current perpendicular to film plane type giant magnetoresistance effect using a Ag-Mg spacer and $Co_2Fe_{0.4}Mn_{0.6}Si$ Heusler alloy electrodes. *Appl. Phys. Express* **8**, 063008 (2015).

[119] Read, J. C. *et al.* Current-perpendicular-to-the-plane giant magnetoresistance in spin-valves with AgSn alloy spacers. *J. Appl. Phys.* **118**, 043907 (2015).

[120] Jung, J. W., Sakuraba, Y., Sasaki, T. T., Miura, Y. & Hono, K. Enhancement of magnetoresistance by inserting thin NiAl layers at the interfaces in $Co_2Fe(Ga_{0.5}Ge_{0.5})$/Ag/$Co_2Fe(Ga_{0.5}Ge_{0.5})$ current-perpendicular-to-plane pseudo spin valves. *Appl. Phys. Lett.* **108**, 102408 (2016).

[121] Smith, A. K., Jamali, M., Stecklein, G., Crowell, P. A. & Wang, J. P. Non-local lateral spin-valve devices fabricated with a versatile top-down fabrication process. *IEEE Magn. Lett.* **7**, 1 (2016).

[122] Nakatani, T. M., Furubayashi, T. & Hono, K. Interfacial resistance and spin-dependent scattering in the current-perpendicular-to-plane giant magnetoresistance using $Co_2Fe(Al_{0.5}Si_{0.5})$ Heusler alloy and Ag. *J. Appl. Phys.* **109**, 07B724 (2011).

Acknowledgement

I would like to express my sincere gratitude to my advisor Prof. Kazuhiro Hono for the opportunity of conducting doctoral research at Magnetic Materials Unit (MMU). I greatly appreciate his supervision and endless challenges in doing cutting-edge research. I am greatly indebted to his suggestions in shaping and improving my writing and presentation skills which are very pivotal for an independent researcher to-be.

My great appreciation also goes to Prof. Seiji Mitani, Prof. Shinji Kuroda, and Prof. Takashi Sekiguchi for serving on the committee of my Ph.D thesis. Thank you for the time the committee spent evaluating my Ph.D thesis and to attend the defense presentation.

I would like to express my sincere gratitude to my main mentors Dr. Shinya Kasai (who also served on the committee) and Dr. Yukiko Takahashi. I really appreciated the complete supports they provided me, from experimental techniques, data analysis, data presentation, paper writing, and research direction. I learned a lot for these three years. The knowledge and skills you taught are of great importance for my future career.

I would like to express my sincere gratitude to Dr. Tadakatsu Ohkubo, Akihide Itoh, and Cheng Po-Han for the collaboration on microstrcuture characterization. This collaboration is very pivotal to enable a comprehensive investigation. I greatly benefited from their important contributions on my work.

I wish to thank (once again) Prof. Seiji Mitani, Dr. Takao Furubayashi, and Dr. Yuya Sakuraba for the collaboration and supervision on experimental techniques.

I acknowledge National Institute for Materials Science for providing the junior researcher assistantship.

I wish to thank Dr. Hiroaki Sukegawa for sharing his know-how and fabrication tools on magnetic tunnel junctions. I wish to thank Thomas Scheike for the latex teaching and discussion on magnetic tunnel junction research. I thank Shigeyuki Hirayama for our collaboration on lateral spin valves works and the maintenance of experimental equipments. I thank Dr. Songtian Li and Dr. Tomoya Nakatani in providing me with his detail fitting work on CPP-GMR devices, opening my view on the challenges of deducing spin polarization parameters. I would like to thank all members of MMU for the friendship and supports.

Finally I would like to thank Dyah-Mikka-Maya, our parents, brothers-sisters, and all best friends for

the endless supports.

Publication

1. Ikhtiar, S. Kasai, A. Itoh, Y. K. Takahashi, T. Ohkubo, S. Mitani, and K. Hono,
"Magneto-transport and microstructure of $Co_2Fe(Ga_{0.5}Ge_{0.5})$/Cu lateral spin valves prepared by top-down microfabrication process",
J. Appl. Phys. **115**, 173912 (2014)
http://dx.doi.org/10.1063/1.4874936

2. Ikhtiar, S. Kasai, Y. K. Takahashi, T. Furubayashi, S. Mitani, and K. Hono,
"Temperature dependence of magneto-transport properties in $Co_2Fe(Ga_{0.5}Ge_{0.5})$/Cu lateral spin valves",
Appl. Phys. Lett. **108**, 062401 (2016)
http://dx.doi.org/10.1063/1.4941549

3. Ikhtiar, S. Kasai, P. -H. Cheng, T. Ohkubo, Y. K. Takahashi, T. Furubayashi, and K. Hono,
"Magnetic tunnel junctions with a rock-salt-type $Mg_{1-x}Ti_xO$ barrier for low area resistance product",
Appl. Phys. Lett. **108**, 173912 (2016)
http://dx.doi.org/10.1063/1.4953783